

BCW Rate + Shape Analysis

Jiajie Ling^a, Xin Qian^b, Wei Wang^{c*}, Chao Zhang^{a*}

^a*Brookhaven National Laboratory*

^b*California Institute of Technology*

^c*College of William and Mary*

Email:

jjling@bnl.gov

xqian@caltech.edu

wswang@wm.edu

chao@bnl.gov

ABSTRACT: In this tech-note, details of the BCW rate & shape oscillation analysis are presented. The detector energy response has been studied using all available ACU and MCS calibration data. Our data based studies show that the non-linearity clearly has two components: one due to the physics processes in the detector medium which include both quenching which can be described by Birks Law and Cherenkov radiation; the other component, unfortunately, is due to the Daya Bay electronics. The BCW non-linearity model is built based on our studies of all the mono-energetic γ lines and validated independently using 3 sets of continuous $\beta + \gamma$ spectra extracted from Daya Bay data sets: ^{12}B , ^{212}Bi and ^{214}Bi spectra. The BCW anti-neutrino candidate selection cuts centered around the DMC cut are described. The efficiencies and uncertainties of the cuts are estimated. The remaining background rates and shapes are discussed. The reactor flux calculation is described and two major fission isotope spectrum calculations, ILL group and Vogel from 1980's and re-evaluations by Huber and Mueller *et al* in 2011, are evaluated and compared. Besides the isotope spectrum uncertainties, reactor uncertainties contributing to flux uncertainties and energy bin correlations are also studied in detail. Due to the numerical challenge of large number of flux uncertainties, we propose a pull-covariance matrix approach to handle reduce the burdgen and the number of nuisance parameters. Our flux correlation studies show energy bin correlations are noticeably different at different sites. Thus, to properly treat the flux energy correlations, we propose a 81×81 covariance matrix to include the correlations between all energy bins of all ADs at different sites. The expected event rate in each energy bin of each AD are calculated using the BCW reactor flux treatment and the detector model centered around the BCW energy non-linearity model. To reduce the burdgen of the minimizer thus increases its stability and reliability, we propose a "smearing matrix" method to speed up the calculation. The details of the fitting models are presented. With the analysis framework we build up, anti-neutrino disappearance is observed at the far detectors. Rate & shape analyses are performed to measure θ_{13} and Δm_{32}^2 (or Δm_{ee}^2)[†] under the oscillation hypotheses and their systematic uncertainty breakdown is estimated. With the P12B data, our results are: $\sin^2 2\theta_{13} = 0.0878 \pm 0.0095$, $\Delta m_{32}^2 = 2.603 \pm 0.219 \times 10^{-3} \text{ eV}^2$. Based on our current understanding of the systematics, we also project future sensitivities to $\sin^2 2\theta_{13}$ and Δm_{ee}^2 of Daya Bay. Our projection shows that the Δm_{ee}^2 sensitivity could be competitive with the currently running beam and atmospheric neutrino oscillation experiments which are measuring the atmospheric mass-squared splitting in μ flavor.

KEYWORDS: reactor anti-neutrino; Daya Bay; θ_{13} ; Δm^2 ; neutrino oscillation; neutrino disappearance; reactor flux; neutrino spectra; covariance matrix; pull method.

*Corresponding Author

[†]Differences between Δm_{32}^2 , Δm_{31}^2 and Δm_{ee}^2 are negligible for the current generation of experiments.

Contents

1. Detector Responses	3
1.1 Energy Resolution	3
1.2 Non-uniformity	3
1.3 Non-linearity	5
1.4 Summary of Data Used in Model Construction	5
1.4.1 Gamma Peaks for Energy Calibration	5
1.4.2 Alpha Energy Points	7
1.4.3 Continuous Spectra	8
1.5 Summary of Birks' Law Based Energy Model	8
1.6 Description of Nominal Model	12
1.6.1 Additional Constrains	12
1.6.2 Nominal Model	12
1.6.3 Validating Energy Model With $\beta + \gamma$ Spectra	23
1.6.4 Validating Energy Model With IBD Spectrum	27
1.7 Summary of Uncertainty Treatment	27
1.7.1 Statistical Uncertainty from Gamma Calibration Points	27
1.7.2 Uncertainties due to k_B and k_C	28
1.7.3 Uncertainties to be used in rate+shape fit	30
1.8 Final Remarks	30
1.8.1 Relative Energy Scale	30
1.8.2 Placed to be improved in the future	31
1.8.3 Summary	31
1.8.4 Data Comparison	31
1.9 Official Energy Model used in the Rate+Shape analysis	32
2. Anti-neutrino Candidates Selection	40
2.1 Run Selection and DAQ Live Time	40
2.2 IBD Candidate Selection and Efficiency of Cuts	40
2.3 Distribution of Anti-neutrino Candidates	41
3. Background Estimation	47
3.1 Accidental Background	47
3.2 ${}^9\text{Li}/{}^8\text{He}$ Background	47
3.3 Fast neutron Background	49
3.4 Correlated ${}^{241}\text{Am}{}^{13}\text{C}$ Background	49
3.5 ${}^{13}\text{C}(\alpha, n){}^{16}\text{O}$ Background	51
3.6 Summary of Background Estimation	51

4. Reactor flux and systematic uncertainties	53
4.1 Reactor antineutrino flux calculation	53
4.1.1 General principle	53
4.1.2 Weekly average thermal power and fission fraction	53
4.2 Reactor flux uncertainties	54
4.2.1 Reactor flux uncertainty sources	54
4.2.2 Uncertainties in fission isotope antineutrino spectra	55
4.2.3 Nuclear reactor related uncertainties	60
4.3 Flux uncertainty treatment: covariance matrix + pull	65
4.3.1 Pull-covariance approach	65
4.3.2 Evaluation of the flux covariance matrix	66
4.3.3 Testing different isotope spectrum calculations	67
4.3.4 Uncertainties and correlations of all 3 sites	68
5. Oscillation Analysis	72
5.1 Rate-only analysis	72
5.2 Rate + Shape analysis	77
5.2.1 Systematic considerations	77
5.2.2 χ^2 construction and event prediction	77
5.2.3 Results	80
6. Summary	82

This note describes the BCW rate+shape analysis of the Daya Bay 6-AD phase data¹. We first describe the most important component of the analysis: detector energy response studies and the establishment of the BCW nonlinearity model. Our IBD event selection is based on the well established BCW decoupled multiplicity cut (DMC). In shape analysis, we face some newly appeared challenges in reactor flux due to the need of treating all spectrum related uncertainties which are not of importance for the rate analysis before. We propose a mixed pull and covariance matrix approach to get the best from both methods. After successfully constructing the AD energy model and treating all systematic uncertainties properly, with the BCW cut selected IBD samples, we construct a general chi-square with clean separation between rate and shape information and present the analysis results and sensitivity projections with future Daya Bay running using the BCW analysis framework. Some details are discussed more in our DocDB entries but we supply sufficient description in this note to give readers a clear big picture.

1. Detector Responses

All detector response results presented in this analysis use the *AdSimple* energy reconstruction algorithm. The details of this algorithm is documented in doc:7334 [1].

1.1 Energy Resolution

Energy resolution is estimated from the width of various energy peaks, as shown in Fig. 1. The best fit functional form of the energy resolution is:

$$\frac{\sigma_E}{E} = 1.16 \sqrt{(1.3\%)^2 + \left(\frac{7.9\%}{\sqrt{E}}\right)^2 + \left(\frac{5.1\%}{E}\right)^2}, \quad (1.1)$$

where E is in the unit of MeV. The terms in the resolution function represent the contribution from spacial/temporal resolution (proportional to E), photon statistics (proportional to \sqrt{E}) and dark noise (constant), respectively. Changing each term by $\pm 30\%$ has negligible effects on the detected IBD prompt spectra, so we fix the resolution function in the later oscillation analysis.

1.2 Non-uniformity

The *AdSimple* reconstruction algorithm has built-in non-uniformity correction to make the energy response more uniform across the detector volume. The position-base correction is extracted from a Monte Carlo template. However, there is still residual non-uniformity, which is then investigated by spallation neutrons. The delayed spectra of spallation neutron is shown in Fig. 5(b). Fig. 2 shows the non-uniformity map (in AD 1) with respect to the AD center. Inside the Gd-LS volume, the peak (~ 8.05 MeV) from neutron capture on Gd are used. Outside of the Gd-LS volume but inside the LS volume, the peak (~ 2.22 MeV) from neutron capture on Hydrogen are used. Inside Gd-LS target volume, the uniformity is better than 0.5%. Outside of the Gd-LS volume, the uniformity is worse. Up to 3% difference can be seen.

The non-uniformity from spallation neutron was cross-checked with the data from *Manual Calibration System* (MCS). A PuC source (combined with ^{60}Co) was deployed to ~ 1700 different

¹Results are based on P12B unblinded data

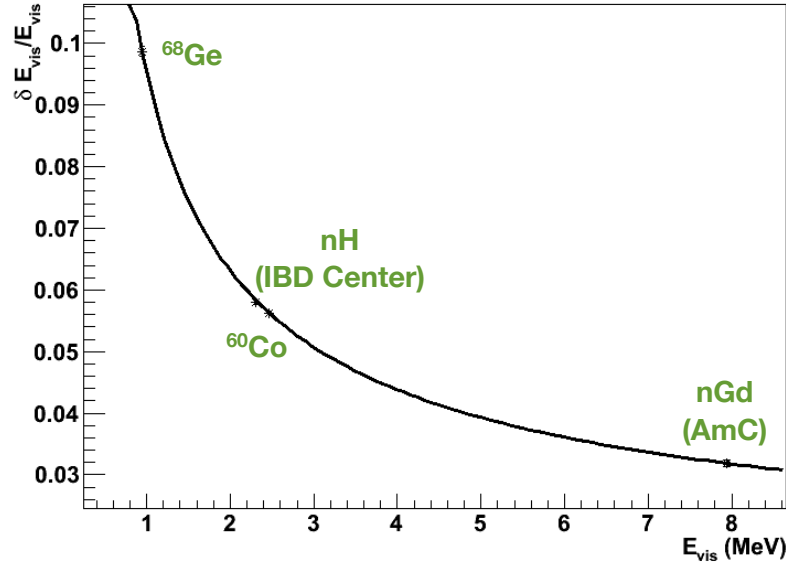


Figure 1. Energy resolution.

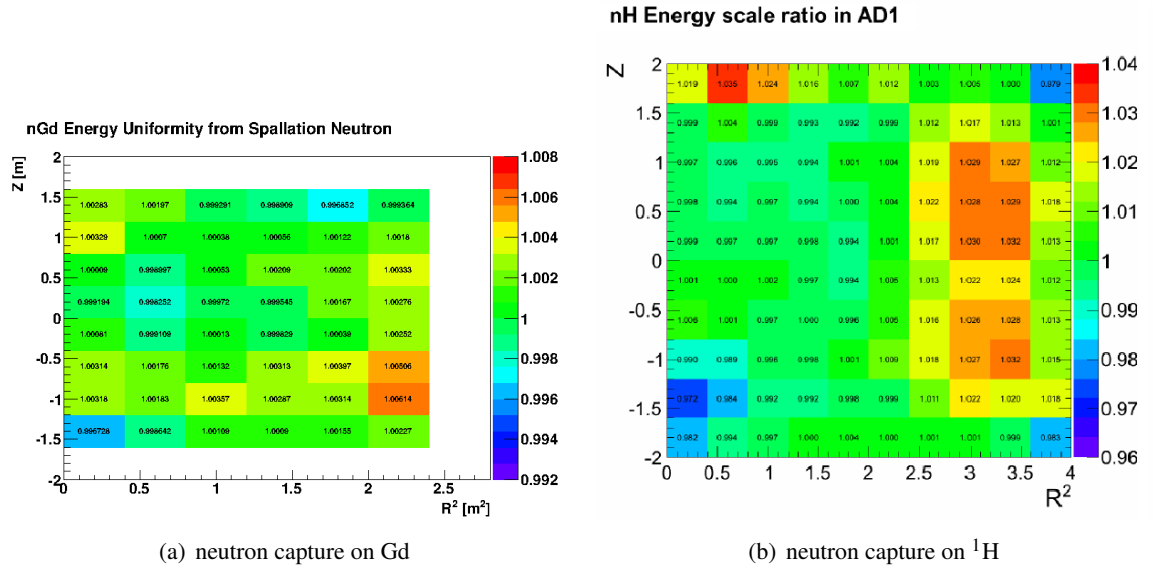


Figure 2. Non-uniformity map (with respect to detector center) from spallation neutrons

locations throughout the detector volume. The neutron capture on Gd peak was selected. The results are shown in Fig. 3. Similar non-uniformity trends are seen from both data sets. Details of the BCW MCS analysis can be found from doc:8574 [2].

For uniformly distributed IBD events, the non-uniformity introduces an overall energy resolution increase of only $\sim 0.7\%$ (part of the first term in the resolution function Eq. 1.1) so is mostly negligible. However this effect must be accounted for when doing energy calibration study, because different calibration peaks selected at different regions of the detector will have a non-negligible

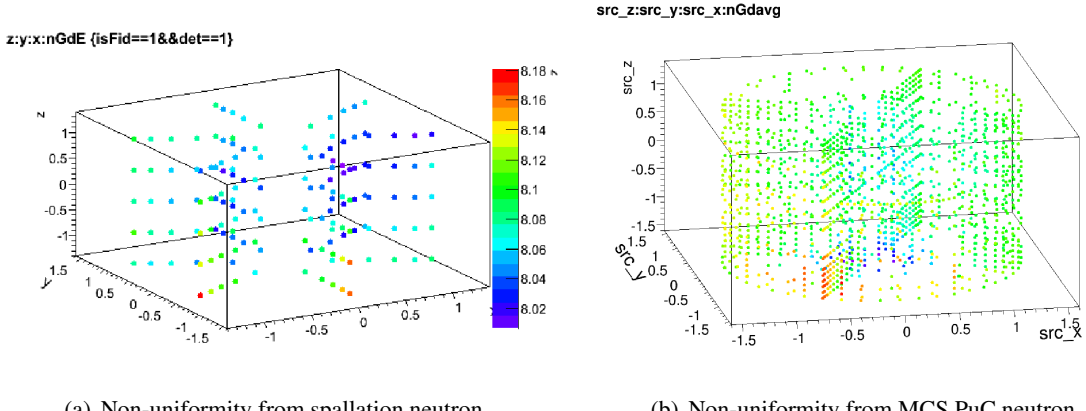


Figure 3. Non-uniformity of the neutron capture on Gd peak from (a) spallation neutron, (b) MCS PuC neutron.

systematic shift in energy.

1.3 Non-linearity

In this section, we review the BCW’s energy model (the BCW model). The overall non-linearity of the BCW model consists two parts: scintillator energy non-linearity and effective electronics non-linearity. The scintillator energy non-linearity is based on Birks’ Law [3]. Additional contributions from Cerenkov light (electron/positron) are included. The parameters (Birks’ constant and percentage Cerenkov contribution at 1 MeV for electron) directly constrained by the Daya Bay data. The electronics non-linearity is an effective non-linearity, which is determined by our gamma calibration data.

The nominal BCW model is checked with the continuous spectra: ^{212}Bi , ^{214}Bi , ^{208}Tl , and ^{12}B . Furthermore, the nominal BCW model is ready to be compared with the measured IBD spectrum. The uncertainty of BCW model is evaluated by varying Birks’ constant and percentage of Cerenkov contribution (at 1 MeV for electron).

The note is organized as the following: Sec. 1.4 summarizes the data used in constructing our model; Sec. 1.5 summarizes the principle of the BCW model; Sec. 1.6 describes the nominal model; Sec. 1.7 and Sec. 1.8 summarizes the uncertainty treatment and the final remarks, respectively.

1.4 Summary of Data Used in Model Construction

1.4.1 Gamma Peaks for Energy Calibration

There are many γ peaks that can be extracted from data for use in energy calibration. They can be sorted into three categories:

- Radioactive sources that are deployed regularly (^{68}Ge , ^{60}Co , ^{241}Am , ^{13}C) or at summer special calibration period (^{137}Cs , ^{54}Mn , ^{40}K , ^{241}Am , 9Be , Pu , ^{13}C .)
- Peaks that can be identified from singles spectra in regular physics runs: The ^{40}K and ^{208}Tl peaks are mostly from the radio-impurity on the PMT glass. The ^{241}Am , ^{13}C source parked

on top of the detector lid produces neutrons which capture on stainless steel and produces a few high energy gamma-rays that are also clear on the singles spectra.

- Peaks that can be identified from correlated spectra in regular physics runs: (spallation or IBD) neutron captures on Gd, neutron captures on H.

When fitting the energy peaks, we adopt the following scheme:

- For calibration sources, center deployments in AD1 are used. If AD1 data are not available, AD2 data are used. The energy difference between AD1 and AD2 are treated as a source of systematic errors.
- To reduce background, a 1 m radius fiducial volume cut is applied for center calibration source. When available, the neighboring physics runs are used for background subtraction.
- Most of the peaks are fitted with a Gaussian signal plus a polynomial or exponential background. For nGd captures the double crystal ball function is used. For ^{60}Co , a Gaussian plus crystal ball function is used. For ^{68}Ge , a double-Gaussian function is used.
- All fitted peak energies are then corrected to full target volume energy (E_{fv}) using the non-uniformity map obtained from spallation neutron capture events (Sec.1.2). For example, the E_{fv}/E_{center} ratio in AD1 is 1.0017. This correction is in particular necessary for external γ 's.
- Peaks from source deployments are preferred over from others (e.g. ^{40}K source are preferred over external ^{40}K .)

The spectra of all γ 's for energy calibration are shown in Fig. 4, 5 and 6, overlaid with the best-fit functions. The list of gamma peak values, their calculated visible energies, and the corresponding reconstructed energies are summarized in Table. 1. We remark some points below:

- The ^{68}Ge and ^{60}Co sources release two correlated gamma-rays. The detector sees them as a single flash of light.
- Neutron captures on ^{12}C has 32% chance of emitting two γ 's ($3.684 + 1.262\text{MeV}$) instead of one (4.945 MeV).
- Neutron captures on ^{155}Gd and ^{157}Gd release a multitude of correlated gamma-rays with total energy ~ 8.05 MeV. The gamma multiplicity is about 3.
- An energetic neutron (e.g. from a neutron source) can excite the ^{12}C nuclei to the first excited state, $^{12}\text{C}^*$, which then de-excites and releases a single gamma of 4.44 MeV. However this peak is in general contaminated by the proton recoil from neutron elastic scattering, which needs to be estimated and subtracted.
- If gamma peaks are from the delayed neutron captures, for example the $n^1\text{H}$ and $n^{12}\text{C}$ cases, the proton recoils serve as the prompt signals thus do not affect the delayed capture energy releases.

Table 1. Gamma Peaks for Energy Calibration, where E_{true} is the true energy of the gamma(s), E_{vis} is the ‘visible’ energy calculated assuming a set of Birks’ constant and Cerenkov radiation and E_{rec} is the reconstructed energy seen from the data. Results are taken from Ref. [4].

Sources	E_{true} [MeV]	E_{vis} [MeV]	E_{rec} [MeV]	δE_{rec} [MeV]
^{137}Cs	0.662	0.633	0.634	6.6×10^{-3}
^{54}Mn	0.835	0.819	0.819	8.5×10^{-3}
^{68}Ge	0.511×2	0.952	0.955	10.0×10^{-3}
^{40}K	1.461	1.506	1.469	4.9×10^{-3}
$n^1\text{H}$ (PuC)	2.223	2.389	2.287	7.2×10^{-3}
$n^1\text{H}$ (AmBe)	2.223	2.389	2.291	7.2×10^{-3}
^{60}Co	$1.173 + 1.333$	2.549	2.453	14.2×10^{-3}
^{208}Tl	2.615	2.841	2.710	15.8×10^{-3}
$^{12}\text{C}^*$ (PuC)	4.439	5.149	4.769	50×10^{-3}
$^{12}\text{C}^*$ (AmBe)	4.439	5.629	4.982	194×10^{-3}
$n^{12}\text{C}$ (PuC)	4.945	5.552	5.114	3.1×10^{-3}
$n^{12}\text{C}$ (AmBe)	4.945	5.552	5.117	16.7×10^{-3}
$^{56}\text{Fe}^*$	5.970	6.789	6.07	64×10^{-3}
$^{16}\text{O}^*$	6.129	8.753	6.342	20×10^{-3}
$n^{56}\text{Fe}$	7.630	10.102	7.842	82×10^{-3}
$n\text{Gd}$ (IBD)	$\Sigma = 8.047$	8.841	8.026	24×10^{-3}

1.4.2 Alpha Energy Points

There are five α -decays that can be extracted from the data easily. Four of them can be extracted using the prompt-delayed coincidence technique same as how we extract ^{212}Bi and ^{214}Bi β -decays. Fig. 7(a) shows the prompt *v.s* delayed energy for any coincident events with coincidence time less than 400 μs (doc:7220 [5]). Region A, B, C are from accidental coincidence, but region D, E are real coincidence decays:

- *Region C*: ^{219}Rn α -decays ($E_\alpha = 6.946$ MeV) to ^{215}Po , ^{215}Po then α -decays ($E_\alpha = 7.526$ MeV) to ^{211}Pb with half life $\tau_{1/2} = 1.781\text{ms}$.
- *Region D*: ^{214}Bi β -decays ($Q = 3.272$ MeV) to ^{214}Po . ^{214}Po then α -decays ($E_\alpha = 7.687$ MeV) with half-life $\tau_{1/2} = 164\mu\text{s}$.
- *Region E*: ^{212}Bi ($Q = 2.252$ MeV) β -decays to ^{212}Po . ^{212}Po then α -decays ($E_\alpha = 8.784$ MeV) with half-life $\tau_{1/2} = 0.299\mu\text{s}$.

^{212}Bi and ^{214}Bi come from the ^{232}Th and ^{238}U decay chains. ^{219}Rn is believed to be coming from ^{227}Ac , which is a contamination in the Gadolinium salt. The energy peak of those four α -decays are shown in Fig. 7(b). In addition, the ^{210}Po α -decay ($E_\alpha = 5.407$ MeV) peak is obvious on the singles spectra, which comes from internal ^{210}Pb contamination. The reconstructed energy of the α peaks are listed in Table. 2

Table 2. Alpha Peaks for Energy Calibration

Sources	E_{true} [MeV]	E_{rec} [MeV]
^{210}Po	5.304	0.513
^{219}Rn	6.819 (79.4%)	0.795
	6.553 (12.9%)	
^{215}Po	7.386	0.911
^{214}Po	7.686	0.975
^{212}Po	8.784	1.217

1.4.3 Continuous Spectra

^{12}B The ^{12}B spectra used in constructing the energy model was produced by Y. Meng (VT) [6]. Her analysis was cross checked by P. K. V. Tsang (LBNL) [7] and F. H. Zhang (IHEP) [8]. Fig. 8 (made by F. H. Zhang) shows the comparison of F. H. Zhang’s and Y. Meng’s ^{12}B spectra. The comparison of ^{12}B spectra from these two analyses are shown in Fig. 9 (made by F. H. Zhang).

^{212}Bi and ^{214}Bi The selection of ^{212}Bi and ^{214}Bi beta spectra is described in details in Ref. [9]. We briefly summarize the procedure here:

- Initial Skim:

The energy of prompt signal and delay signal are constrained to be 0.5-3.0 MeV and 0.7-2.0 MeV, respectively. The time difference between prompt and delay is smaller than 400 μs . The time to the previous water pool muon is required to be larger than 0.6 ms.

- ^{212}Bi selection:

The energy of the prompt signal is from 0.5 to 3.0 MeV. The energy of the delay signal is from 1.1 to 1.4 MeV. Standard flasher cuts are applied. A fiducial volume cut ($R < 1 \text{ m}$ and $-0.5 \text{ m} < z < 0.5 \text{ m}$) is applied. The time difference between prompt and delay signals is between 1 and 4 μs . The background window is selected to be 4-10 μs .

- ^{214}Bi selection:

The energy of the prompt signal is from 1.3 to 3.0 MeV. The energy of the delay signal is from 0.85 to 1.15 MeV. Standard flasher cuts are applied. A fiducial volume cut ($R < 1 \text{ m}$ and $-0.5 \text{ m} < z < 0.5 \text{ m}$) is applied. The time difference between prompt and delay signals is between 10 and 200 μs . The background window is selected to be 210-400 μs .

The final spectra are shown in Fig. 10.

^{208}Tl The spectra of ^{208}Tl are from B. Littlejohn [10]. Standard muon vetos including both shower muon veto, AD muon veto, and Water Pool (WP) muon veto are applied. An additional vertex cut ($R < 1 \text{ m}$ and $-0.5 \text{ m} < Z < 0.5 \text{ m}$) is used. The spectra of ^{208}Tl are shown in Fig. 11.

1.5 Summary of Birks’ Law Based Energy Model

The purpose of the non-linearity model is to build up a relationship between the reconstructed energy E_{rec} and the true kinetic energy E_{true} of a given particle. We can describe such relationship

as two independent factors:

$$\begin{aligned}\frac{E_{rec}}{E_{true}} &= \frac{E_{vis}}{E_{true}} \cdot \frac{E_{rec}}{E_{vis}} \\ &= f_1(E_{true}) \cdot f_2(E_{vis}),\end{aligned}\tag{1.2}$$

where E_{vis} is the ‘visible’ energy of the particle which represents the total amount of light (or photoelectrons) seen by the PMTs. In this way we expect f_1 to be a function of E_{true} that is determined by the physics processes such as scintillation and Cerenkov radiation, while f_2 being a function of E_{vis} that is determined by the photosensors and electronics effects (e.g. in a perfect linear electronics system, f_2 equals unity.)

We can now build a physics based non-linearity model by introducing a few parameters to describe each effect:

$$\frac{E_{rec}}{E_{true}} = a \cdot [f_q(E_{true}; k_B) + k_c \cdot f_c(E_{true})] \cdot f_e(E_{vis}; k_0, k_1, k_2),\tag{1.3}$$

where a (since a is not 1) is a scaling factor set by the the *AdSimple* reconstruction such that the reconstructed energy from spallation neutron capture on Gd is the same as the true energy (weighted peak at 8.047 MeV). The three terms f_q , f_c and f_e represent the non-linear effects from scintillator quenching, Cerenkov radiation and the electronics non-linearity, respectively. In the following detailed discussion, we first calculate the scintillation and Cerenkov contribution for electrons, then convert the electron non-linearity to gammas and positrons, and finally apply the electronics effects.

Scintillator Quenching Scintillator quenching represents the effect that the light-output is suppressed due to the interactions between the excited molecules along the path of the incident particle, which drain energy that would otherwise go into fluorescence photons. This quenching effect is more pronounced for high ionizing power particles such as α particles, since they would produce a higher density of excited molecules. Equation *Birks’ formula* semi-empirically describe the quenching effect as follows:

$$\frac{dL}{dx} \propto \frac{dE/dx}{1 + k_B \cdot (dE/dx) + c \cdot (dE/dx)^2}\tag{1.4}$$

where dL/dx and dE/dx are the light output per unit length and the particle stopping power respectively. k_B is called *Birks’ constant* and is dependent on the material. The constant c that is associated with the second order dE/dx is set to zero. The quenching effect of electrons is rather insensitive to this term, while the quenching effect of alphas is sensitive to this term. One can see for large dE/dx the light output is saturated and is only related to the particle range.

From the Birks formula shown in Eq. 1.4 we can then calculate the scintillator quenching term $f_q(E_{true}; k_B)$ which is a function of the true energy of the particle and the Birks’ constant k_B :

$$f_q(E_{true}; k_B) = \frac{1}{E_{true}} \cdot \int_0^{E_{true}} \frac{dE}{1 + k_B \cdot \frac{dE}{dx}}.\tag{1.5}$$

The dE/dx tables for electron are obtained from the NIST database (ESTar: <http://physics.nist.gov/PhysRefData/Star/Text/ESTAR.html>). We further assume that the

dE/dx are the same between electron and positron. There has been good progress in validating this assumption. For example, Ref. [11] shows that the effect of positron annihilation on flight is negligible. The dE/dx tables for proton and alpha are obtained from SRIM program (<http://www.srim.org/SRIM/SRIM2011.htm>). The dependence of dE/dx with respect to E_{true} for various particles are shown in Fig. 12. Eq. 1.5 can be applied directly to proton and alpha. For electron/positron, the situation is more complicated, since dE/dx also involves a contribution from radiation. In general, the radiation energy is emitted in the format of photons peaked at low energy [12], which would further deposit energy in the liquid scintillator through electrons (Compton scattering) or electron-positron pairs (pair production). In both cases, the energy of electron/positron will be much lower than that of the incident electron. Therefore, the energy released through radiation will suffer from strong quenching. In an extreme case, we can assume that the radiation energy is totally quenched, e.g.

$$f_q(E_{true}; k_B) = \frac{1}{E_{true}} \cdot \int_0^{E_{true}} \frac{\frac{\partial E_{collision}}{\partial E_{collision+radiation}} \cdot dE_{collision+radiation}}{1 + k_B \cdot \frac{dE}{dx}|_{collision}}. \quad (1.6)$$

We show the results of two quenching models (Eq. 1.5 vs. Eq. 1.6) in Fig. 13 assuming $k_B = 6.4 \times 10^{-3} \text{ cm/MeV}$.

Cerenkov Radiation Cerenkov radiation is emitted when a particle travels in a medium faster than the speed of light in the same medium. The Cerenkov radiation is an electromagnetic shock wave, whose coherent wavefront is conical in shape and is emitted at a well-defined angle $\cos \theta_c = c/(n \cdot v)$ with respect to the track of the particle, where c is the speed of light in vacuum and n is the index refraction of the medium. The Cerenkov light term $f_c(E_{true})$ is a function of the true particle energy and is calculated from the NuWa full detector simulation. In addition, the Cerenkov contribution can also be calculated given the dE/dx as well as the index of refraction $n(\omega)$:

$$E_{Cerenkov} \propto \int_{\omega_1}^{\omega_2} \int_{E_{true}}^{E_f} \frac{\alpha}{\frac{dE}{dx}|_{collision+radiation}} \cdot \left(1 - \frac{1}{\beta^2(E_e) \cdot n^2(\omega)} \right) dE_e d\omega, \quad (1.7)$$

where α is the fine structure constant. The ω_1 and ω_2 are the frequencies of Cerenkov optical photon. They represent the boundary of the region of interests, in which Cerenkov light will be detected by detector. The index of refraction $n(\omega)$ normally depends on the frequency of Cerenkov light. E_f , a function of ω , represents the energy threshold to emit Cerenkov light. $\beta(E_e)$ is the speed of electron given energy E_e . The constant k_c represents the detector's efficiency in collecting the Cerenkov photons and is allowed to be free floating. The shape of the $f_c(E_{true})$ term obtained from NuWa is shown in Fig. 14². In Fig. 15, $f_c(E_{true})$ term obtained from Nuwa is compared with that calculated using Eq. 1.7 for electrons. The results are in good agreement. We denote the sum of scintillator quenching and Cerenkov radiation effects as the total visible energy E_{vis} . In Fig. 16, we show the effect of Cerenkov contribution ($\sim 8.3\%$ at 1 MeV electron energy).

Converting electron non-linearity to gammas and positrons After calculating the E_{vis} curve for electrons, we follow doc:8240 [13] to convert it to gammas and positrons. For a gamma particle, it has to convert to a charged particle (electron or positron) to lose energy. There are three major processes that it loses energy:

²Only the electron Cerenkov curve is used in the analysis, with a free floating amplitude.

- Compton scattering ($\gamma \rightarrow \gamma + e^-$)
- Photoelectric effect ($\gamma \rightarrow e^-$)
- Pair production ($\gamma \rightarrow e^- + e^+$)

Using a Geant4 simulation to record all the interaction processes of an initial gamma particle, we can obtain the probability density function (p.d.f) of the primary charged particles (i.e. we do not further track the process from the primary charged particles³) from the gamma interaction. Once the gamma is converted to a charged particle, this charged particle behaves in the same scintillation and Cerenkov process as we describe above. We further assume that electrons and positrons interact the same way in matter, which is reasonable for the purpose of our study. Fig. 17 illustrates the resulting p.d.f of the primary charged particles. For a gamma particle with E_{true} , we then calculate the corresponding E_{vis} as follows:

$$E_{vis}^\gamma = \int E_{vis}^e \cdot \frac{dN}{dE}(E_{true}^e) \cdot dE_{true}^e, \quad (1.8)$$

where $\frac{dN}{dE}(E_{true}^e)$ is the p.d.f of the primary charged particles.

For positrons, we simply assume that it's the same as electrons except the additional two 0.511 MeV gammas at the annihilation.

$$E_{vis}^{e^+} = E_{vis}^{e^-} + 2 \cdot E_{vis}^{\gamma|0.511MeV} \quad (1.9)$$

Fig. 18 shows the converted E_{vis}/E_{true} curves for electrons, gammas, positrons, protons, and alphas.

Electronics Non-linearity We attribute the difference between the data points and the gamma non-linearity prediction in Fig. 18 to the electronics non-linearity effects. In the energy reconstruction, for each PMT, only the charge (integrated by FEE for ~ 100 ns) from the first hit in a fixed time window was used. It was shown in doc:8493 [14] and doc:8364 [15] that due to the slow component of the scintillation light, this charge selection is by-construction biased. A decreasing charge collection efficiency as a function of total number of photoelectrons is predicted. This however may not be the sole origin of the electronics non-linearity. Recently, it is pointed out in doc:8907 [16] that the signal shaping would also introduce additional electronics non-linearity.

We expect that the electronics non-linearity only depends on the total energy visible in the detector E_{vis} , since that's what's been ‘seen’ by the PMTs. For each gamma peak data point, we can predict E_{vis} with the scintillator quenching and Cerenkov radiation model described earlier. We then plot the E_{rec}/E_{vis} for each gamma peak data point as shown in Fig. 19, including those with multiple gammas such as ^{60}Co and neutron capture on Gd. Interestingly, a smooth decreasing trend as a function of E_{vis} showed up. We model the electronic non-linearity using the following formats:

$$\begin{aligned} f_e(E_{vis}; k_0, k_1, k_2) &= k_0 + k_1 * E_{vis} + k_2 * E_{vis}^2 \quad (E_{vis} \leq -\frac{k_1}{2k_2}) \\ f_e(E_{vis}; k_0, k_1, k_2) &= k_0 - \frac{k_1^2}{4k_2} \quad (E_{vis} > -\frac{k_1}{2k_2}). \end{aligned} \quad (1.10)$$

³Except for the positron from pair production, the two annihilation gammas are tracked until they are converted to electrons.

1.6 Description of Nominal Model

1.6.1 Additional Constrains

Birks' constant For different types of liquid scintillators, the Birks' constants are normally different. For KamLAND (20% pseudocumene + 80% dodecane with 1.36g/L PPO wavelength shifter), the Birks' constant is measured to be 13.8×10^{-3} cm/MeV [17]. In Ref. [18], Birks' constant is measured to be 7.4×10^{-3} cm/MeV for the scintillator used in SNO (LAB+PPO). In Ref. [19], Birks constant is measured to be about 9.5×10^{-3} cm/MeV for LAB+PPO scintillator. The measurement of the Birks' constant of the Daya Bay Gd loaded scintillator is summarized in Ref. [20]. The resulting Birks' constant is $7.5 \pm 1.2 \times 10^{-3}$ cm/MeV. Furthermore, it is pointed out in Ref. [21], that the Birks' constant could be different given same type of liquid scintillator for different particle types.

Despite the wide range of possible values of Birks' constant, Daya Bay alpha data (tabulated in Table. 2) can provide a good constrain of the Birks' constant assuming the Birks' constant is universal for all particles. Fig. 20 shows the Daya Bay alpha data together with quenching models assuming $k_B = 6.4 \times 10^{-3}$ cm/MeV and $k_B = 7.4 \times 10^{-3}$ cm/MeV. In our quenching models, the electronics non-linearity is obtained by fitting the gamma calibration data, which is described in Sec. 1.5). Due to smaller ratio of fast over slow scintillation decay components for α , one expects additional electronics non-linearity to reduce the light yield. Although we have not worked out the exact strength of this additional electronics effect, the data clearly favor a quenching model with $k_B = 6.4 \times 10^{-3}$ cm/MeV over a quenching model with $k_B = 7.4 \times 10^{-3}$ cm/MeV (Fig. 20). Therefore, we chose Birks' constant to be 6.4×10^{-3} cm/MeV in our nominal model.

Cerenkov contribution The Cerenkov contribution in the visible energy of electron also depends on the types of liquid scintillator. This is mainly due to the existence of wavelength shifter, which can convert Cerenkov light outside the range of visible light into the range of visible light. For KamLAND, the Cerenkov contribution is determined to be about 4.5% for 1 MeV electron [17]. In Ref. [18], the Cerenkov contribution is determined to be about 15% for 1 MeV electron for the scintillator used in SNO (LAB+PPO). In this work, the nominal Cerenkov contribution is chosen to be about 8.3% for 1 MeV electron. This choice is constrained by bench Compton scattering measurement [22]⁴ (Fig. 21, and the Daya Bay gamma calibration data. A too large (e.g. 15%) or a too small (e.g. 4%) Cerenkov contribution would lead to a discrepancy between gamma calibration data and the best fitted smooth electronics non-linearity function [23].

1.6.2 Nominal Model

Fig. 18 shows our nominal scintillator energy non-linearity model with $k_B = 6.4 \times 10^{-3}$ cm/MeV. Fig. 19 shows our nominal effective electronics non-linearity model. The best matched parameters are tabulated in Table. 3. In order to obtain the final non-linearity model, we assume that the electronics non-linearity is the same between electron, gamma and positron, since they have similar scintillation light decay distribution.

⁴The Compton scattering measurement utilizes the gamma sources as beam, and uses the Compton scattered gamma in order to tag the recoil electrons. The energy of the recoil electrons can be calculated with the incident gamma energy as well as the angle of the scattered gamma. Therefore, one can use this technique to study the energy response of liquid scintillator.

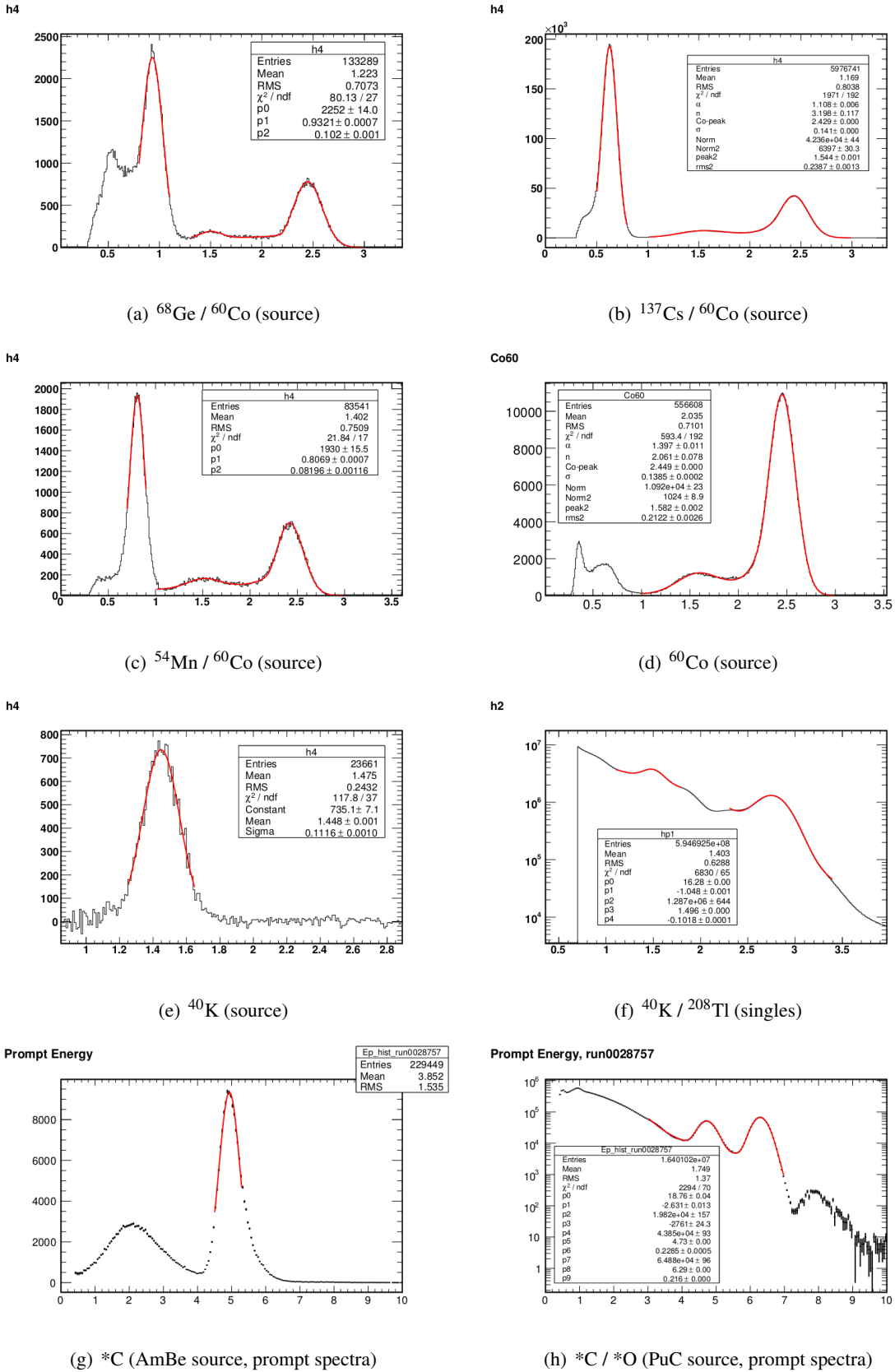


Figure 4. Energy spectra of various gamma peaks used for non-linearity study.

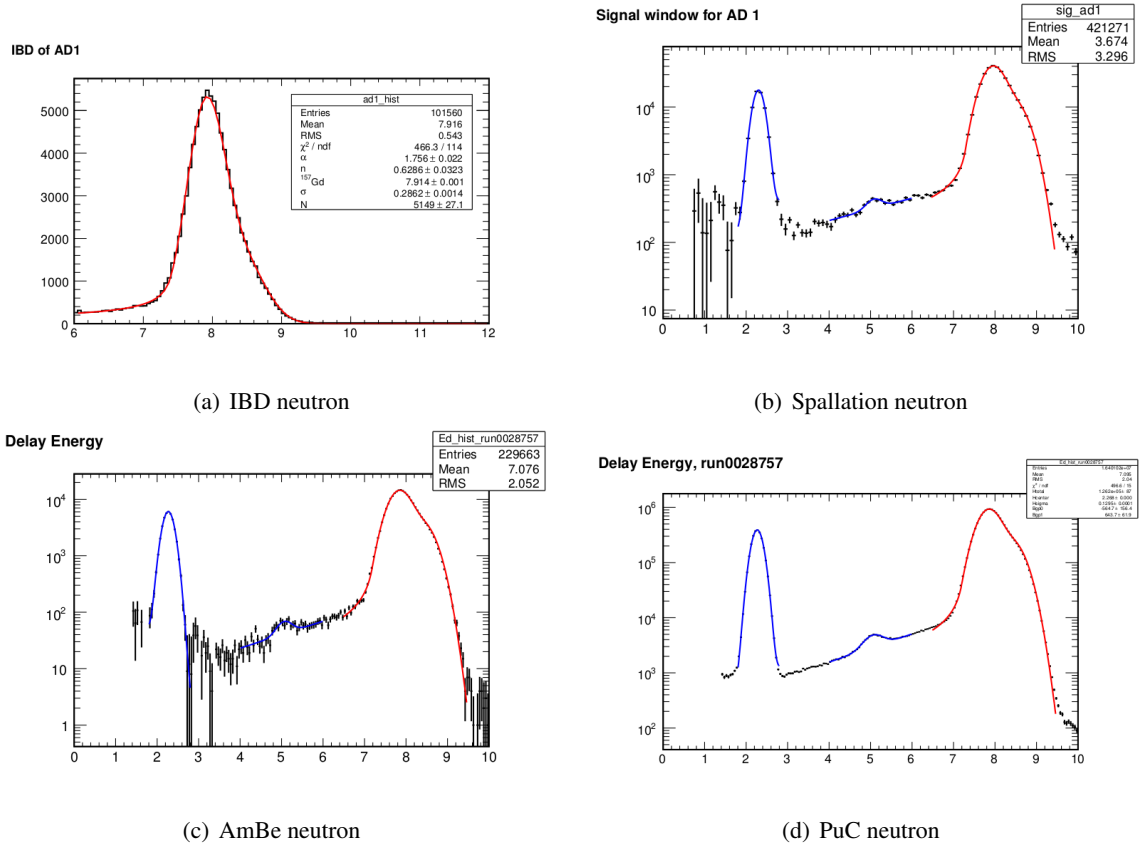


Figure 5. (n,γ) peaks from neutron capture on Gd, ^1H , ^{12}C with various neutron samples.

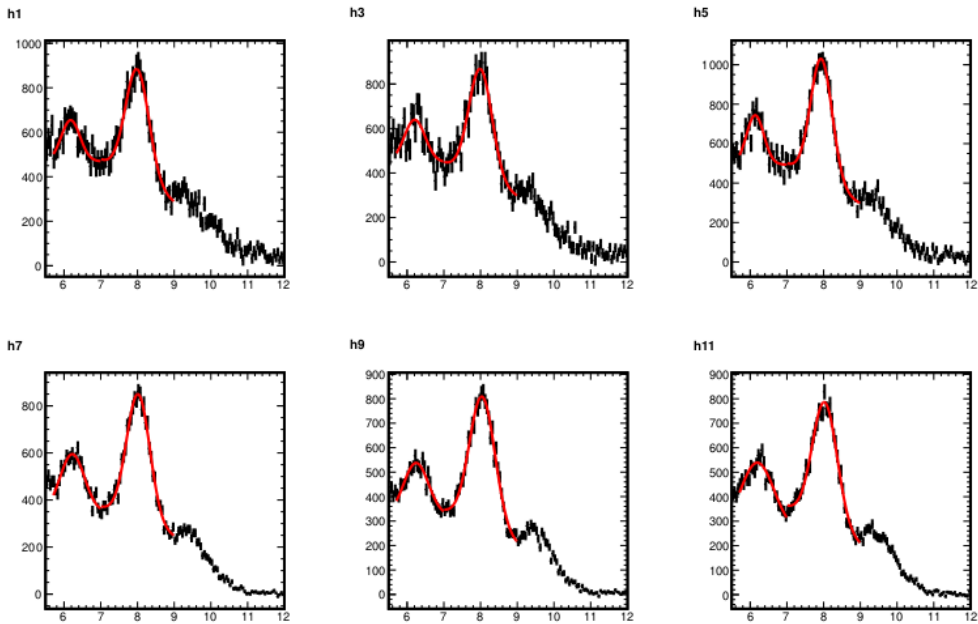
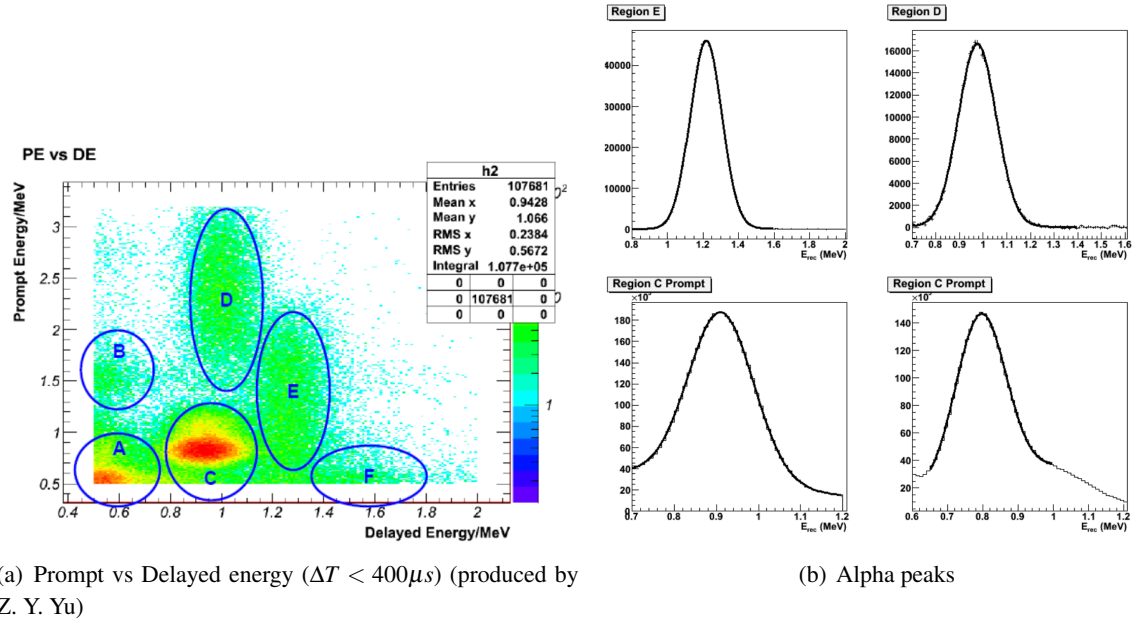


Figure 6. External gamma-ray from neutron capture on stainless steel in the 6 ADs.



(a) Prompt vs Delayed energy ($\Delta T < 400\mu s$) (produced by Z. Y. Yu)

(b) Alpha peaks

Figure 7. Alpha-decay selection and peak spectra

Selection Criteria	FeiHong's	Yue's
Energy	Enrec in AdScaled default charge, Co energy scale	AdSimple default charge
Flasher cut	Same as IBD	Same except not applied on Muons
Muon veto	Same as IBD except shower muon changed to 1ms	200us WS muon veto
Isolation cut	Yes	Yes
Vertex cut	1.5 m	1.5 m
Signal window	1ms to 100ms	1ms to 100ms
Bkg. window	401ms to 500ms	501 to 600ms

Figure 8. Comparison of ^{12}B selection criteria (made by F. H. Zhang).

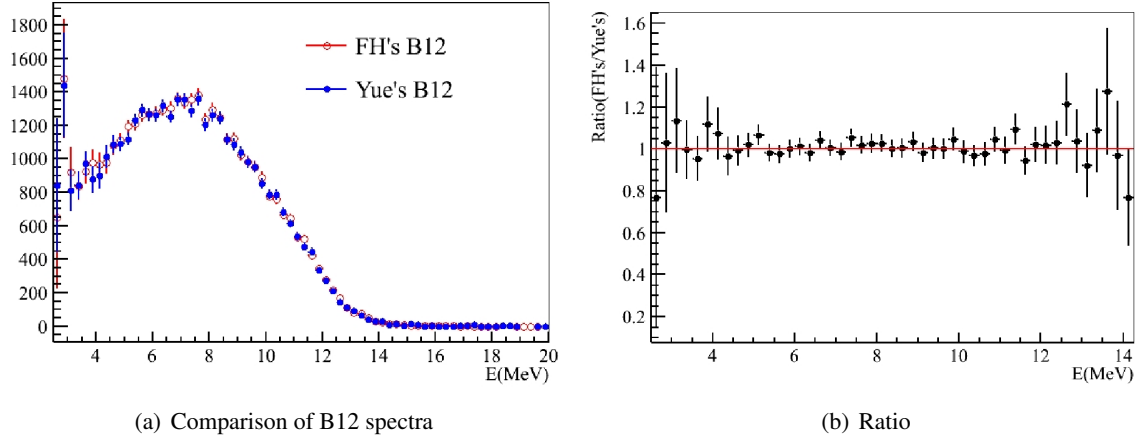


Figure 9. Comparison of ^{12}B spectra from F. H. Zhang and Y. Meng (made by F. H. Zhang).

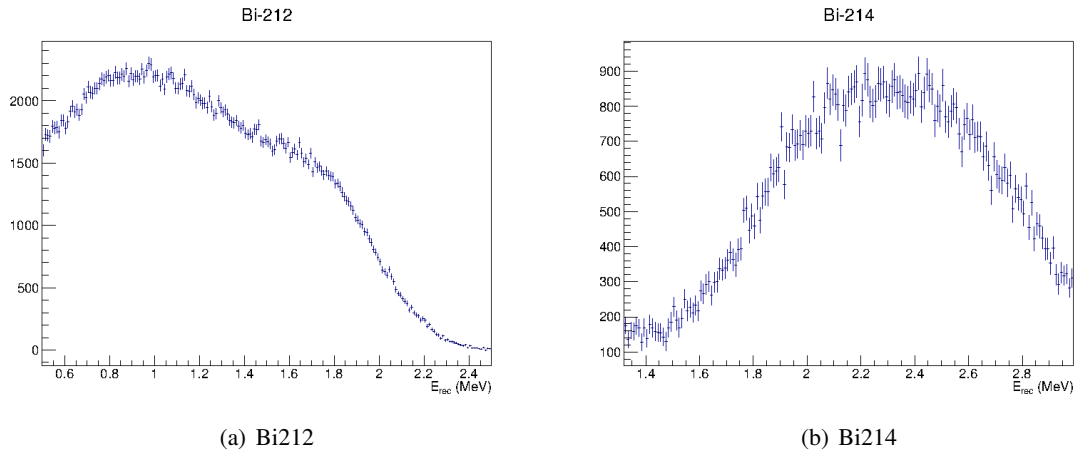


Figure 10. The ^{212}Bi and ^{214}Bi spectra are shown.

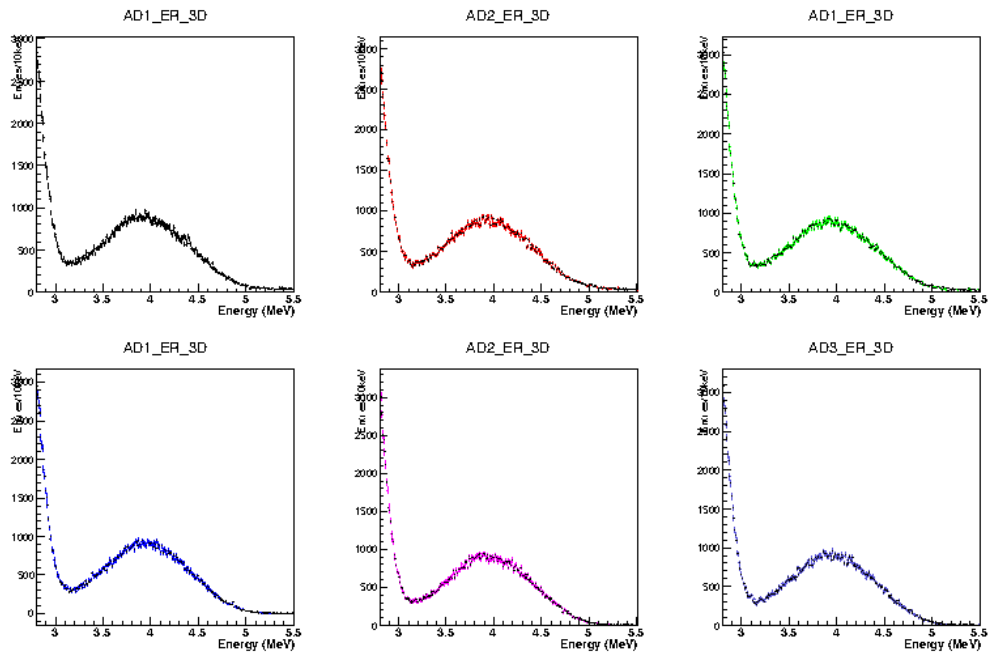


Figure 11. ^{208}Tl spectra (made by B. Littlejohn).

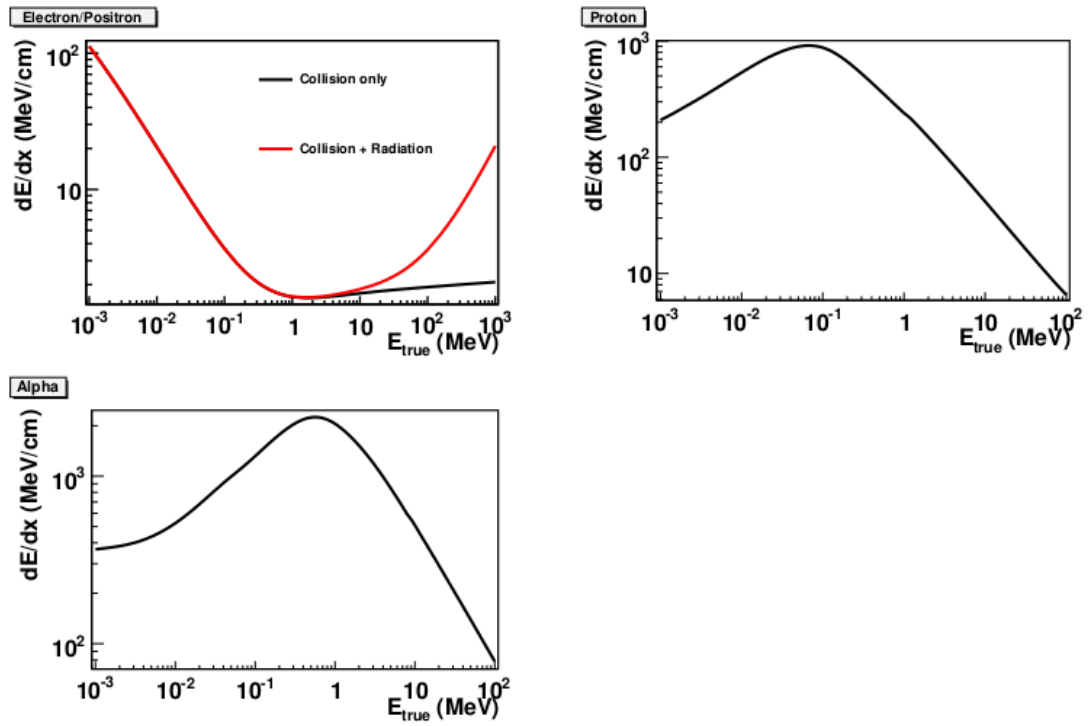


Figure 12. dE/dx for various particles.

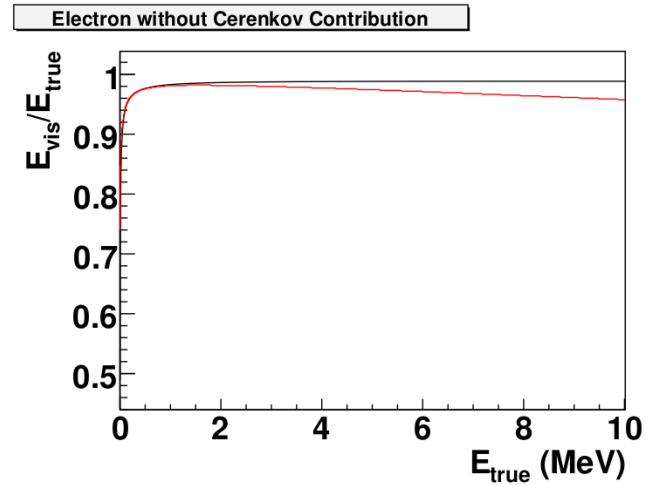


Figure 13. Comparison of two quenching models, Eq. 1.5 (black) vs. Eq. 1.6 (red), with $k_B = 6.4 \times 10^{-3}$ cm/MeV.

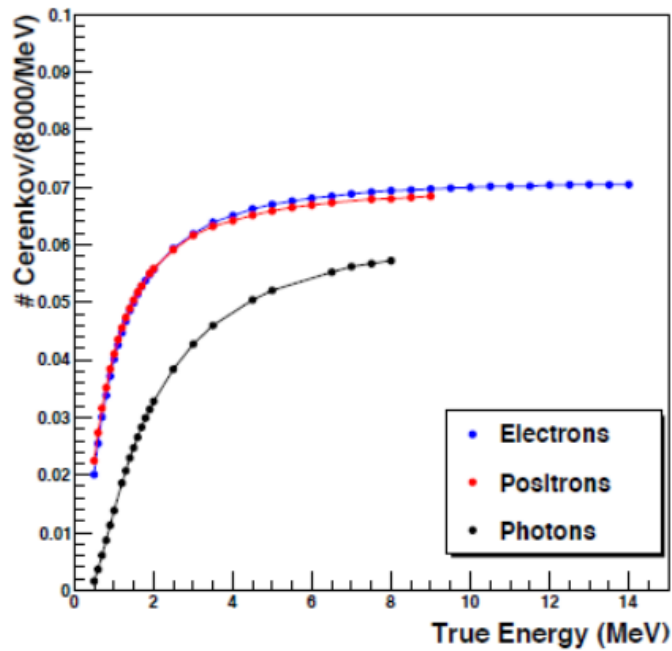


Figure 14. Cerenkov non-linearity (made By E. Worcester).

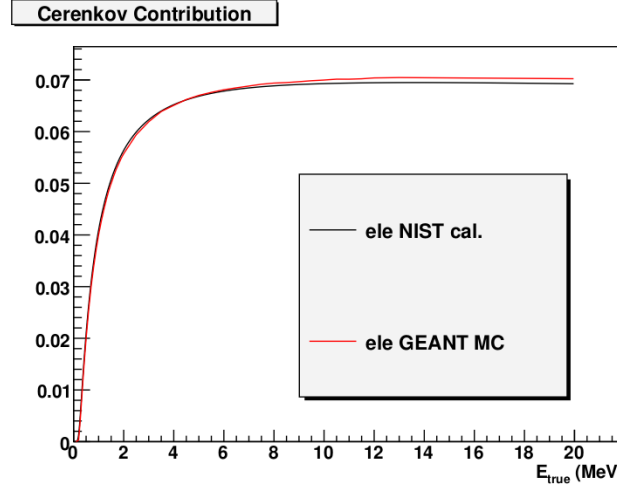


Figure 15. Cerenkov shape comparison of MC (NuWa) and direct calculation for electron.

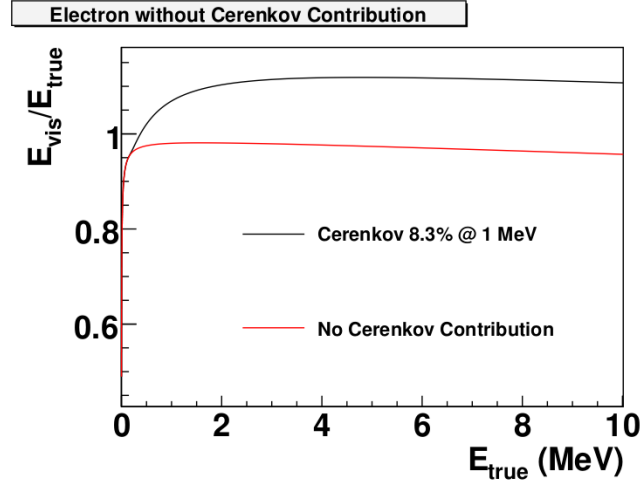


Figure 16. Effect of Cerenkov contribution. Eq. 1.6 is assumed as the quenching model with $k_B = 6.4 \times 10^{-3}$ cm/MeV.

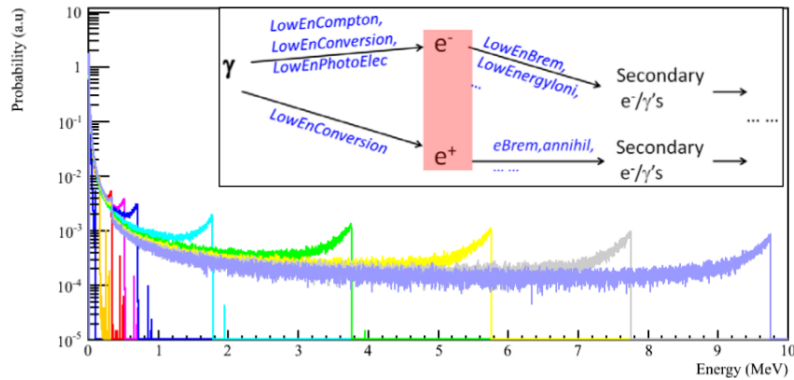


Figure 17. Converting electron non-linearity to gamma and positron (made by L. J. Wen).

Nominal BCW quenching model

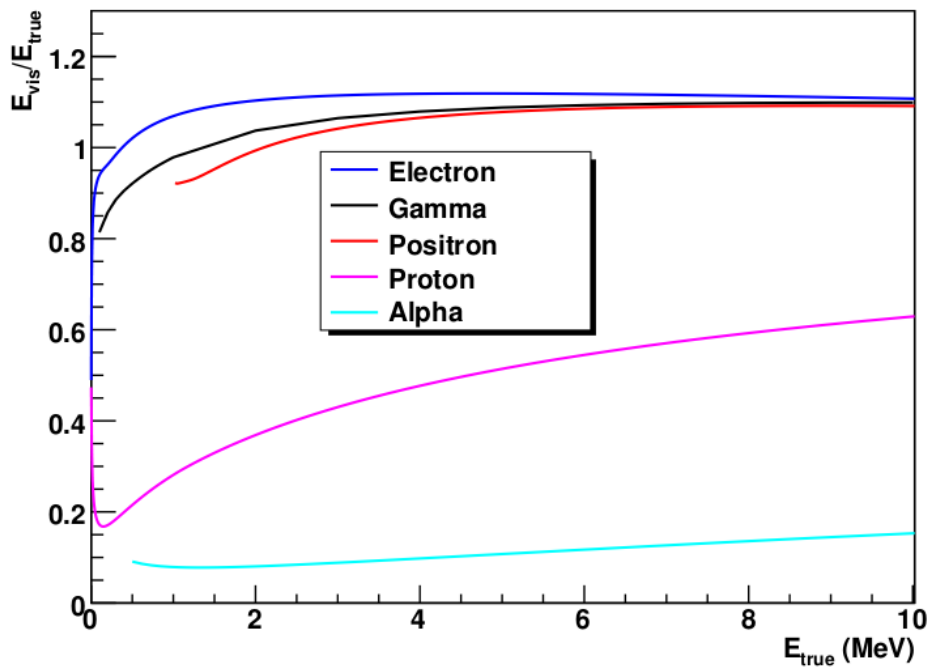


Figure 18. The detector non-linearity from scintillator quenching plus Cerenkov radiation. Eq. 1.6 is assumed as the quenching model with $k_B = 6.4 \times 10^{-3}$ cm/MeV.

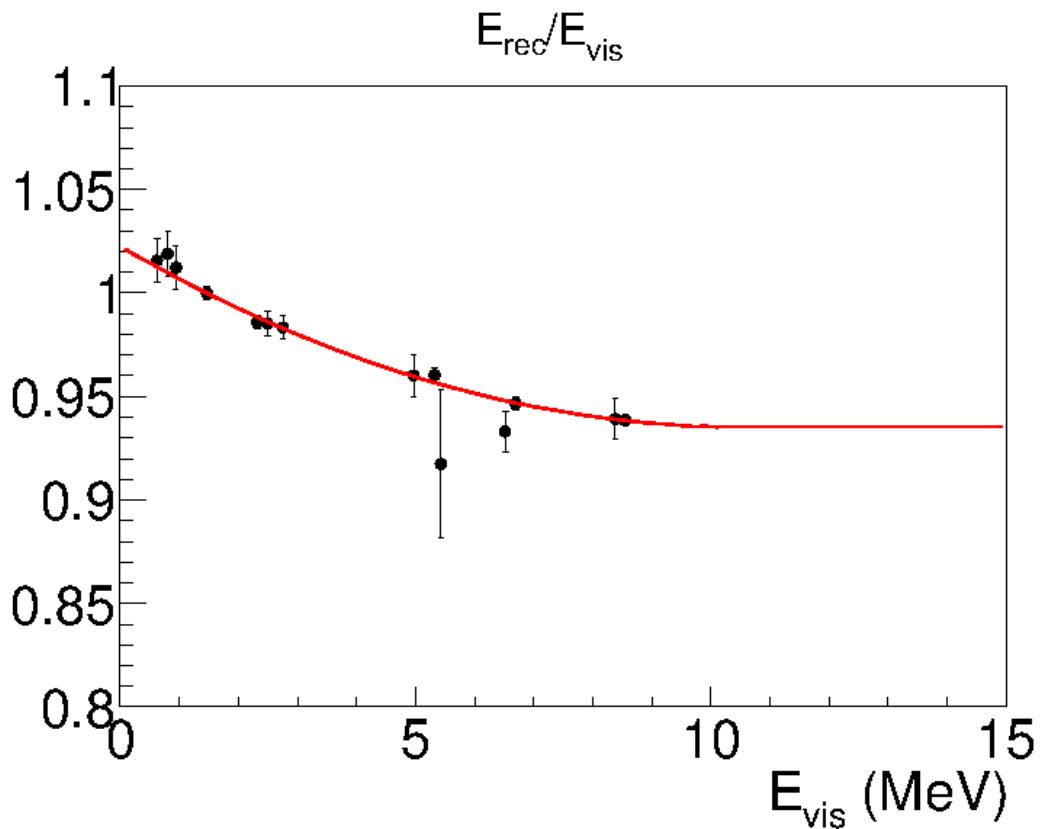


Figure 19. Electronics non-linearity. Eq. 1.6 is assumed as the quenching model with $k_B = 6.4 \times 10^{-3}$ cm/MeV. The functional form of electronics non-linearity is assumed to be Eq. (1.10).

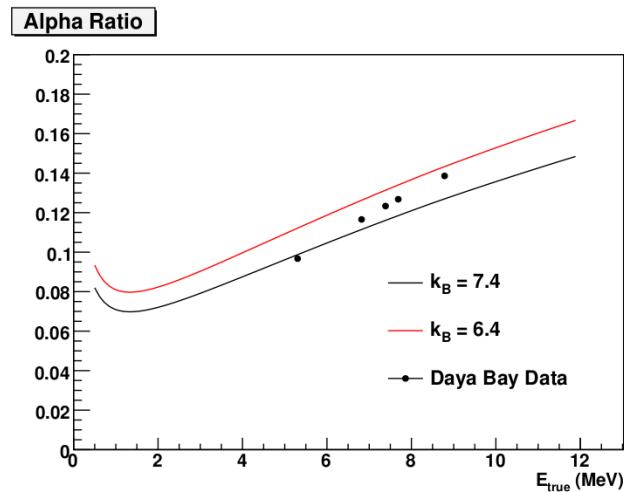


Figure 20. Comparison of Daya Bay alpha data with quenching model ($E_{\text{rec}}/E_{\text{true}}$). Alpha data favors $k_B = 6.4 \times 10^{-3}$ cm/MeV over $k_B = 7.4 \times 10^{-3}$ cm/MeV. See text for more explanations.

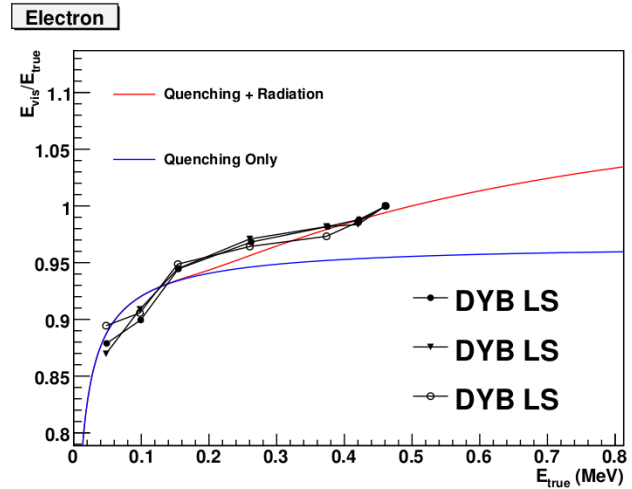


Figure 21. Comparison of Daya Bay bench Compton scattering measurement [22] with quenching model (E_{rec}/E_{true}). The nominal Cerenkov contribution is chosen to be 8.3% for 1 MeV electron.

Table 3. Best matched values of energy non-linearity parameters

Parameter	Best-fit Value	Uncertainty (%)
k_B	0.0064 [cm/MeV]	0
k_c	8.3% [@ 1 MeV]	0
k_0	1.0226	0.0047
k_1	$-0.01654 [\text{MeV}^{-1}]$	0.0024
k_2	$0.0007830 [\text{MeV}^{-2}]$	0.0002409

Nominal BCW nonlinearity model

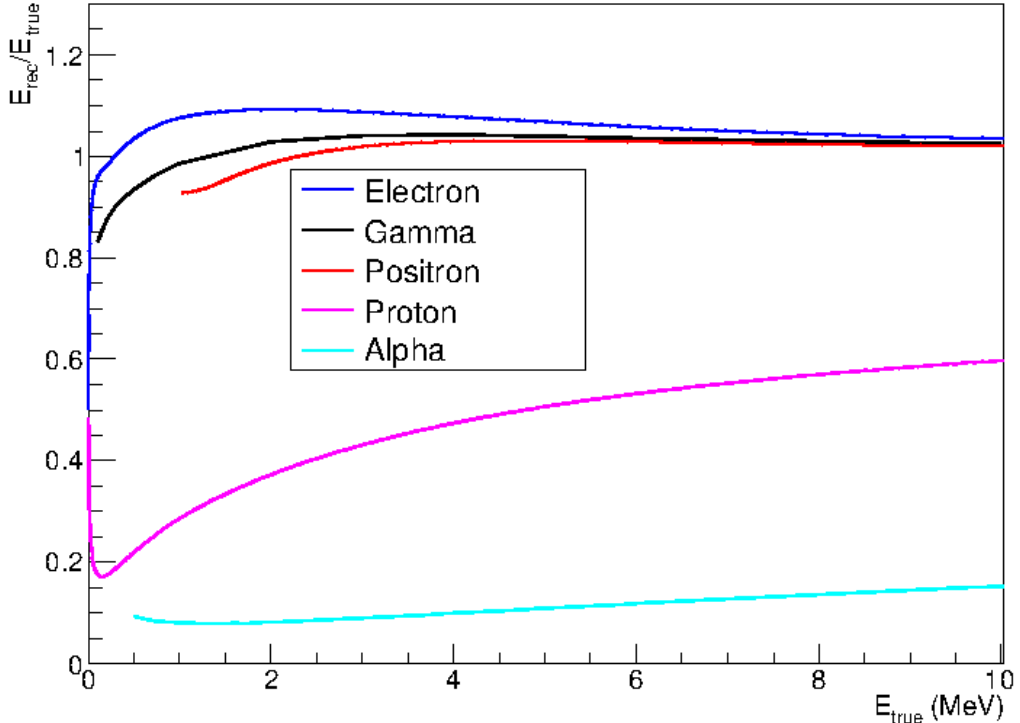


Figure 22. Effective energy non-linearity.

Putting all terms together as in Eq. 1.3, we obtain the final ‘effective’ non-linearity curves as shown in Fig. 22.

1.6.3 Validating Energy Model With $\beta + \gamma$ Spectra

Since gamma calibration data has been used to constrain the effective electronics non-linearity (Fig. 19), our model naturally describe the gamma calibration data well. As can be seen from Fig. 22, the effective non-linearity model predicts very different behavior for electrons, gammas and positrons. The model was constructed from gamma peak data points. If the model is correct, it should be able to describe the electrons in our detector as well. Eventually for IBD analysis we will use the positron non-linearity curve which is a combination of electrons and gammas. Four

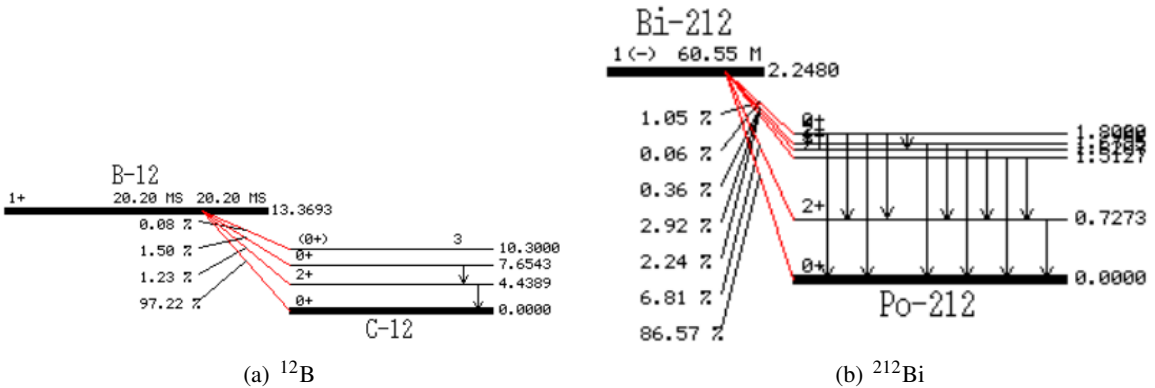


Figure 23. Beta Decay Scheme I (from <http://atom.kaeri.re.kr>)

relatively clean and high statistics $\beta^- + \gamma$ spectra (^{12}B , ^{208}Tl , ^{212}Bi and ^{214}Bi) are extracted from data and used to validate the BCW energy model.

The decay schemes for the four nuclei are shown in Fig. 23 and Fig. 24. The theory of beta decay is reviewed in Ref. [24]. The procedure to predict expected spectrum including both electron/positron and gammas is described in Ref. [25], and briefly summarized here. The corrections applied in the theoretical spectra include: Coulomb correction (Fermi function), screening correction, finite-size EM correction, finite-size weak interaction correction, weak magnetism correction, and forbidden decay shape correction. For allowed decay, we implement Fermi/screening/finite-size/weak magnetism corrections. For first forbidden non-unique decay, we assume the shape follows that of allowed decay. We then implement the Fermi/Screening corrections. For the other forbidden decays (up to fifth order unique, or second order non-unique), we implemented the Fermi/screening/finite-size/weak magnetism/forbidden corrections.

To predict the visible spectra in the detector, we adopt the following procedure:

- Calculate the beta decay spectra given the branching ratio (B.R) and Q-value of each beta decay branch.
- For each beta decay branch, obtain the information about the correlated gamma decays
- Apply scintillator quenching and Cerenkov radiation non-linearity to the e^- and γ 's separately (Fig. 18.)
- Apply electronics non-linearity to the total visible energy (Fig. 18).
- Apply energy resolution function (Eq. 1.1.)
- The above procedure predicts the shape of the visible spectra. The overall rate normalization is allowed to be free.

^{212}Bi , ^{214}Bi and ^{208}Tl Spectra ^{208}Tl is the daughter nuclei from the ^{232}Th decay chain. ^{212}Bi and ^{214}Bi are the daughter nuclei from the ^{232}Th and ^{238}U decay chains, respectively. Furthermore, it is worth pointing out the limitations in the theoretical prediction of the spectra. Form ^{212}Bi , all

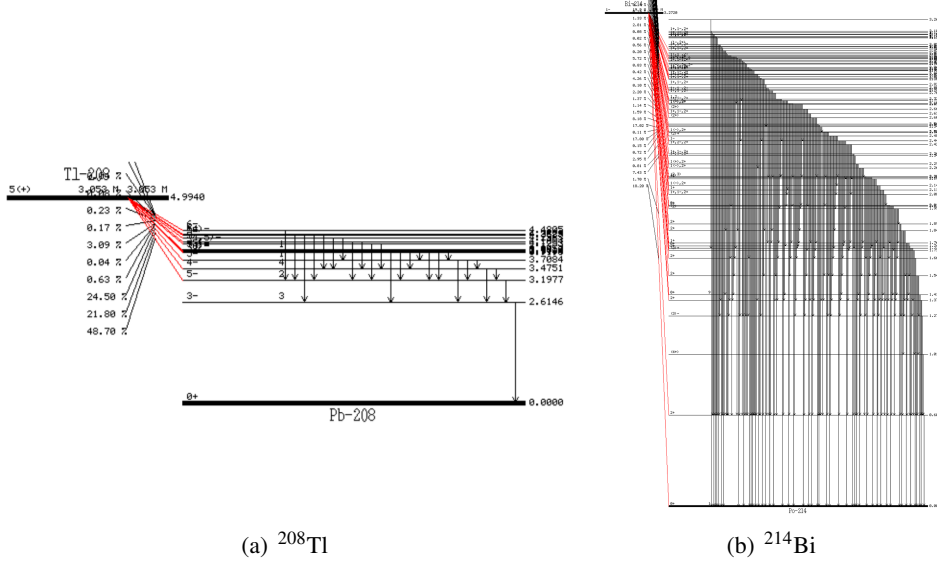


Figure 24. Beta Decay Scheme II (from <http://atom.kaeri.re.kr>)

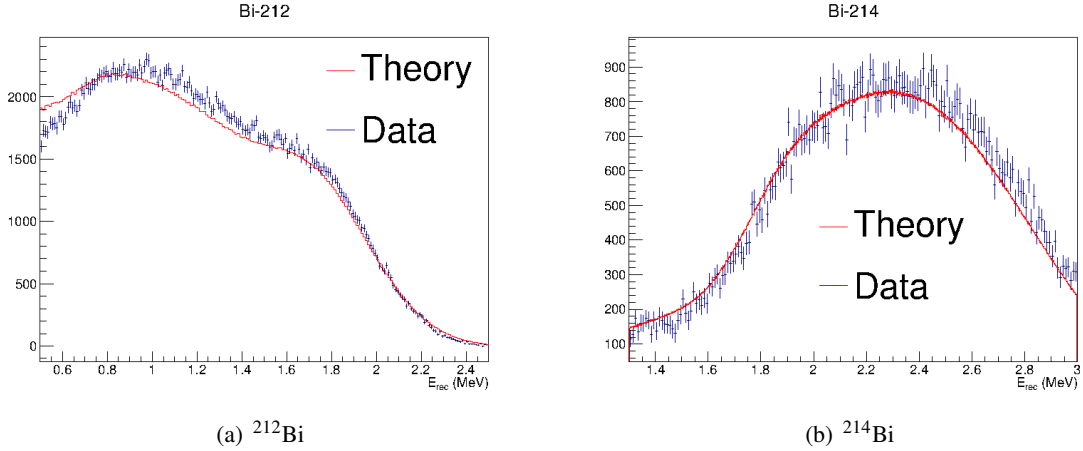


Figure 25. ^{212}Bi and ^{214}Bi $\beta + \gamma$ decay spectra.

beta decays are 1st forbidden non-unique decays. It is a big question to theorists how much the shape differs from the allowed decay calculation. For ^{214}Bi , due to the many closely packed energy levels of the daughter nucleus, the completeness of measurements to the beta-decay branches need investigation. For ^{208}Tl , the decay channels with large branching ratio are first non-unique forbidden decay (branching ratio 48.7%), first non-unique forbidden decay (branching ratio 21.80%), and 1st unique forbidden decay (branching ratio 24.50%). Therefore, it also suffers from the uncertainty in expected theoretical spectra. Therefore, the comparisons of data with expectation are only presented for the completeness of our discussion. The comparisons are shown in Fig. 25 and Fig. 26. For ^{208}Tl , there are additional backgrounds at low energy region, since it is extracted from a singles' spectrum.

^{12}B Spectrum ^{12}B is produced by the muon spallation inside the scintillator. ^{12}B beta decays

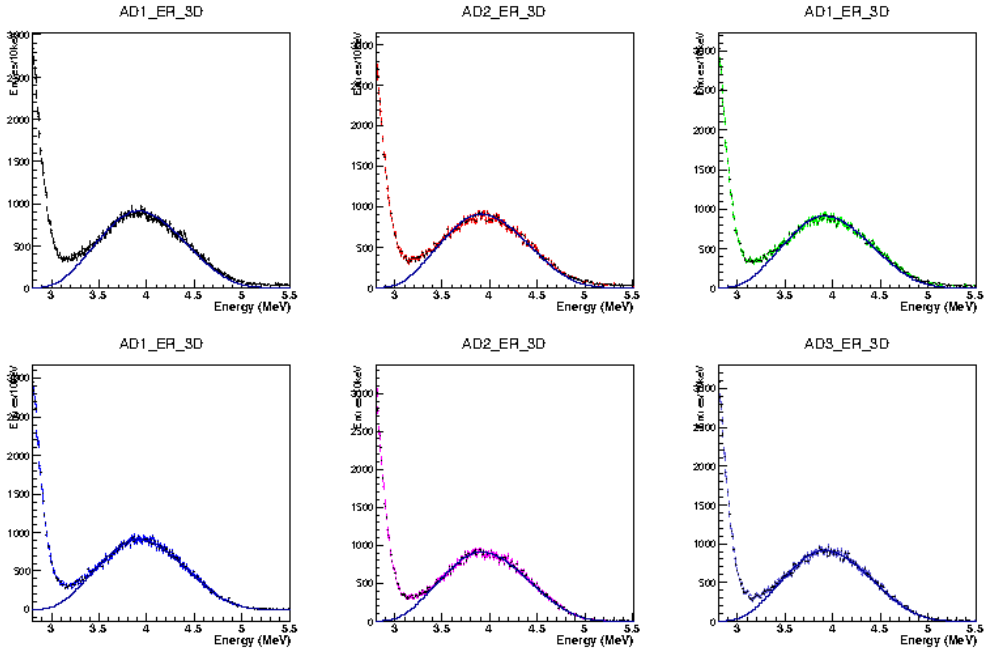


Figure 26. ^{208}Ti $\beta + \gamma$ decay spectra for all six ADs.

with half-life $\tau_{1/2} = 20.2$ ms. The end point of the β spectrum is 13.4 MeV. They are the most abundant spallation isotopes at high energies above 4 MeV. It is expected to have ~ 400 events per day per AD. They can be selected from the time correlation with preceding muon events as follows:

- $1\text{ms} < \Delta T_{B-\mu} < 100\text{ms}$ (signal window)
- $501\text{ms} < \Delta T_{B-\mu} < 600\text{ms}$ (background window for subtraction)
- $3\text{MeV} < E_B < 15\text{MeV}$ (only high energy part of the β spectrum)

The results are presented in Sec. 1.4.3. The selected data spectrum also contains backgrounds from ^{12}N , ^9Li , ^9C , ^8He , ^8Li , and ^8B . The contamination of these backgrounds are obtained by GEANT4 MC simulation [26] and updated in Ref. [27]. The results are summarized in Fig. 27.

The background spectra of ^{12}N , ^9Li , ^9C , ^8He , ^8Li , and ^8B are produced following the same procedure described in Sec. 1.6.3. More details can be found in Ref. [28]. Some of the essential information are summarized here:

- ^{12}N follows the beta+ decay. Both the 2.7% branching ratio channel and the 0.46% branching ratio channel always contain three alphas in the final state. In these cases, there would be no gammas in the final state.
- ^9C follows the beta+ decay. About 6% of the total branching ratio would contain one proton and two alphas in the final state. In these cases, the corresponding gammas would not appear in the final state.
- The ^9Li and ^8He follow the beta decay. The corresponding branching ratios in which there is no neutron in the final state are about 50% and 84% for ^9Li and ^8He , respectively.

Updated Table with Yue's B12 analysis

Isotope	BR	Half Life Time	1→100 ms	301→400 ms	501→600 ms	Counts from MC	Fractions
B12	100%	20.2 ms	0.93404	~0	~0	26580	24827
N12	100%	11 ms	0.93719	~0	~0	1015	951
C9	100%	126.5 ms	0.41640	0.08046	0.02689	380	148.4
He8	84%	119 ms	0.43564	0.07591	0.02368	63	21.76
Li9	50.5%	178.3 ms	0.32825	0.09913	0.04556	732	105.78
Li8	100%	838 ms	0.07850	0.06126	0.05195	5513	146.42
B8	100%	770 ms	0.08525	0.06506	0.05431	506	15.31

Figure 27. The contamination of these backgrounds are obtained by GEANT4 MC simulation [26] and updated in Ref. [27]. The last column shows the remaining background based on Yue's selection method.

- ${}^8\text{B}$ follows the beta+ decay.
- ${}^8\text{Li}$ follows the beta decay. 100% of the branching ratio will have two alphas in the final state.

The spectra of ${}^{12}\text{B}$ are very well known. The only complication is the decay of Hoyle State (branching ratio 1.5%). The Hoyle state [29] would mostly decay to three alphas instead of gamma [30].

In calculating the theoretical spectra for various nucleus, we took into account the deposited energy of proton and alphas using our nominal quenching model ($k_B = 6.4 \times 10^{-3} \text{ cm/MeV}$).

The comparison of the data with the theoretical spectra after implementing the nominal BCW energy non-linearity model is shown in Fig. 28. (log scale). The ratio of the data to the expected spectra is shown in Fig. 29. The nominal BCW model can very well describe the ${}^{12}\text{B}$ data. At high energy region ($E_{\text{rec}} > 13 \text{ MeV}$), there are some potential discrepancies between data and expectation, which could be reduced with a slightly larger ${}^{12}\text{N}$ contribution. Since the potential discrepancies are well above the IBD energy range and are limited by statistics, we did not investigate them.

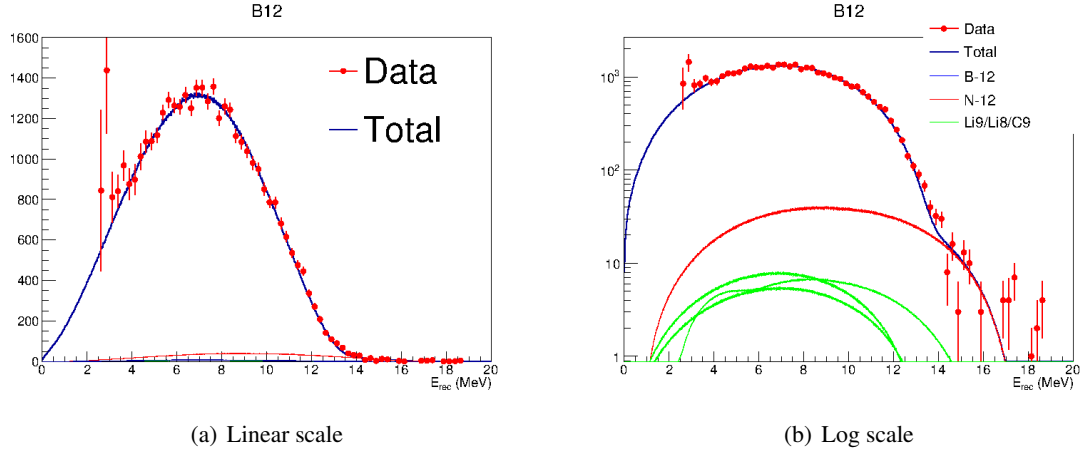
1.6.4 Validating Energy Model With IBD Spectrum

To be added.

1.7 Summary of Uncertainty Treatment

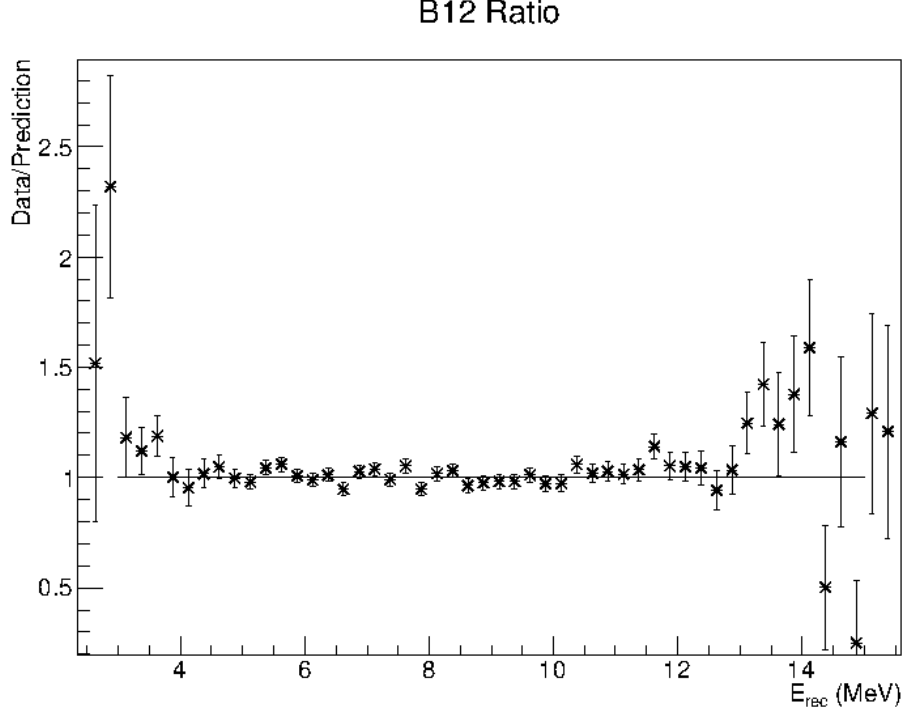
1.7.1 Statistical Uncertainty from Gamma Calibration Points

In the BCW model, gamma calibration data are used to constrain the effective electronics non-linearity. Therefore, the uncertainties of the gamma calibration points would result in uncertainties in the effective electronics non-linearity. Fig. 32 compares the this uncertainty with the uncertainty



(a) Linear scale

(b) Log scale

Figure 28. ^{12}B decay spectra (left: linear scale; right: log scale).**Figure 29.** The ratio of the data to the expected spectra.

due to k_B and k_C . It is clear that this uncertainty is much smaller than the uncertainty due to k_B and k_C .

1.7.2 Uncertainties due to k_B and k_C

As discussed in Sec. 1.6.1, there are ranges of possible Birks' constant k_B and Cerenkov contribution k_c . Therefore, we chose six models (listed in Table. 4) with typical combinations of k_B and k_c as the basis to evaluate the uncertainty of non-linearity. Here, the column of “electron radiation

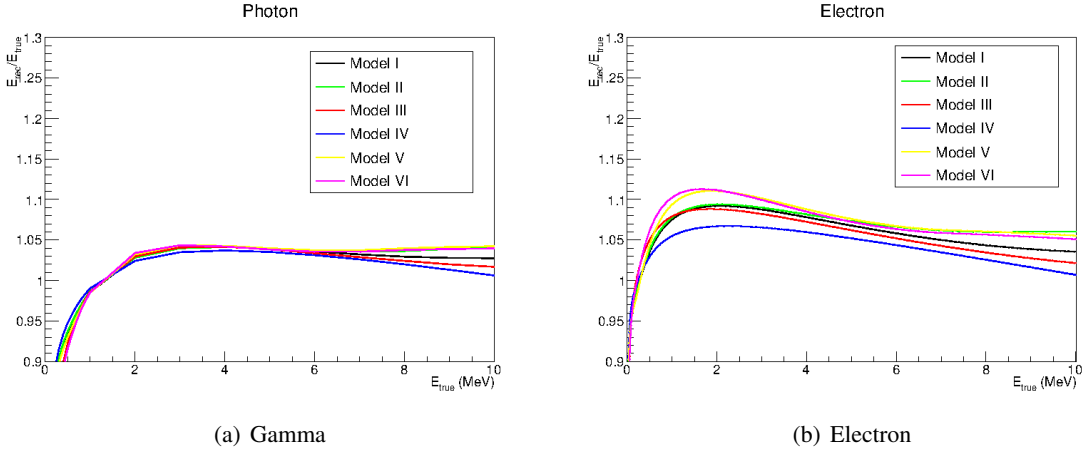


Figure 30. Comparison of six non-linearity models for gamma (left) and electron (right).

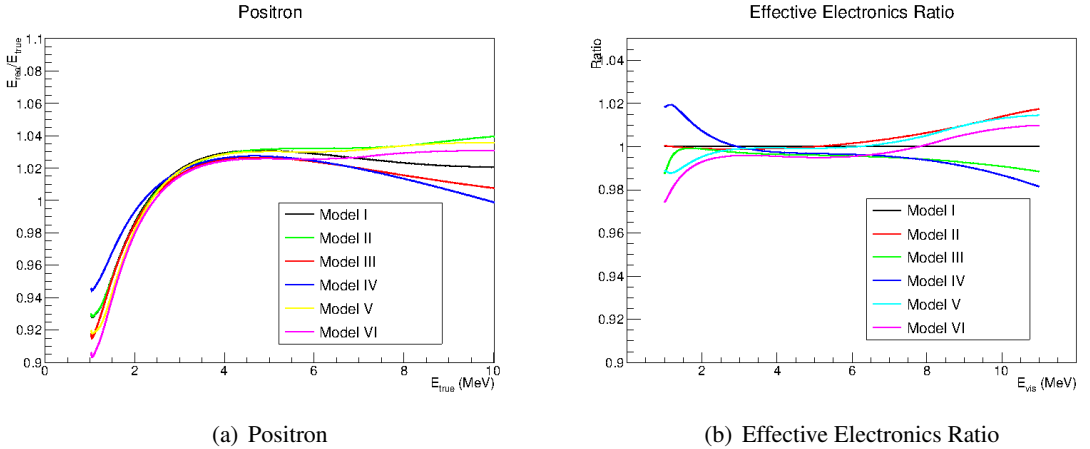


Figure 31. Comparison of six non-linearity models for positron (left). On the right panel, we show the comparison of effective electronics ratio.

“energy deposition” illustrates whether we use Eq. 1.5 (No) or Eq. 1.6 (Yes) in construct the quenching model. The column of “Electronics non-linearity” illustrate how we determine the electronics non-linearity. The results are summarized in Table. 4. The comparisons between data and models can be found in Sec. 1.8.4.

The comparison of these six models in terms of effective non-linearity (E_{rec}/E_{true}) for gamma and electron can be found in Fig. 30. The comparison of these six models in terms of effective non-linearity (E_{rec}/E_{true}) for positron is shown in Fig. 31. Furthermore, we define the ratio between effective positron non-linearity from each model and the effective positron non-linearity from the nominal model (Model I) as the “Effective Electronics Ratio” f_i :

$$f_i = \frac{\frac{E_{rec}}{E_{true}}|_{Model_i}}{\frac{E_{rec}}{E_{true}}|_{Nominal}}. \quad (1.11)$$

The right panel of Fig. 31 show the comparison f_i .

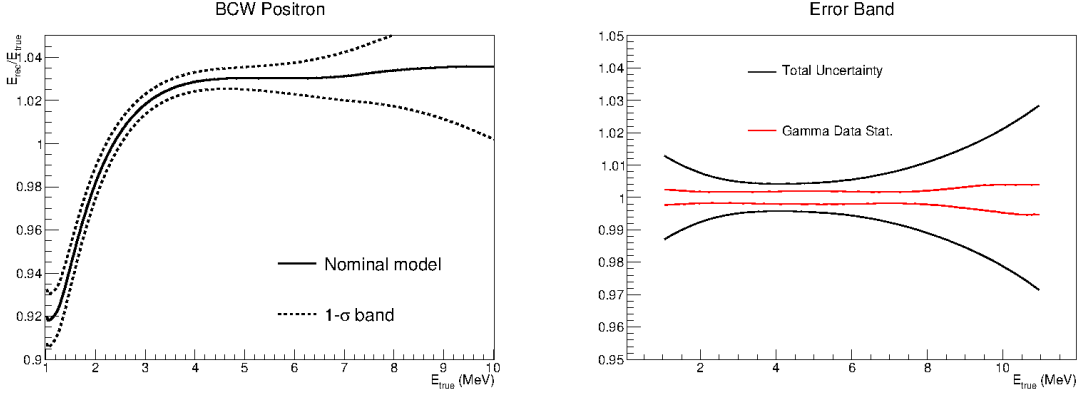


Figure 32. The nominal and $1-\sigma$ band of the positron non-linearity model (left). The right panel shows the $1-\sigma$ error band after normalizing the nominal model.

1.7.3 Uncertainties to be used in rate+shape fit

In order to implement the non-linearity models and their associated uncertainties into the fitter, we define the non-linearity model for positron as:

$$\frac{E_{rec}}{E_{true}} = \frac{E_{rec}}{E_{true}}|_{Nominal} \cdot \left(1 + \sum_{i=2}^{i=6} a_i \cdot (f_i - 1) \right). \quad (1.12)$$

One can easily check that when $a_i \equiv 0$, we recover the nominal model. Furthermore, if $a_2 = 1$, while all other $a_i \equiv 0$, we recover model II. The suggested penalty for a_i is:

$$Penalty = a_2^2 + a_3^2 + 4 \cdot a_4^2 + 4 \cdot a_5^2 + 4 \cdot a_6^2. \quad (1.13)$$

Here, we suggest an additional factor of 4 for model IV, V, and VI, since the agreement with data are not as good as that from model II and III. The resulting $1-\sigma$ band is shown in Fig. 32. The right panel of Fig. 32 shows the $1-\sigma$ error band after normalizing the nominal model. We also compare with the uncertainty associated with the uncertainty of gamma calibration points. Since the latter is quite small and we have been very conservative in quoting uncertainties due to k_B and k_C , we neglect it in our non-linearity model.

1.8 Final Remarks

1.8.1 Relative Energy Scale

The energy non-linearity model is important to set the correct absolute energy scale of our detectors. On the other hand, for the oscillation analysis, we are looking for an energy-dependent distortion between near and far detectors. The relative energy scale difference between ADs become even more important.

The relative energy difference between ADs was checked by various samples such as spallation neutron, α -decays, singles, etc. It was suggested in doc:8570 [31] that the relative energy scale uncertainty is 0.11%. In this analysis, we use a conservative estimate of 0.35%. This means each AD is allowed to have an independent $\pm 0.35\%$ stretch on the prompt spectrum.

1.8.2 Placed to be improved in the future

We will improve the treatment radiation energy loss for electron. Currently, we have adapted two extreme cases. Case I: the radiation energy loss is totally quenched. Case II: the total energy loss is assumed to only contain the collision energy loss. The truth will be somewhere in between. At the IBD energy, the truth is closer to the case I, which is our nominal model.

We have been assuming that the energy loss mechanism for electron and positron are the same. This assumption should be largely OK [11]. The small difference should be understood better.

We have been assuming that the Birks' constant is universal for all particles. This assumption is to be verified with future measurements.

We have been assuming that the electronics effect only depends on the total visible energy. In reality, it should also be sensitive to the position and timing pattern of the light. This effect is to be understood. Furthermore, it is desired to carry out an independent measurement of the electronics effect.

Uncertainty treatment of our model can be further improved once our knowledge of the electronics non-linearity is improved with future measurement.

1.8.3 Summary

In this note, we review the BCW energy non-linearity model. Our nominal model can satisfy all existing experimental constrains. We are ready to compare with the IBD spectrum.

1.8.4 Data Comparison

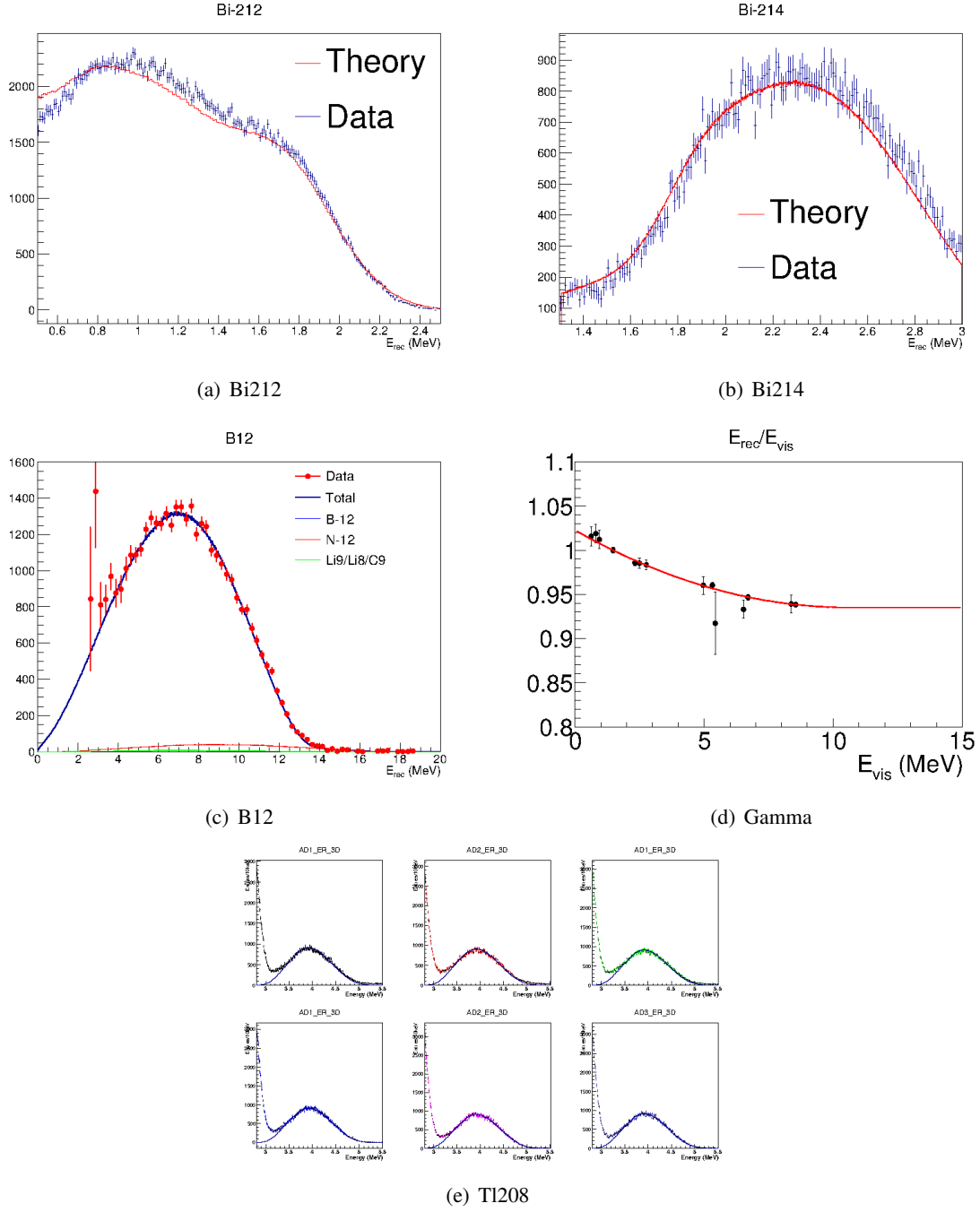


Figure 33. Model I.

1.9 Official Energy Model used in the Rate+Shape analysis

Besides the BCW energy model, IHEP [32] and LBNL [33] also independently developed two energy models. The Official energy model used in the rate+shape analysis adopts our concept of model weighting method. In addition to two BCW energy models, we added in two models from IHEP [32] and the LBNL [33] model. Therefore, in total, we have five energy models to construct

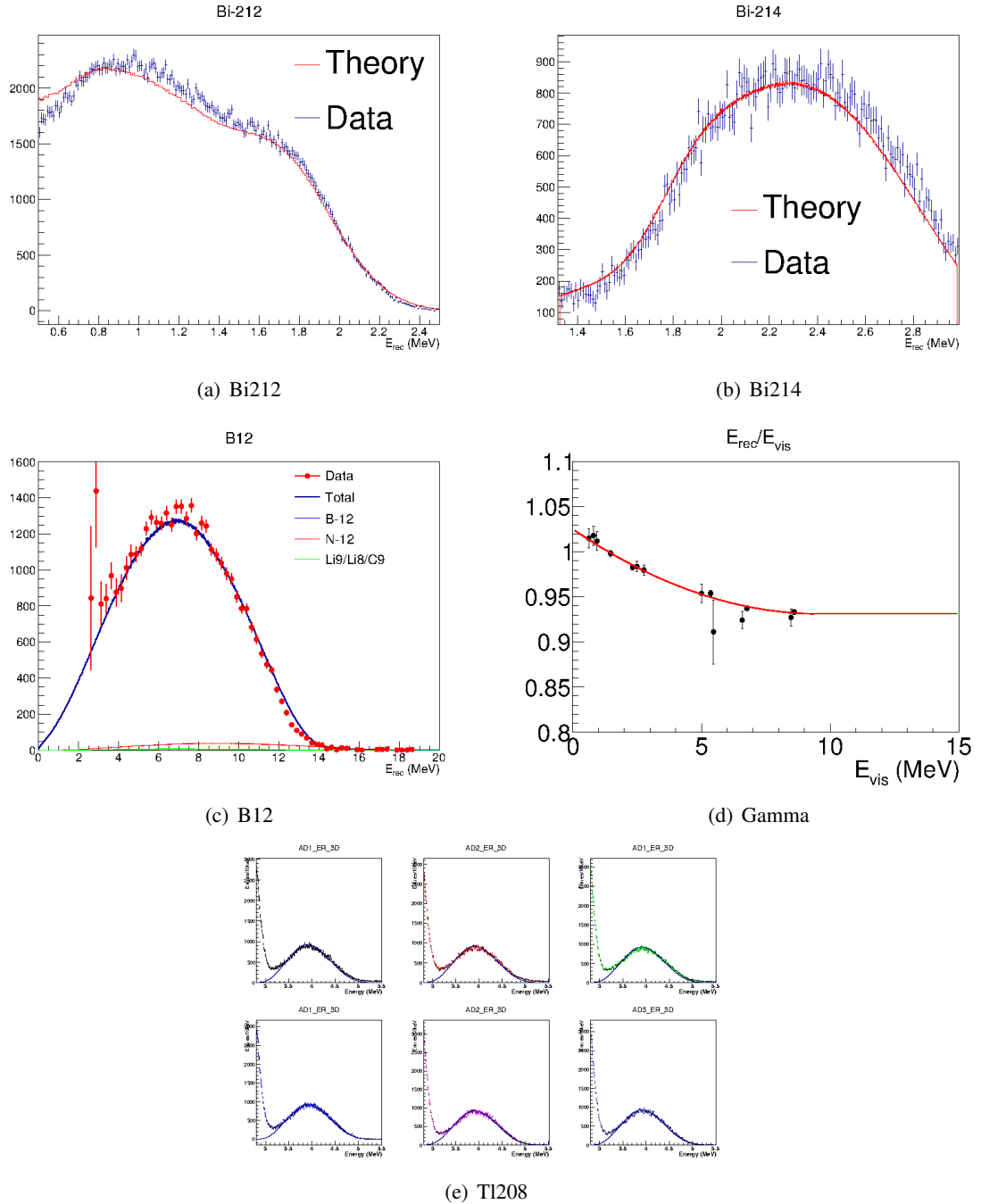


Figure 34. Model II.

the final uncertainty band for our energy model. The final combined uncertainty band is shown in Fig. 39. The uncertainty band can cover all the models which can give good description of our calibration data. The linear combination of the five models can also largely reproduce all the available models.

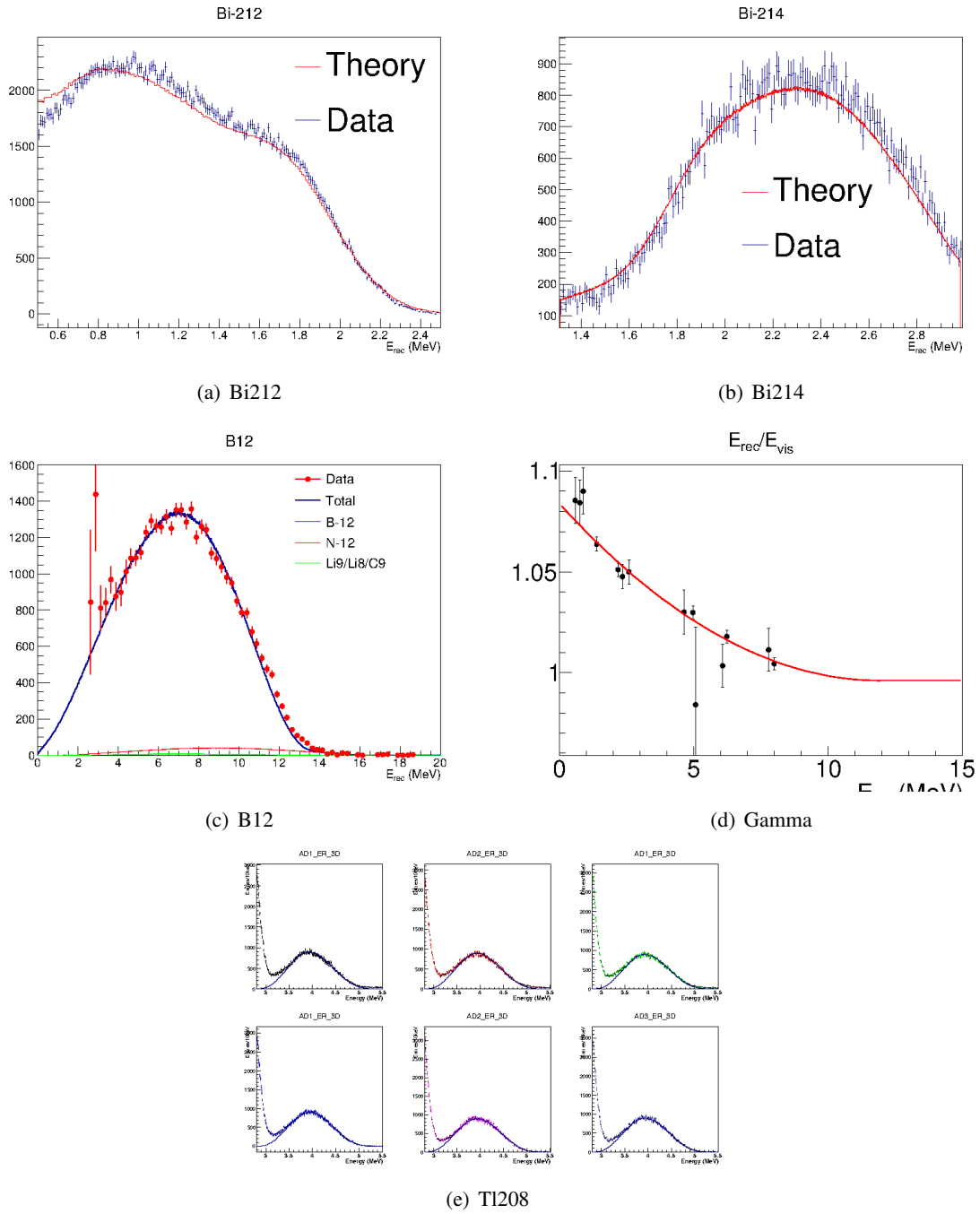


Figure 35. Model III.

Table 4. Summary of six models in evaluating the uncertainty of the non-linearity model. See text for more explanations.

Model No	k_B (10^{-3} cm/MeV)	Cerenkov contribution at 1 MeV	Electron radiation energy deposition	Daya Bay Gamma calibration	Daya Bay B12	Daya Bay Bi/Tl	Daya Bay alpha
I	6.4	8.3%	Yes	Good	Good	Acceptable	Acceptable
II	6.4	8.3%	No	Good	Reasonable	Acceptable	Acceptable
III	13.8	4.6%	Yes	Good	Reasonable	Acceptable	Bad
IV	6.4	4.5%	Yes	Reasonable	Not good	Acceptable	Acceptable
V	6.4	11.1%	Yes	Reasonable	Reasonable	Acceptable	Acceptable
VI	13.8	8.3%	Yes	Reasonable	Reasonable	Acceptable	Bad

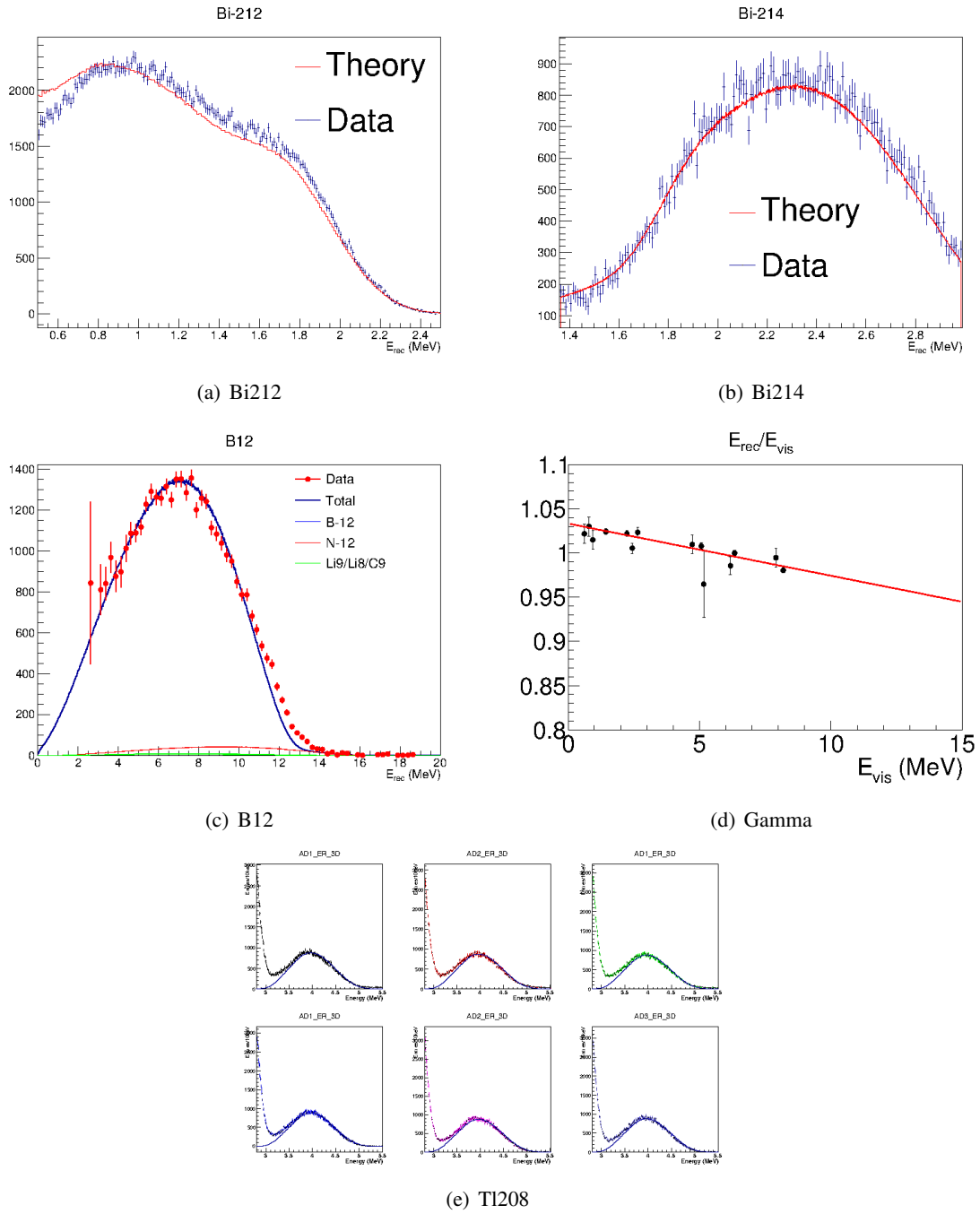


Figure 36. Model IV.

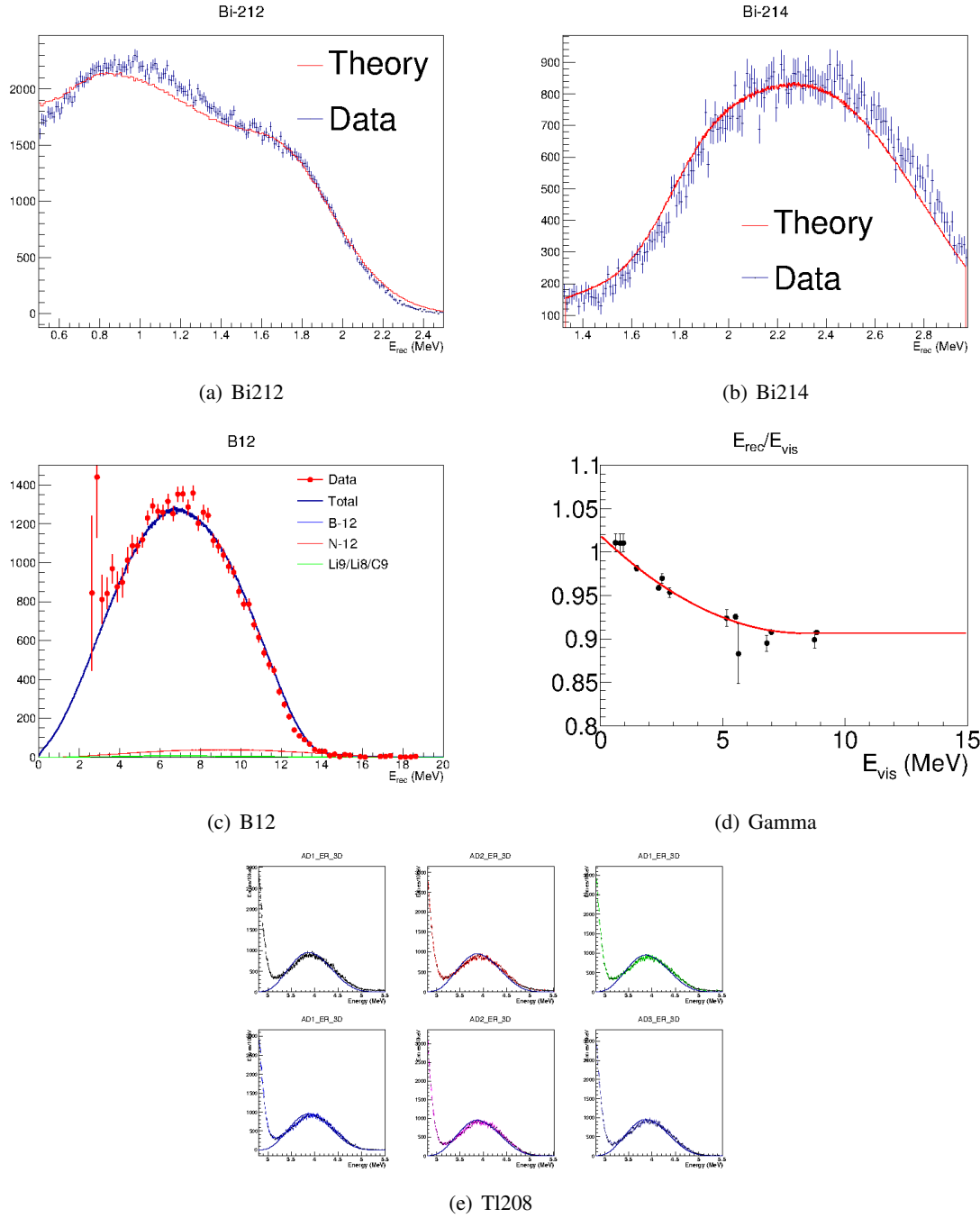


Figure 37. Model V.

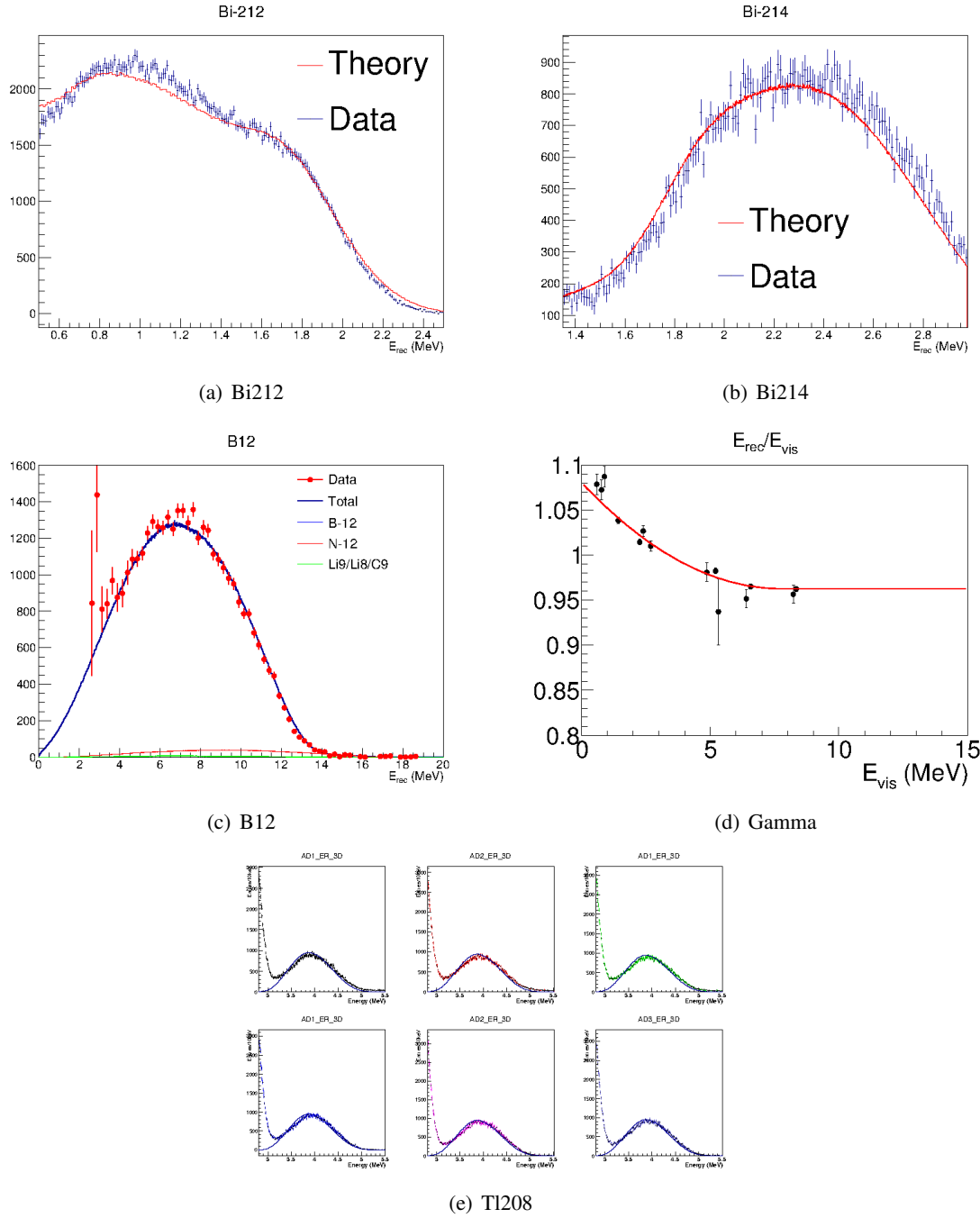


Figure 38. Model VI.

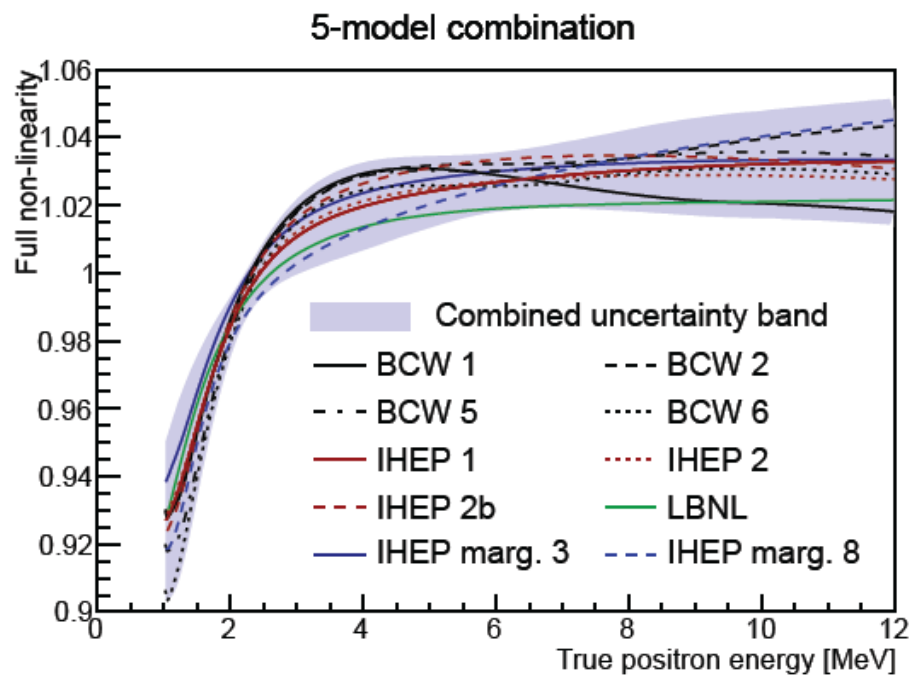


Figure 39. The final five-model-weighting energy model.

2. Anti-neutrino Candidates Selection

2.1 Run Selection and DAQ Live Time

In the presented θ_{13} rate & shape analysis we use the data from all stable 6 AD runs from Dec 24, 2011 to July 28, 2012, in which only runs that have all three experimental sites (Daya Bay / Ling Ao / Far) simultaneously running are used. The run numbers are from 21221 to 26694. Reconstructed data from *P12E* production are used. Data quality is carefully checked to remove ‘bad’ periods, which could be caused by high voltage failures, abnormal DAQ errors, unstable event rate, unusual noisy periods, etc. The details of the data quality check is documented in doc:8487 [34]. The full official good-run list is provided by the DQWG. Some runs are specially taken only to understand the properties and status of the detector, such as calibration runs and diagnostic runs. Data from these runs are not included in the oscillation analysis. The DAQ live time is then calculated by adding up the data taking time from all the clean periods, minus the short trigger disable gaps when the data flow rate is too high. The total DAQ live time is summarized in Table 7.

2.2 IBD Candidate Selection and Efficiency of Cuts

We use the same selection as described in the tech-note (doc:7621 [35]) of the February BCW θ_{13} rate analysis. We briefly summarize the selection rules below. Readers are encouraged to read doc:7621 [35] for details.

- **Prompt Energy Cut:** $0.7 \text{ MeV} < E_p < 12 \text{ MeV}$
- **Delayed Energy Cut:** $6 \text{ MeV} < E_d < 12 \text{ MeV}$
- **Time Correlation Cut:** $1 \mu\text{s} < \Delta T_{p-d} < 200 \mu\text{s}$
- **Flasher Cut:** The event must pass the flasher cut (doc:7434)
- **Muon Veto Cut:** The event must pass the muon veto cut
 - AD is vetoed $2 \mu\text{s}$ before any muons that are tagged by Water Pool⁵ or the same AD⁶.
 - AD is vetoed $600 \mu\text{s}$ after muons that are tagged by Water Pool.
 - AD is vetoed $1400 \mu\text{s}$ after muons that are tagged by the same AD.
 - AD is vetoed 0.4 seconds after shower muons⁷ in the same AD.
- **Multiplicity Cut:** The event must pass the decoupled multiplicity cut (*partial DMC*) cut
 - Only one prompt candidate within $200 \mu\text{s}$ before the delayed candidate
 - No other prompt candidate within $400 \mu\text{s}$ before the delayed candidate
 - Outside of the muon veto window, no delayed candidate within $200 \mu\text{s}$ after the delayed candidate

⁵*Water Pool Muon*: Number of *Inner Water Pool* hit PMTs > 12 in or number of *Outer Water Pool* hit PMTs > 12

⁶*AD Muon*: The total light yield in the AD > 3000 photoelectrons (PE)

⁷*AD Shower Muon*: The total light yield in the AD $> 3 \times 10^5$ photoelectrons (PE)

We summarize the efficiency of cuts in two tables. Again, readers are encouraged to read doc:7621 [35] for details in calculating the efficiencies and uncertainties. Table 5 summarizes the common efficiencies that can apply to all ADs. For each efficiency, we quote an absolute uncertainty that is correlated among all ADs, and a relative uncertainty that is uncorrelated among ADs.

Table 5. Summary of efficiency of cuts common to all ADs

Description	Efficiency	Uncertainty	
		Correlated	Uncorrelated
Gd capture ratio	0.8383	0.0060	0.10%
Spill in	1.0503	0.0010	0.02%
Delayed energy cut	0.9224	0.0051	0.13%
Prompt energy cut	0.9981	0.0010	0.01%
Capture time cut	0.9857	0.0019	0.02%
Flasher cut	0.9991	0.0002	0.013%
Total	0.7983	0.94%	0.17%

Table 6 summarizes the efficiencies that are different among ADs. These efficiencies are also time dependent, and are calculated precisely on a run-by-run basis. The time dependences are plotted in Fig. 40 and Fig. 41. The mean efficiencies weighted by the live-time of each run are shown. The uncertainties on them are negligible.

Table 6. Summary of live-time weighted mean efficiency of cuts (different among ADs)

	Daya Bay		Ling Ao	Far		
	AD1	AD2	AD1	AD1	AD2	AD3
Muon veto cut	0.8153	0.8119	0.8473	0.9808	0.9802	0.9802
Multiplicity cut	0.9759	0.9762	0.9774	0.9764	0.9762	0.9760

Combining all, Table 7 summarizes the the total number of $\bar{\nu}_e$ candidates observed in each AD after the analysis cuts, together with the total efficiencies. Each AD at the far site sees about 14000 IBD events. The total statistical uncertainty combining the 3 ADs at the far site reaches below 0.5%.

Table 7. Summary of Anti-neutrino Candidates

	Daya Bay		Ling Ao	Far		
	AD1	AD2	AD1	AD1	AD2	AD3
DAQ live time [days]	191.001	191.001	189.645	189.779	189.779	189.779
Number of $\bar{\nu}_e$ candidates	101290	102519	92912	13964	13894	13731
Total efficiency of cuts	0.6351	0.6327	0.6611	0.7645	0.7639	0.7637

2.3 Distribution of Anti-neutrino Candidates

We show the detected $\bar{\nu}_e$ candidates (background not subtracted) per day as a function of time in

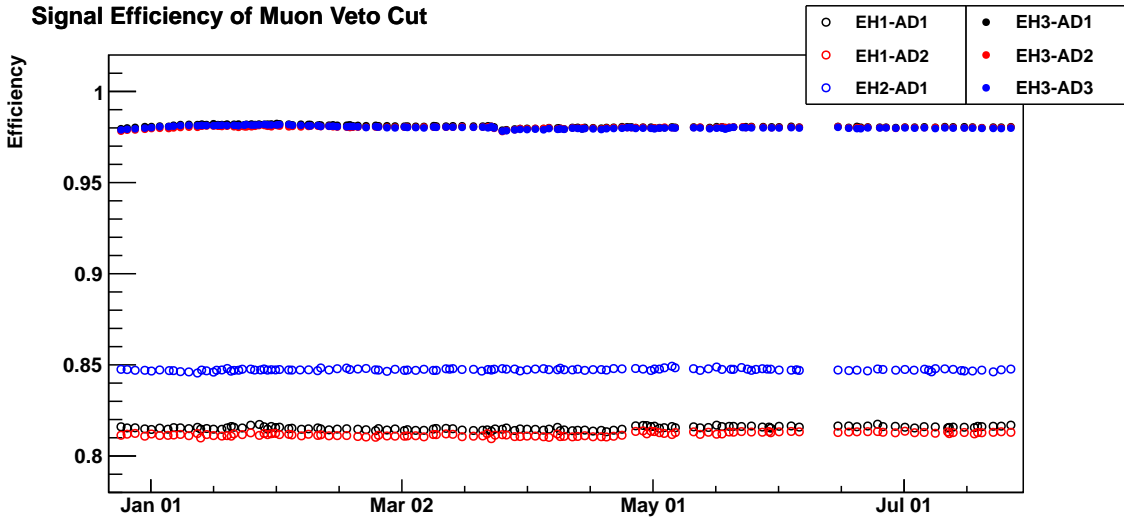


Figure 40. Signal efficiency of muon veto cut as a function of time. The rate is rather stable, indicating the stabilities of the water system.

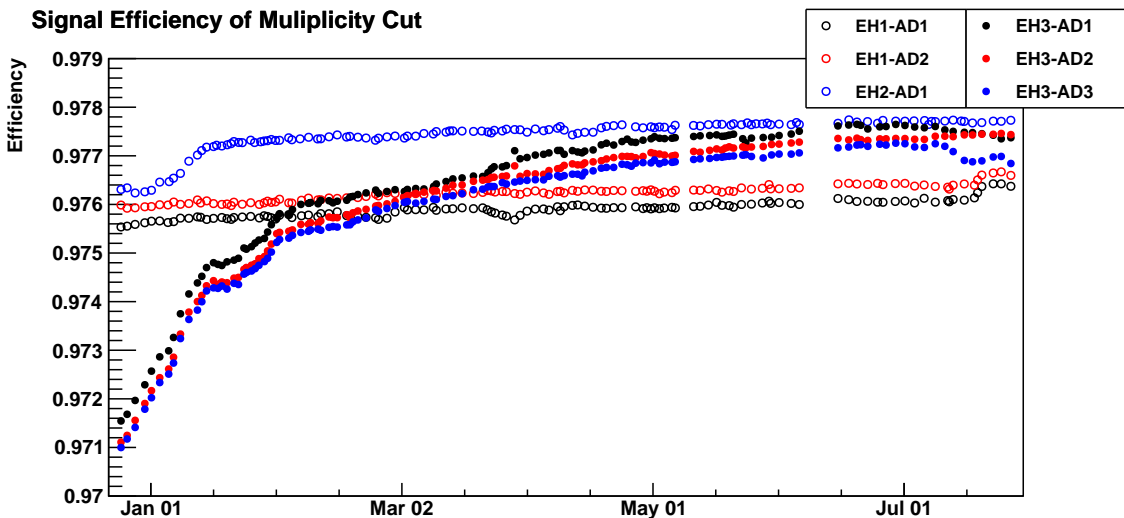


Figure 41. Signal efficiency of multiplicity cut as a function of time. The changes of efficiency is largely due to the changes of the R_p , the prompt-like singles rate in the AD.

Fig 42. The changes in the detected $\bar{\nu}_e$ rate tracks well with the activities of the Daya Bay and Ling Ao reactors.⁸

We further show some characteristic distributions of the $\bar{\nu}_e$ candidates in Figs. 43 - 49. All distributions look normal as expected.

⁸Only the reactor flux information from Dec 24, 2011 to May 11, 2012 is known. The reactor flux information for later periods are still blinded to the analyzers.

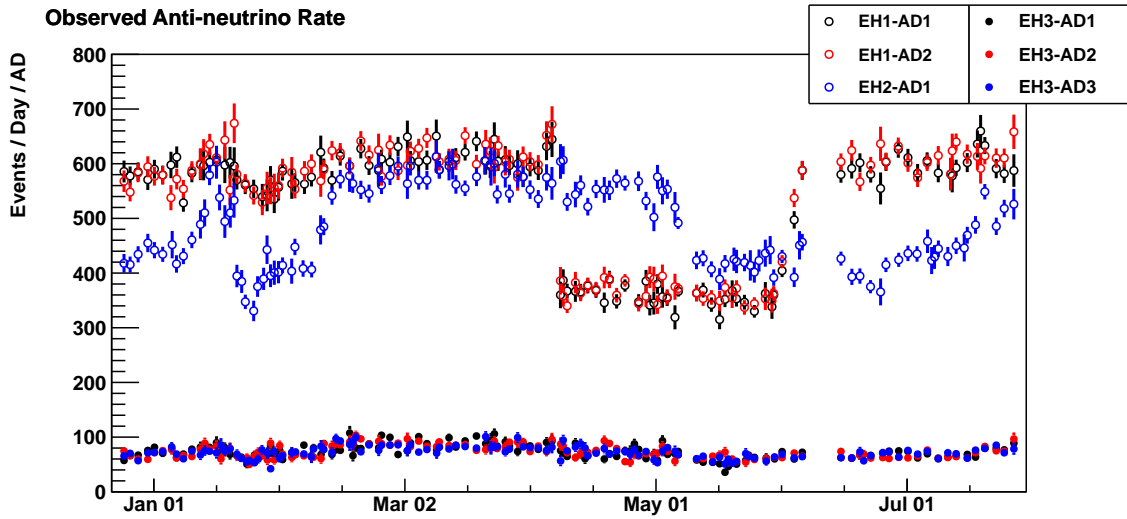


Figure 42. Detected $\bar{\nu}_e$ candidates per day as a function of time. Background is not subtracted from the candidates. Runs are combined such that each point has at least 8 hours.

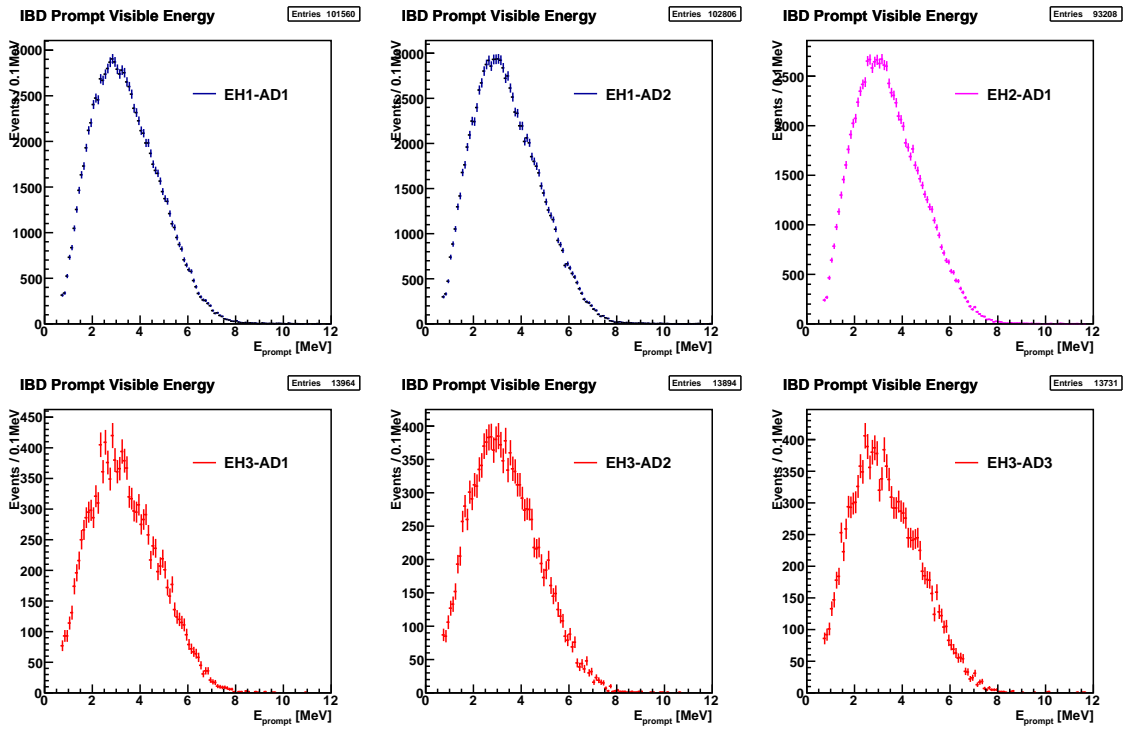


Figure 43. The prompt energy distribution of $\bar{\nu}_e$ candidates in each AD.

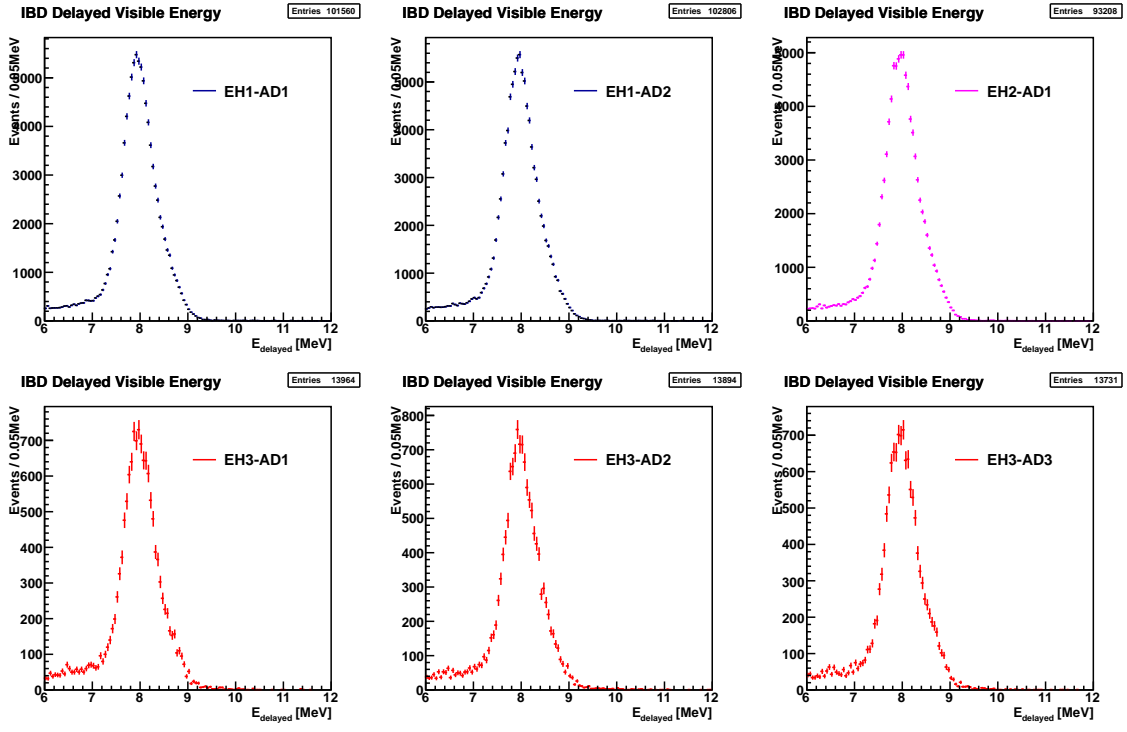


Figure 44. The delayed energy distribution of $\bar{\nu}_e$ candidates in each AD.

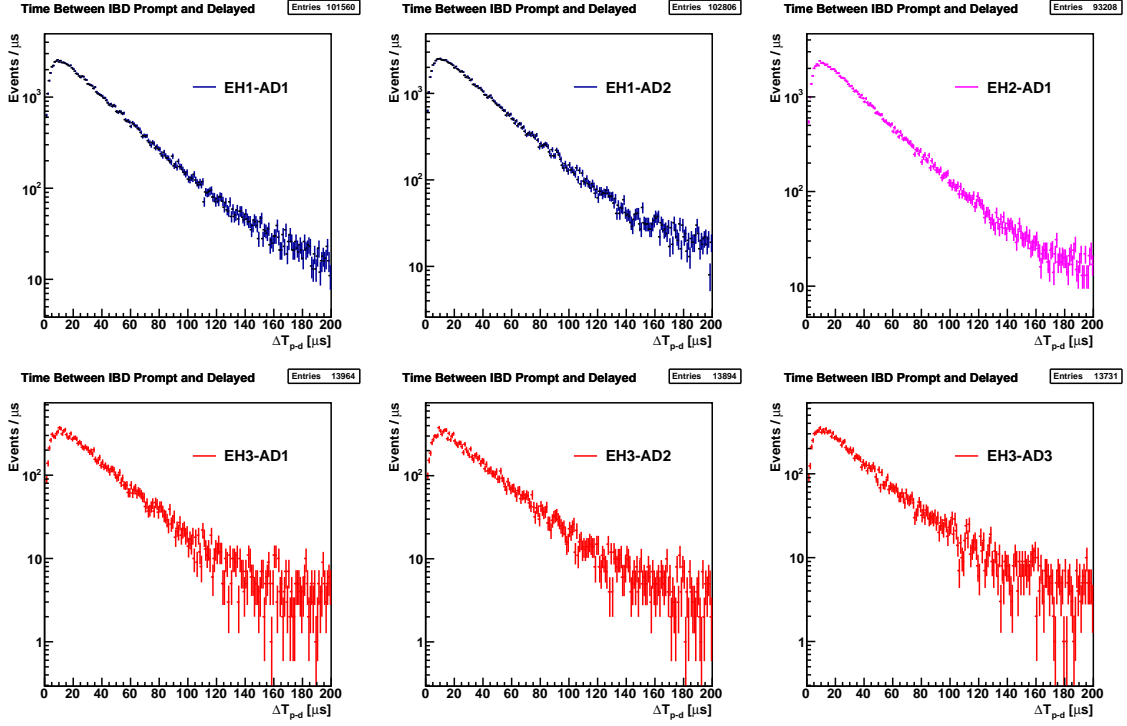


Figure 45. The neutron capture time distribution of $\bar{\nu}_e$ candidates in each AD.

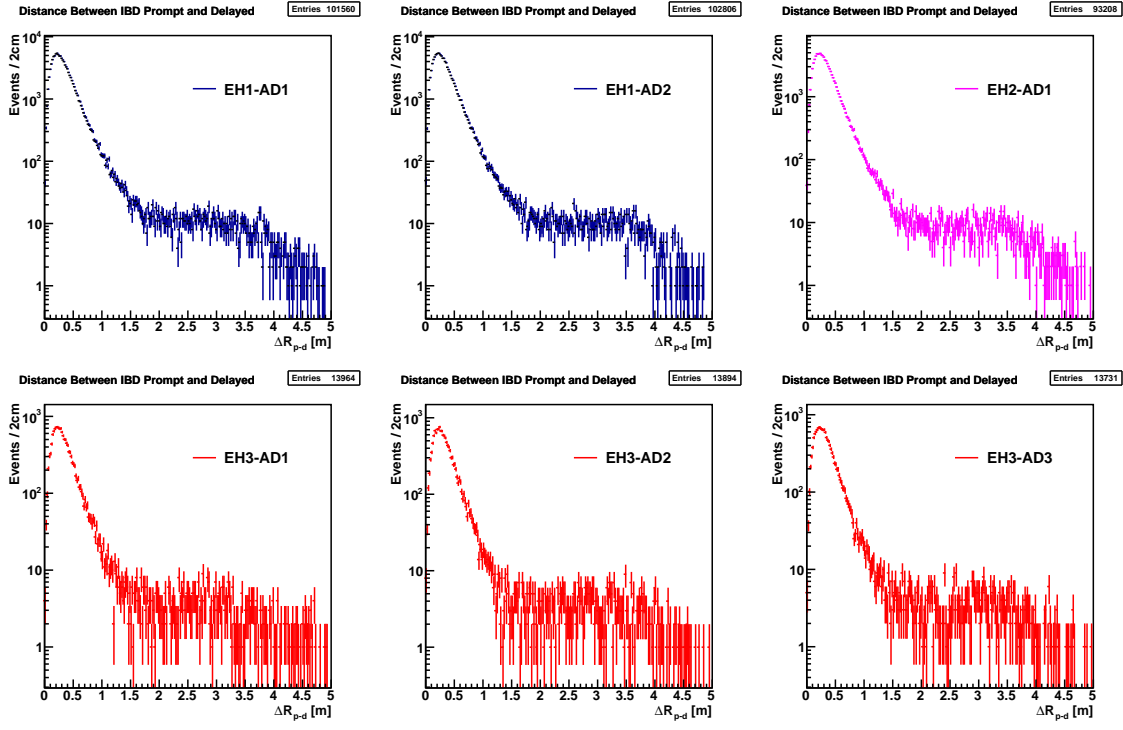


Figure 46. The distribution of distance between prompt and delayed event of the $\bar{\nu}_e$ candidates in each AD.

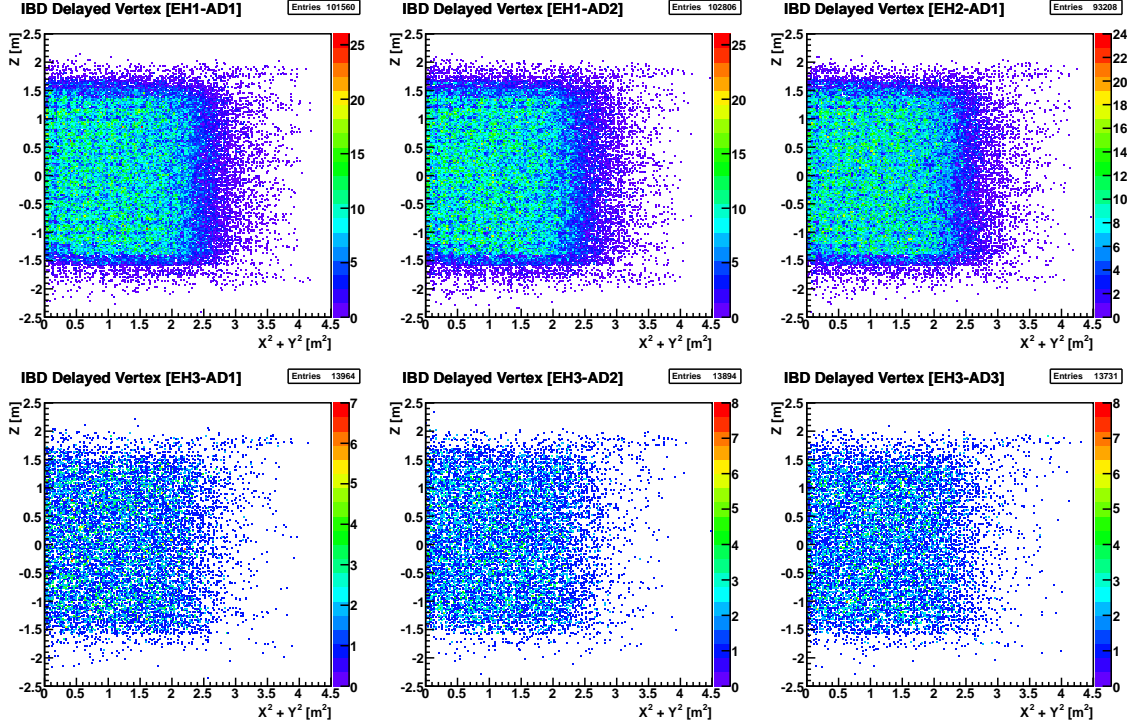


Figure 47. The vertex distribution of the delayed event of the $\bar{\nu}_e$ candidates in each AD.

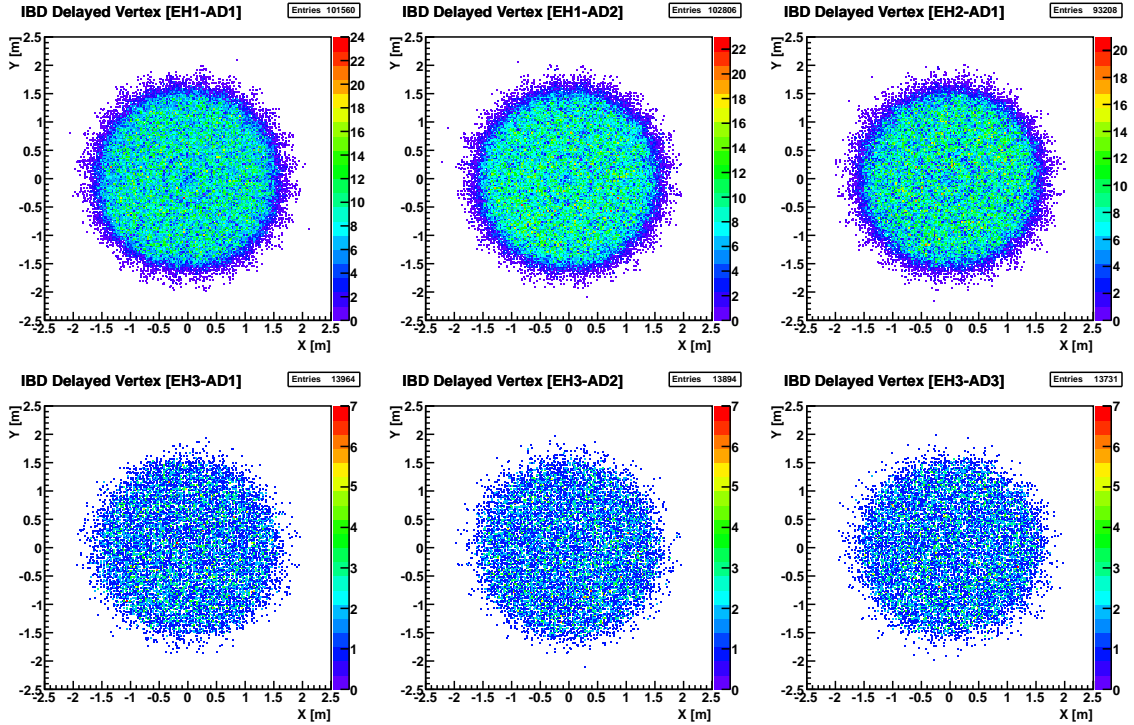


Figure 48. The vertex distribution of the delayed event of the $\bar{\nu}_e$ candidates in each AD.

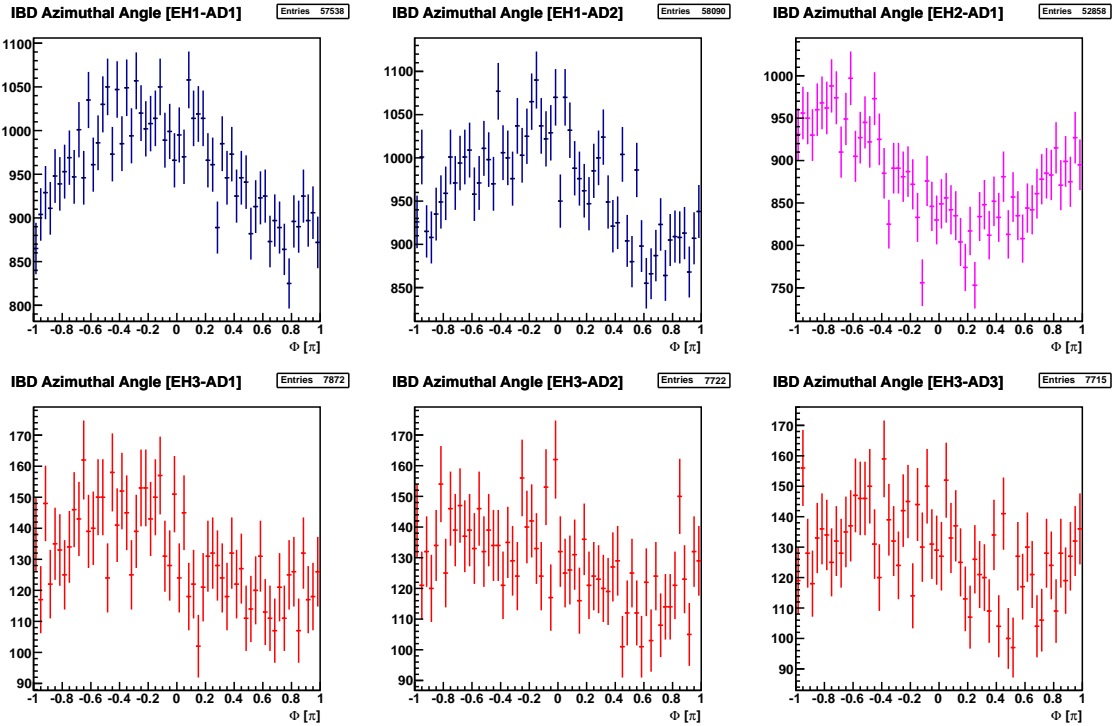


Figure 49. The distribution of the azimuthal angle of the vector from prompt to the delayed event of the $\bar{\nu}_e$ candidates in each AD. This direction approximates the incoming direction of the reactor neutrino.

3. Background Estimation

The general background treatment has been described in details in the doc:9140 [36] and the technote (doc:7621 [35]) of the February BCW θ_{13} rate analysis. Here we will only emphasize on the spectra shape and uncertainties of each background. The background events can be divided into two categories:

- *Accidental Background*: Two uncorrelated events ‘accidentally’ passing the analysis cuts and mimic an IBD pair.
- *Correlated Background*: True correlated events that fake the IBD interaction. The possible correlated backgrounds are:
 - ${}^9\text{Li}/{}^8\text{He}$ from muon spallation
 - Fast neutrons from muon spallation
 - Correlated signals from ${}^{241}\text{Am}{}^{13}\text{C}$ source
 - ${}^{13}\text{C}(\alpha, n){}^{16}\text{O}$ background

3.1 Accidental Background

The accidental background is caused by a ‘prompt-positron-like’ single event ($0.7 \text{ MeV} < E_p < 12 \text{ MeV}$) and a ‘delayed-neutron-like’ single event ($6 \text{ MeV} < E_d < 12 \text{ MeV}$) randomly happen close in time ($\Delta T_{p-d} < 200\mu\text{s}$) and fake an IBD pair. The accidental background is estimated by selecting isolated ‘singles’ events after applying muon veto cut and time isolation cut. The accidental background rate can then be calculated by:

$$R_{acc} = (1 - R_p \cdot 400\mu\text{s}) \cdot R_p \cdot 199\mu\text{s} \cdot R_d \quad (3.1)$$

where R_p and R_d are the ‘prompt-like’ singles rate and and the ‘delayed-like’ singles rate, which can be accurately calculated from the singles spectra on a run-by-run basis. On average, R_p is on the order of $\sim 70 \text{ Hz}$ and R_d is on the order of a thousand events per day. The origin of the ‘delay-neutron-like’ singles is investigated in doc:7043 [37]. The accidental rate as a function of time in each AD is shown in Fig. 50. The variation of the accidental rate is mainly due to the changes of R_p with time, which is possibly correlated with Rn activities in the water.

The estimated total number of accidental background events is summarized in Table. 8. By varying the time window of the time isolation cut, we estimated a systematic uncertainty of 0.2% on calculating the accidental rate. The energy spectra of the accidentals in each AD can be accurately determined by accumulating the ‘singles’ E_p spectra in all data-taken periods. The spectra are shown in Fig. 51. The uncertainty on the spectra shape is negligible and is ignored in the presented shape analysis.

3.2 ${}^9\text{Li}/{}^8\text{He}$ Background

${}^9\text{Li}$ ($\tau_{1/2} = 178.3 \text{ ms}$, $Q = 13.6 \text{ MeV}$) and ${}^8\text{He}$ ($\tau_{1/2} = 118.5 \text{ ms}$, $Q = 10.7 \text{ MeV}$) are long-lived isotope produced by cosmic muons entering AD. Their beta-decay daughters are neutron unstable which further decays to emit a neutron. This gives a correlated beta-neutron signal and fake the

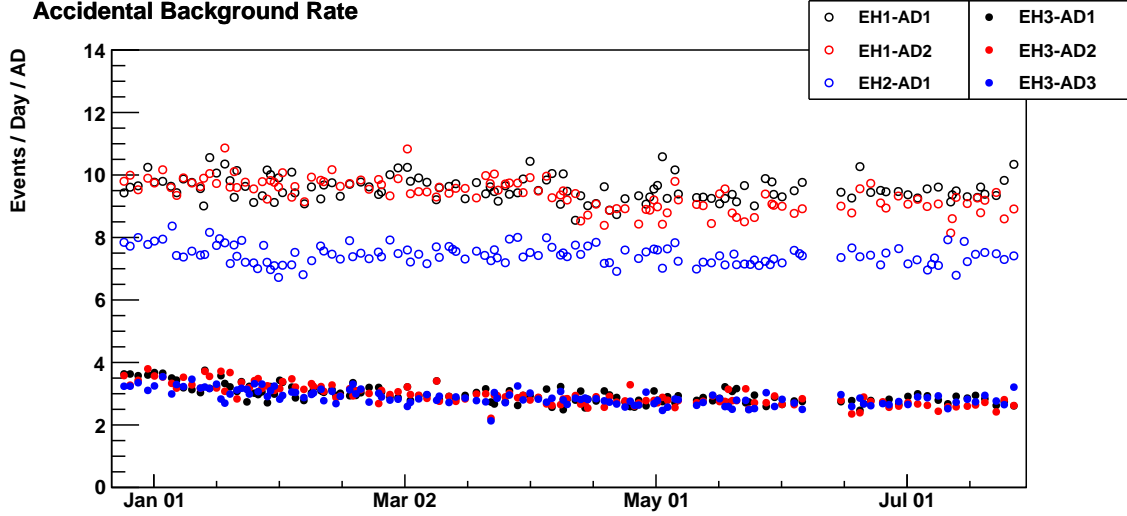


Figure 50. Accidental Rate as a Function of Time

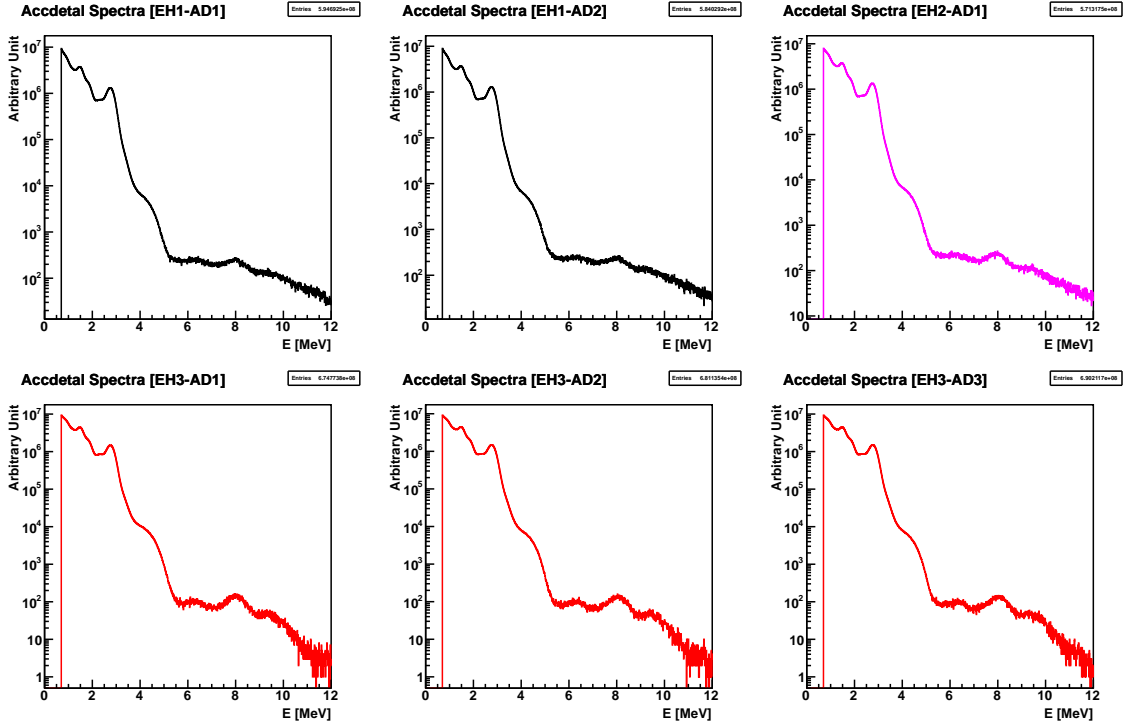


Figure 51. Energy spectra of accidental background in all six ADs.

IBD events. The shower muon veto is designed to remove most of the ${}^9\text{Li}/{}^8\text{He}$ background. The remaining background is estimated by selecting muon tagged ${}^9\text{Li}/{}^8\text{He}$ events and fit the time to muon distribution:

$$f(t) = \sum_i N_i \cdot (\lambda_\mu + \lambda_i) e^{-(\lambda_\mu + \lambda_i)t} + N_r \cdot \lambda_\mu e^{-\lambda_\mu t} \quad (3.2)$$

where λ_μ is the ‘muon’ (after analysis cuts) rate in study. N_i is the number of spallation isotope i produced by the muons and λ_i is the decay time of the isotope i . To have a reasonable fit, the muon rate need to be reduced to significantly lower than than the isotope decay rate. This is not a problem for high energy muons (e.g. shower muons $E_\mu > \sim 1.7$ GeV), but becomes challenging for low energy muons. Technique such as requiring a neutron produced by the muon is explored and efficiency is estimated. By adding up the ${}^9\text{Li}/{}^8\text{He}$ production rate from muons of different energy, the estimated total number of ${}^9\text{Li}/{}^8\text{He}$ background events is summarized in Table. 8. The uncertainty is dominated by the statistics collected.

The ${}^9\text{Li}$ and ${}^8\text{He}$ energy spectra is calculated according to doc:8772 [38] and doc:8860 [39]. The spectra uncertainty is implemented by taken into account the following effects:

- The ratio $r = {}^9\text{Li}/({}^8\text{He} + {}^9\text{Li})$ is treated as a nuisance parameter. $r = 95\% + -5\%$.
- We calculate the ${}^9\text{Li}/{}^8\text{He}$ spectrum in Erec (apply quenching model for all particles, and then electronics non-linearity). Assuming that the Erec spectrum is coming from beta only, we can apply the inverse of the electron nonlinearity model to obtain an effective beta decay spectrum (Etrue). In the fitter, we apply the energy nonlinearity model on this effective beta decay spectrum to calculate the spectrum on Erec.
- The shape uncertainties for the quenching of neutron and α are calculated with two sets of kb values (6.4 and 13.8). One nuisance parameter is implemented to control the change from one spectrum to another spectrum.
- ${}^9\text{Li}/{}^8\text{He}$ is largely a beta decay spectrum. the electron energy model is well constrained by the ${}^{12}\text{B}$ spectrum. Therefore we can directly use the state-of-art electron energy model, which decouples form the positron energy model in the fitter. In practice, we used Gaosong’s covariance matrix (doc:9024 [40]) with 4 nuisance parameters.

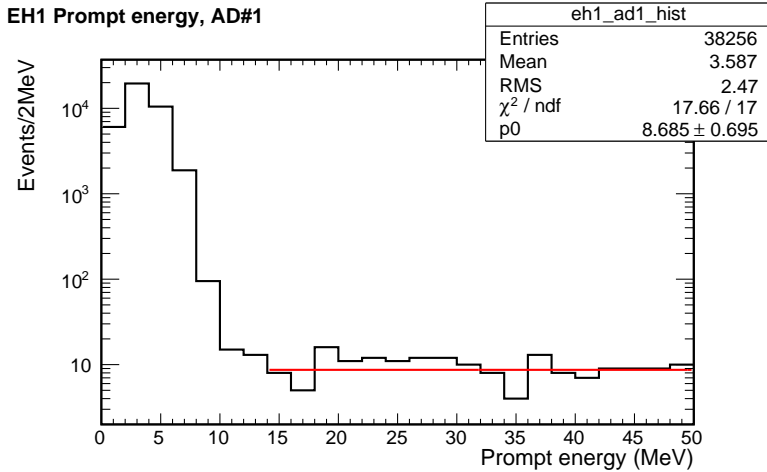
3.3 Fast neutron Background

Fast neutrons produced by muons could enter AD and give coincidence events that mimic the IBD events, where the prompt event comes from proton recoil by the neutron. If the parent muon is not detected by water pool or the AD, either from inefficiency of the veto system, or from muons outside of the veto system, the fast neutron will escape the muon veto cut and contribute to the $\bar{\nu}_e$ background.

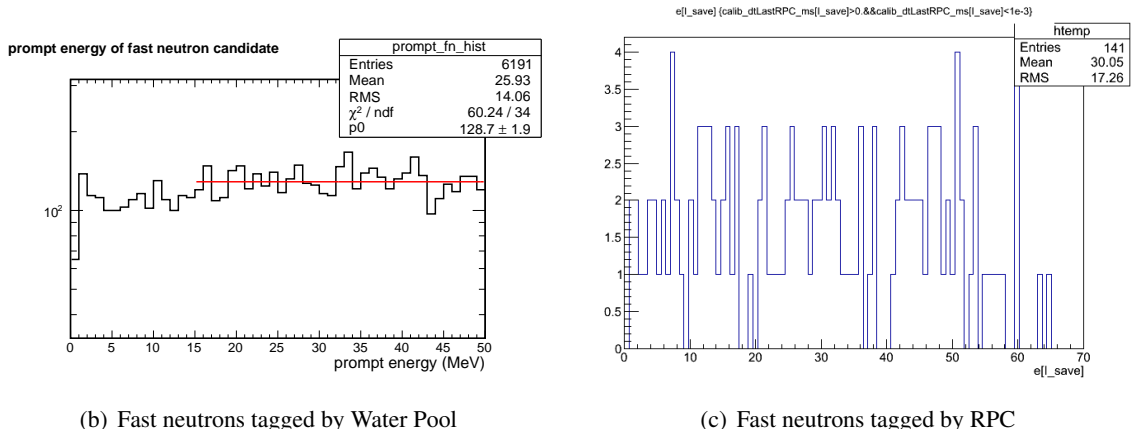
The fast neutron background is studied by looking for IBD candidates above 8.5 MeV where the reactor neutron spectra dropped to a negligible level, as well as the IBD-like events in coincidence with muons tagged by water pool or RPC. All three methods showed a consistently flat prompt energy spectra (Fig. 52). The total number of the fast neutron background in (0.7MeV, 12MeV) is extrapolated from high energy IBD candidates assuming a flat energy spectra. The result is summarized in Table. 8. 50% systematic uncertainty is assigned to account for the possible deviation from a flat spectra shape.

3.4 Correlated ${}^{241}\text{Am}{}^{13}\text{C}$ Background

The ${}^{241}\text{Am}{}^{13}\text{C}$ sources (0.5 Hz neutron rate) parking on top of the ADs can cause correlated background. It is mainly caused by two correlated high energy gammas from one ${}^{241}\text{Am}{}^{13}\text{C}$ neutron.



(a) Fast neutrons tagged by AD



(b) Fast neutrons tagged by Water Pool

(c) Fast neutrons tagged by RPC

Figure 52. Prompt energy spectrum of fast neutron tagged by (a) AD; (b) Water Pool; (c) RPC.

The prompt signal comes from neutron inelastic scattering on stainless steel, and the delayed signal comes from the neutron capture on stainless steel. The two gammas have a small probability of entering the AD together causing correlated events.

A simulation has been performed (doc:6779 [41]) to study this background. Special calibration runs have been taken to compare with the simulation. In the special runs, a strong $^{241}\text{Am}^{13}\text{C}$ source was placed on top of the SS lid between ACU-A and ACU-B, for a total of 10 days. From both simulation and the special calibration, the yield ratio of correlated over uncorrelated AmC background is estimated. The measured rate of uncorrelated AmC background is shown in doc:8979 [42]. We then estimated the correlated $^{241}\text{Am}^{13}\text{C}$ background rate to be 0.26 ± 0.12 events/day/AD for all ADs. The 45% relative uncertainty on the background is conservatively estimated from the comparison between data and simulation [42].

The energy spectra of the correlated $^{241}\text{Am}^{13}\text{C}$ background is from the analysis of the special calibration run, and shown in Fig. 53. The spectra agree with the Monte Carlo simulation within statistics. The uncertainty of the $^{241}\text{Am}^{13}\text{C}$ shape is constrained by a exponential fit with

uncertainty of 15% on the fitting parameter as recommended in the doc:8979 [42].

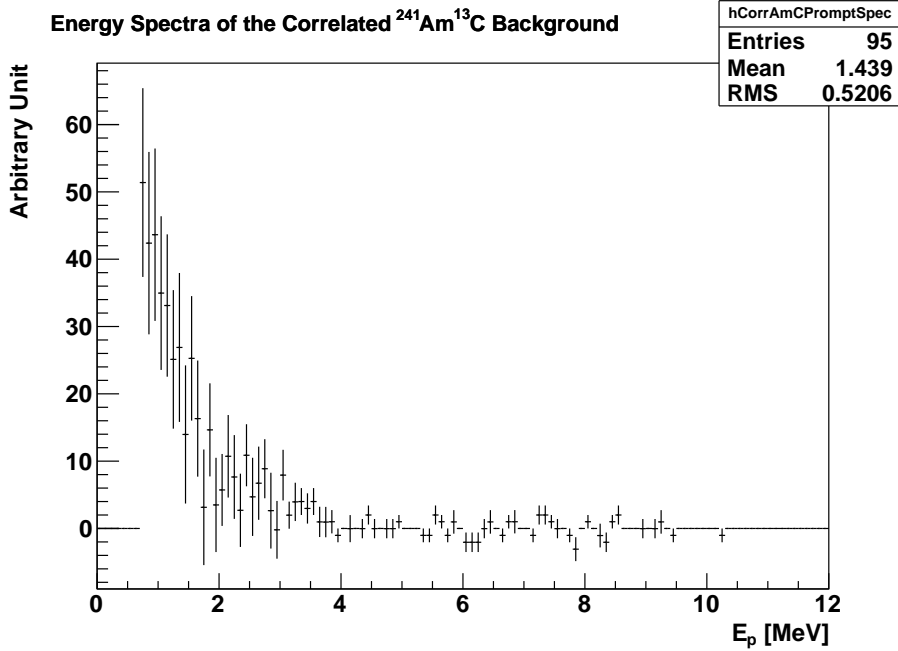


Figure 53. Energy spectra of the correlated $^{241}\text{Am}^{13}\text{C}$ background.

3.5 $^{13}\text{C}(\alpha, \text{n})^{16}\text{O}$ Background

From the measured alpha rate combined with the $^{13}\text{C}(\alpha, \text{n})^{16}\text{O}$ cross sections, the (α, n) background is estimated in doc:7509 [43] to be 0.007% in AD1/2/3 and 0.05% in AD 4/5/6 compared to the IBD rate, much smaller compared with other backgrounds. The rate in each AD is summarized in Table. 8

The energy spectra of the $^{13}\text{C}(\alpha, \text{n})^{16}\text{O}$ background is calculated in doc:8716 [44], and shown in Fig. 54. We don't assign uncertainty to the shape of the spectra.

3.6 Summary of Background Estimation

Table. 8 summarizes the total number of expected backgrounds in the data set, as well as the total number of candidates including backgrounds. Table. 9 summarizes the same information in terms of rate (events/day), where the neutrino rate has the estimated background subtracted. The rates have been corrected (divided) by the detector-dependent muon cut efficiency and multiplicity cut efficiency, for comparison of different AD's.

The total number of background events is dominated by the accidentals, but the uncertainty on the backgrounds is dominated by $^9\text{Li}/^8\text{He}8$, fast neutron and correlated $^{241}\text{Am}^{13}\text{C}$ backgrounds.

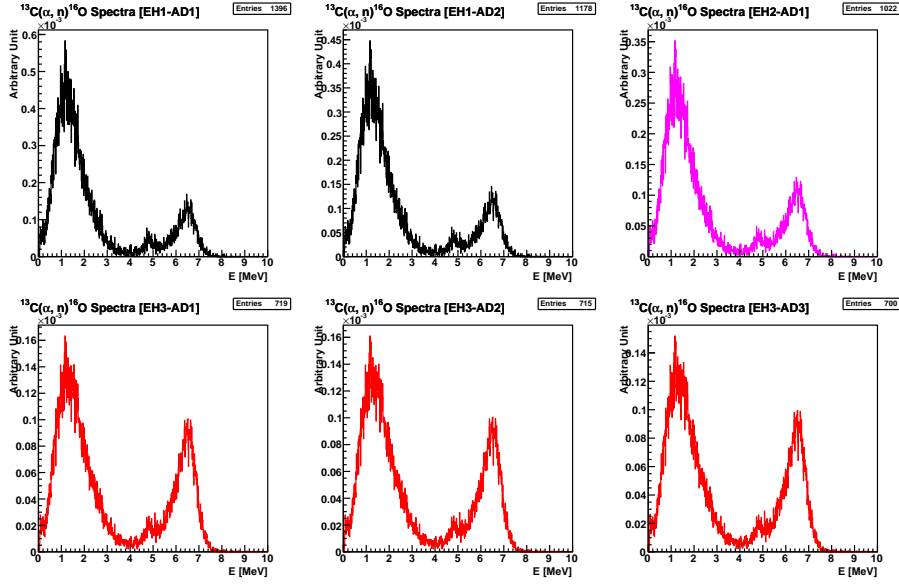


Figure 54. Energy spectra of the $^{13}\text{C}(\alpha, \text{n})^{16}\text{O}$ background.

Table 8. Summary of observed signals and estimated backgrounds [events]

	Daya Bay		Ling Ao	Far		
	AD1	AD2	AD1	AD1	AD2	AD3
DAQ live time [days]	191.00	191.00	189.65	189.78	189.78	189.78
$\bar{\nu}_e$ candidate [events]	101290	102519	92912	13964	13894	13731
Accidentals [events]	1449.8	1416.6	1168.0	538.6	530.8	521.4
$^9\text{Li}/^8\text{He}8$ [events]	364.7	363.4	188.5	40.0	39.9	39.9
Fast Neutron [events]	139.8	139.3	97.4	7.3	7.3	7.3
Correlated $^{241}\text{Am}^{13}\text{C}$ [events]	39.5	39.4	40.8.4	47.3	47.2	47.2
$^{13}\text{C}(\alpha, \text{n})^{16}\text{O}$ [events]	12.2	10.6	7.9	7.3	7.3	7.3
Total Expected B.G. [events]	2006.0	1969.2	1502.6	640.3	632.5	623.0
B.G. Uncertainty [events]	149.5	149.0	112.0	25.0	25.0	25.0

Table 9. Summary of observed signals and estimated backgrounds [events/day]

	Daya Bay		Ling Ao	Far		
	AD1	AD2	AD1	AD1	AD2	AD3
$\bar{\nu}_e$ [/day]	653.297	664.146	581.973	73.311	73.031	72.200
Accidentals [/day]	9.5397	9.3570	7.4363	2.9633	2.9232	2.8718
$^9\text{Li}/^8\text{He}8$ [/day]	2.4	2.4	1.2	0.22	0.22	0.22
Fast Neutron [/day]	0.92	0.92	0.62	0.04	0.04	0.04
Correlated $^{241}\text{Am}^{13}\text{C}$ [/day]	0.26	0.26	0.26	0.26	0.26	0.26
$^{13}\text{C}(\alpha, \text{n})^{16}\text{O}$ [/day]	0.08	0.07	0.05	0.04	0.04	0.04

4. Reactor flux and systematic uncertainties

The reactor flux uncertainties are mostly cancelled out by the near-far detector design. However, there are still remained contributions to the final uncertainties in $\sin^2 2\theta_{13}$ and Δm^2 . To properly treat these uncertainties, a detailed reactor flux and its uncertainty analysis is needed.

Daya Bay has 6 reactor cores. Together with the uncertainties presented in the fission isotope spectra, there are more than 140 systematic uncertainties, which is a considerable burden to the minimizer in the pull chi-square approach used in past Daya Bay analysis. It not only slows down the minimizer but only makes it less reliable. To resolve this, we propose a combination of “pull” and “covariance matrix” approach to treat the flux uncertainty correlations properly while keeping the numerical expenses low. The pull-covariance method has the advantages of both methods.

In this section, we first briefly describe the reactor flux models we considered and explain how we treat their uncertainties using a covariance matrix which can be used together with the conventional pull method.

4.1 Reactor antineutrino flux calculation

4.1.1 General principle

Reactor antineutrinos are the beta decay products of reactor fission isotopes. There are 4 dominant ones, ^{235}U , ^{238}U , ^{239}Pu , and ^{241}Pu . Total number of antineutrinos released by a reactor per unit time can be calculated in the following way,

$$\phi(E) = \frac{W_{th}}{\langle e_{fission} \rangle} \sum_{i=1}^4 f_i S_i(E), \quad (4.1)$$

where E is the antineutrino energy, W_{th} is the thermal power release of the reactor, $\langle e_{fission} \rangle = \sum_i f_i e_i$ is the fission fraction weighted fission energy release, f_i is the fission fraction of the 4 dominant fission isotopes, $S_i(E)$ is the fission isotope spectrum and i runs from 1 to 4 which represents ^{235}U , ^{238}U , ^{239}Pu , and ^{241}Pu . The Daya Bay reactors are all 2.895GW_{th} pressure water reactors (PWR) and it is well accepted that its thermal power can be measured to an accuracy of 0.5%. In the following subsections, we will discuss the quantities in Eq. 4.1 and their uncertainties. We will present the isotope spectra $S_i(E)$ in binned format and the bin size is 0.25MeV as chosen by the experts who have made the calculation.

4.1.2 Weekly average thermal power and fission fraction

Detailed reactor operation data irrelevant to the public interest and nuclear safety but necessary for flux analysis are accessible to the Reactor Working Group (RWG) of Daya Bay. We can obtain daily thermal power information and fission fraction information as a function of burnup from the reactor operation companies. However, we are only allowed to share the weekly information with other Daya Bay collaborators. To provide weekly thermal power and fission fraction data that can be used to calculate weekly neutrino fluxes in an unbiased way is essential for the analysis, the following issues need to be addressed:

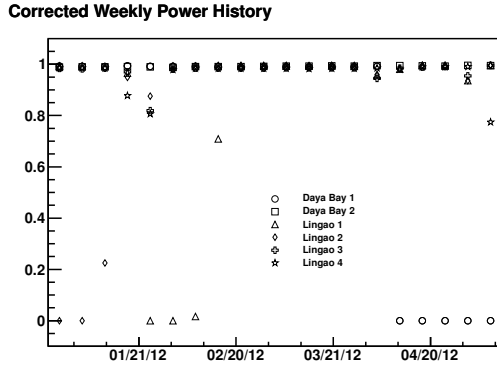


Figure 55. Thermal power vs time (weekly)

1. The mismatch between reactor up time and the detector up time causes bias. Imagine an extreme case: reactors are down the first half of the week while detectors are down the 2nd half of the week. Using weekly average power causes very large bias.
2. Weekly average fission fractions should only consider the time that both reactor and detectors are live.

Both issues are from the same cause, the mismatch between reactor and detector livetime. And they can be solved using the same approach: all weekly average values should be detector livetime and efficiency weighted average. For thermal power, we ask the operation company perform a DAQ livetime weighted hourly thermal time profile; for the fission fractions, we use the following weighted weekly average:

$$\bar{f}_i = \sum_{day=1}^7 f_{i,day} \frac{W_{th,day}}{\sum_{day=1}^7 W_{th,day}} \quad (4.2)$$

Ref. [45] and Ref. [46] show detailed reasoning and derivations.

The weekly effective thermal power and fission fractions are shown in Fig 55. and Fig. 56 as examples.

4.2 Reactor flux uncertainties

4.2.1 Reactor flux uncertainty sources

The following factors contribute to the reactor flux uncertainties:

1. Isotope spectrum uncertainties in $S_i(E)$
2. Thermal power uncertainties in W_{th}
3. Fission fraction uncertainties in f_i
4. Fission energy uncertainties in e_i
5. Off-equilibrium uncertainties
6. Spent nuclear fuel uncertainties

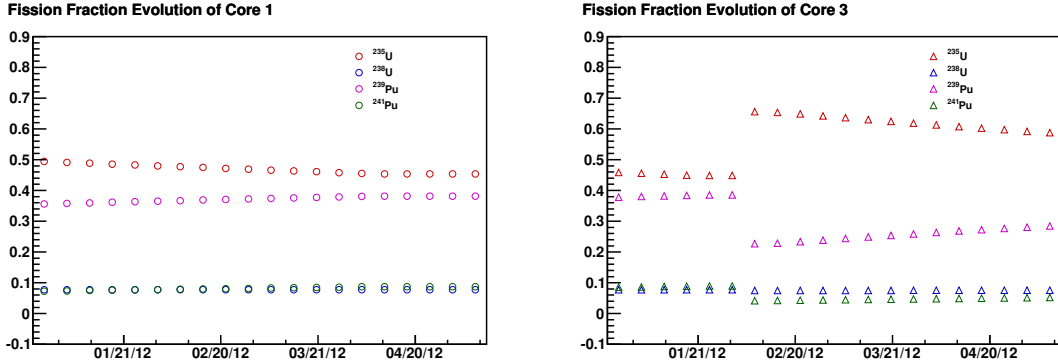


Figure 56. Fission fractions vs time (weekly). Left: Daya Bay core 1 fission fraction evolution; Right: Ling Ao Core1 fission evolution. Note there was a refueling in the 7th and 8th week thus the fission composition changed.

Depending on the assumptions in the correlations, there can be as many as ~ 144 systematic uncertainties associated with the reactor antineutrino flux. We will discuss each of these systematic uncertainties in the next section.

4.2.2 Uncertainties in fission isotope antineutrino spectra

Fission isotopes release antineutrinos in their beta decays. In principle, the spectra can be calculated starting from first principles. However, due to incomplete knowledge of all the fission product beta decays, such *ab initio* approach has very large uncertainties. Among the 4 dominant fission isotopes of PWR, ^{235}U , ^{239}Pu and ^{241}Pu fissions are dominantly induced by thermal neutrons and their decay beta spectra were accurately measured by the BILL spectrometer [47, 48, 49]. Antineutrino spectra can thus be converted from measured beta spectra, which provides more accurate antineutrino spectra than the *ab initio* approach. As for ^{238}U , because its fissions are mainly induced by fast neutrons, no experimental measurements have been performed. The antineutrino spectrum of ^{238}U fission products is calculated using the *ab initio* approach [50, 51].

Fission isotope antineutrino spectrum uncertainties are fully correlated among all reactors. For each isotope's own spectra, there are correlated components and uncorrelated ones among energies and isotopes. See Tab. 10 and Tab. 11 where only total uncertainties and correlated components are shown.

Old calculations (pre-2011) Based on the BILL beta spectrometer data taken in the 80's at ILL High Flux Reactor in Grenoble, the antineutrino spectra of ^{235}U , ^{239}Pu and ^{241}Pu are calculated in Ref. [47, 48, 49]. Table 10 shows the converted antineutrino spectra and correlated and total systematic uncertainties in each energy bin. For convenience, from here on, we label this calculation the “Old Flux”.

Re-evaluation in 2011 In 2011, two independent groups re-evaluated the BILL data using improved calculations. See Ref. [51, 52]. We here show the Huber calculation in Ref. [52] in Tab. 11. We label this set of re-evaluation as the “New Flux”.

Table 10. Antineutrino spectra based on BILL beta spectra (1980’s). Uncertainties are relative and in percentage.

$E_{\bar{\nu}_e}$	^{235}U	σ^{corr}	σ^{tot}	^{239}Pu	σ^{corr}	σ^{tot}	^{241}Pu	σ^{corr}	σ^{tot}
1.5	1.86	3	4.2	1.45	4.	5.2	1.56	4.	5.0
1.75	1.57	3	4.2	1.26	4.	5.2	1.42	4.	5.0
2	1.30E00	3	4.2	1.07	4.	4.5	1.24	4.	4.3
2.25	1.08E00	3	4.2	8.90E-01	4.	4.5	1.06	4.	4.3
2.5	9.00E-01	3	4.2	7.10E-01	2.5	4.3	8.70E-01	2.5	4.0
2.75	7.61E-01	3	4.2	5.99E-01	2.5	4.3	7.50E-01	2.5	4.0
3	6.37E-01	3	4.2	4.91E-01	2.5	4.3	6.23E-01	2.5	4.0
3.25	5.36E-01	3	4.2	3.97E-01	2.5	4.3	5.20E-01	2.5	4.0
3.5	4.37E-01	3	4.2	3.17E-01	2.5	4.3	4.20E-01	2.5	3.9
3.75	3.52E-01	3	4.2	2.48E-01	2.5	4.3	3.34E-01	2.5	3.9
4	2.83E-01	3	4.2	1.90E-01	2.0	4.4	2.70E-01	2.0	3.9
4.25	2.23E-01	3	4.2	1.48E-01	2.0	4.4	2.10E-01	2.0	3.9
4.5	1.72E-01	3	4.2	1.07E-01	2.0	4.8	1.57E-01	2.0	4.2
4.75	1.32E-01	3	4.2	7.90E-02	2.0	4.8	1.18E-01	2.0	4.2
5	1.05E-01	3	4.2	5.76E-02	2.0	5.2	9.20E-02	2.0	4.4
5.25	8.21E-02	3	4.2	4.41E-02	2.0	5.2	6.96E-02	2.0	4.4
5.5	6.17E-02	3	4.2	3.50E-02	2.5	5.9	5.25E-02	2.5	4.9
5.75	4.82E-02	3	4.2	2.66E-02	2.5	5.9	3.82E-02	2.5	4.9
6	3.70E-02	3	4.3	1.77E-02	2.5	6.8	2.76E-02	2.5	5.6
6.25	2.70E-02	3	4.3	1.26E-02	2.5	6.8	1.89E-02	2.5	5.6
6.5	2.03E-02	3	4.4	9.40E-03	2.5	7.4	1.39E-02	2.5	6.1
6.75	1.50E-02	3	4.4	6.94E-03	2.5	7.4	1.01E-02	2.5	6.1
7	1.05E-02	3.6	4.7	4.68E-03	3.0	11.0	6.83E-03	3.0	7.0
7.25	6.68E-03	3.6	4.7	3.05E-03	3.0	16.0	4.11E-03	3.0	7.0
7.5	4.29E-03	4.0	5.0	1.80E-03	3.0	19.0	2.54E-03	3.0	8.0
7.75	2.69E-03	4.0	5.4	8.80E-04	3.0	27.0	1.59E-03	3.0	8.0
8	1.36E-03	5.0	6.0	5.00E-04	5.0	35.0	8.90E-04	5.0	11.0
8.25	4.13E-04	5.0	7.0	3.50E-04	5.0	50.0	4.36E-04	5.0	17.0
8.5	2.37E-04	6.0	10.	2.20E-04	5.0	80.0	2.35E-04	5.0	24.0
8.75	1.29E-04	6.0	15.	0	5.0	100.0	1.20E-04	5.0	38.0
9	5.60E-05	7.0	27.	0	5.0	100.0	4.70E-05	5.0	90.0
9.25	2.20E-05	7.0	31.	0	5.0	100.0	0	5.0	100.0
9.5	1.40E-05	10.0	56.	0	5.0	100.0	0	5.0	100.0

The New Flux and the Old Flux are consistent within uncertainties as shown in Fig. 57. Due to improved calculations, the systematic uncertainties are now smaller for ^{235}U , ^{239}Pu , and ^{241}Pu , and the nominal antineutrino yields are higher, which are responsible for the so-called “Reactor Flux Anomaly” identified by Mention *et al* in Ref. [53]. The effect is 2.5σ thus sensitive to different

Table 11. Reevaluated fission isotope antineutrino spectra in 2011 by Huber. Uncertainties are relative and in percentage.

$E_{\bar{\nu}_e}$	^{235}U	σ^{corr}	σ^{tot}	^{239}Pu	σ^{corr}	σ^{tot}	^{241}Pu	σ^{corr}	σ^{tot}
2.00	1.32	1.73	1.82	1.08	1.94	2.60	1.26	1.78	2.47
2.25	1.12	1.73	1.84	0.92	1.97	2.60	1.08	1.79	2.41
2.50	0.915	1.74	1.87	0.719	2.01	2.51	0.894	1.80	2.29
2.75	0.77	1.76	1.88	0.62	2.06	2.60	0.777	1.82	2.33
3.00	0.651	1.78	1.93	0.515	2.12	2.91	0.641	1.86	2.43
3.25	0.553	1.82	1.95	0.398	2.18	3.09	0.536	1.90	2.46
3.50	0.454	1.87	2.01	0.329	2.25	3.27	0.439	1.95	2.54
3.75	0.364	1.93	2.08	0.261	2.33	3.30	0.346	2.01	2.45
4.00	0.294	1.99	2.14	0.195	2.42	3.42	0.282	2.08	2.56
4.25	0.23	2.07	2.27	0.157	2.51	3.95	0.22	2.15	2.87
4.50	0.179	2.15	2.45	0.113	2.60	4.90	0.166	2.24	3.36
4.75	0.138	2.24	2.54	0.0833	2.70	5.04	0.125	2.33	3.49
5.00	0.11	2.33	2.60	0.0613	2.80	4.73	0.0974	2.44	3.33
5.25	0.0864	2.44	2.63	0.0483	2.91	5.10	0.0747	2.55	3.42
5.50	0.0646	2.55	2.77	0.0354	3.02	5.73	0.0558	2.66	3.70
5.75	0.051	2.67	2.94	0.0292	3.13	6.37	0.0411	2.79	4.22
6.00	0.0389	2.79	3.15	0.0192	3.25	8.49	0.0305	2.92	4.96
6.25	0.0287	2.92	3.34	0.0128	3.37	9.36	0.0198	3.06	5.40
6.50	0.0217	3.06	3.38	0.00998	3.49	9.75	0.0154	3.20	5.54
6.75	0.0161	3.21	3.52	0.00754	3.61	10.55	0.0109	3.35	5.75
7.00	0.0114	3.36	3.77	0.00498	3.74	13.04	0.00775	3.51	5.94
7.25	0.00717	3.52	4.28	0.00326	3.86	18.21	0.00447	3.68	7.33
7.50	0.00464	3.68	4.55	0.00195	4.00	22.63	0.0029	3.85	8.60
7.75	0.00297	3.86	4.93	0.000847	4.13	26.78	0.00178	4.02	9.25
8.00	0.00162	4.03	6.97	0.000587	4.26	29.05	0.00106	4.20	12.44

^{238}U 's uncertainty assumptions which we will discuss more.

^{238}U fission spectrum *ab initio* approach No fission measurements were ever made for ^{238}U thus its fission spectrum can only be obtained via the *ab initio* approach [50, 51]. In our analysis, we consider two calculations made by Vogel *et al* in Ref. [50] and Mueller *et al* in Ref. [51]. The comparison of the two calculations are shown in Fig. 57(d). Although the Mueller calculation was done in 2011 based on improved nuclear database, the uncertainties are actually enlarged due to improved knowledge about missing information. Table 12 summarizes the antineutrino yields and their uncertainties.

As the ^{238}U uncertainties are due to either theoretical calculation or missing nuclear information, their values and correlations are difficult to evaluate[53]. Thus for their correlations, we face different options:

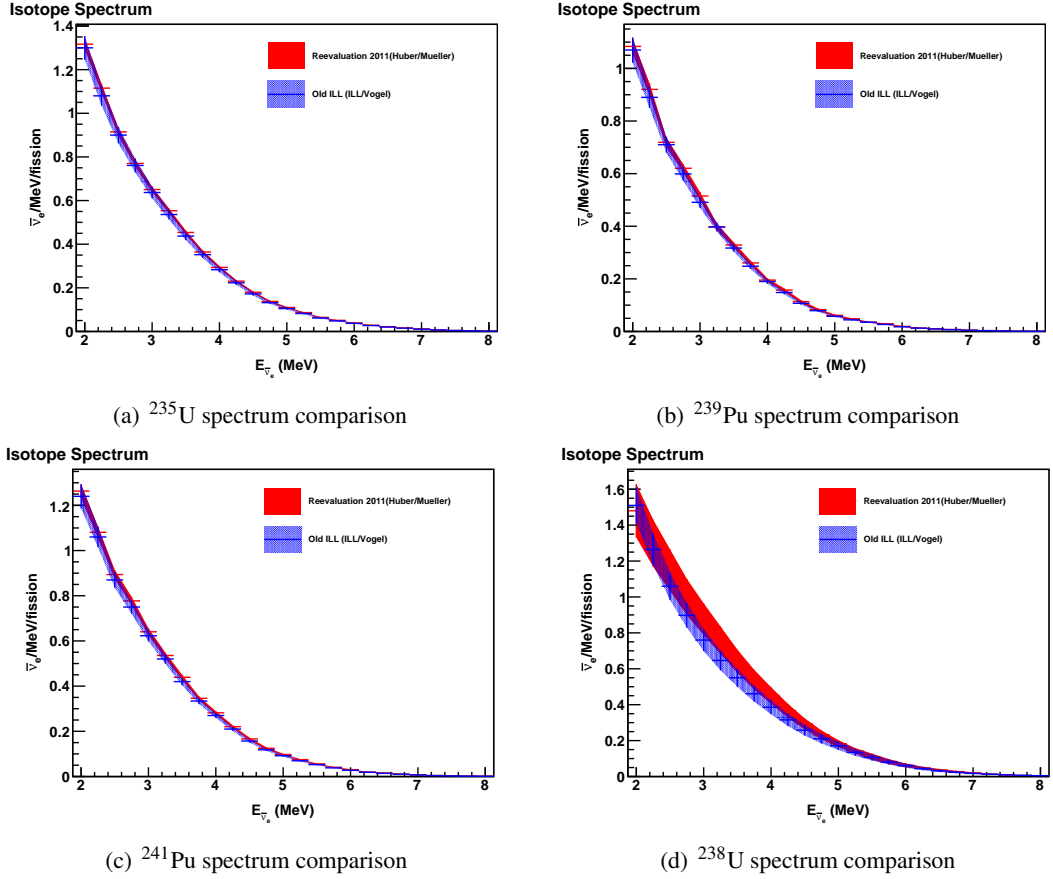


Figure 57. Comparison of the old isotope spectra from 1980’s and the new ones in 2011 by Huber and Mueller *et al.* ^{235}U , ^{239}Pu , and ^{241}Pu are converted from the beta spectra of the BILL data. The ^{238}U spectra are calculated based on an *ab initio* approaches. The previous calculation was done by Vogel *et al* in 1981 and the new one is by Mueller *et al* in 2011 based on improved nuclear database.

1. ^{238}U uncertainites are uncorrelated between bins and uncorrelated with other isotopes
2. ^{238}U uncertainites are fully correlated and correlated with other isotops’ correlated components
3. ^{238}U uncertainites are correlated between but uncorrelated with other isotopes

We found very different flux normalization uncertainties can be caused by different assumptions. Assumption 1 gives a contribution of 2% from isotope uncertainties but Assumption 2 contributes an uncertainty 3.5%. Assumption 3 leads to a 2.5% uncertainty contribution. To understand the ^{238}U contribution, it is helpful to work out the analytical expression of isotope caused normalization uncertainty,

$$\begin{aligned} \sigma_{iso}^2 &= \sigma_{iso}^{corr2} + \sigma_{iso}^{uncorr2} \\ \sigma_{iso}^{corr2} &= \sum_{i,j} \sum_{i',j'} F_i \sigma_j^{corr} F_{i'} \sigma_{i',j'}^{corr} + \sum_j F_{238}^2 \sigma_{238,j}^{corr2} \\ \sigma_{iso}^{uncorr2} &= \sum_{i,j} F_i^2 \sigma_{i,j}^{corr2}, \end{aligned} \quad (4.3)$$

Table 12. ^{238}U fission spectrum comparison of Vogel calculation in 1980 and Mueller *et al* in 2011 based on improved nuclear database

$E_{\bar{\nu}_e} (\text{MeV})$	Vogel <i>et al</i>	$\sigma^{tot} (\%)$	Mueller <i>et al</i>	σ^{tot}
2.00	1.5100	6.65	1.48	10.07
2.25	1.2651	6.99	1.30	10.08
2.50	1.0600	7.25	1.15	10.08
2.75	0.8976	7.67	1.00	10.08
3.00	0.7600	8.10	0.876	10.11
3.25	0.6465	8.53	0.759	10.16
3.50	0.5500	9.04	0.642	10.15
3.75	0.4608	9.64	0.539	10.27
4.00	0.3860	10.23	0.451	10.38
4.25	0.3156	10.92	0.367	10.45
4.50	0.2580	11.68	0.293	10.50
4.75	0.2100	12.45	0.232	10.57
5.00	0.1710	13.65	0.183	10.74
5.25	0.1346	14.59	0.143	10.96
5.50	0.1060	15.95	0.110	15.90
5.75	0.0801	17.40	0.0835	16.21
6.00	0.0605	18.68	0.0621	16.62
6.25	0.0437	20.22	0.0470	17.03
6.50	0.0315	21.84	0.0358	17.53
6.75	0.0234	23.80	0.0271	18.12
7.00	0.0174	26.02	0.0195	22.80
7.25	0.0127	28.15	0.0133	22.86
7.50	0.0093	30.71	0.00865	22.72
7.75	0.0066	34.30	0.00601	22.91
8.00	0.0047	38.31	0.00384	24.08

where σ_{iso}^2 is the absolute, fissions per second, flux normalization uncertainty caused by isotope uncertainties. σ_{iso}^{corr2} and $\sigma_{iso}^{uncorr2}$ represent the correlated and the uncorrelated components of the total uncertainty. $F_i \equiv \frac{W_{th}}{\langle e_{fission} \rangle} f_i$ is isotope i 's fission rates. $\sigma_{i,j}^{corr}$ and $\sigma_{i,j}^{uncorr}$ represent the correlated and uncorrelated uncertainties in the energy bins of each isotope's IBD yield per fission. i and i' represent different isotopes and j and j' are energy bin indices. Using Daya Bay Core 1 as an example core, during the P12B running period, the normalization uncertainty breakdown and ^{238}U contribution are shown in Table 13.

Although ^{238}U uncertainties cause very different reactor normalization uncertainties, they do not affect the oscillation analysis due to the near-far cancellation effect. As shown in Fig. 58 and Fig. 59, isotope spectrum uncertainties are practically fully correlated between all detectors thus cancelled out between near and far detectors in oscillation analysis. In our analysis, we are currently adapting Assumption 1.

Table 13. Total reactor normalization uncertainty breakdown and the contribution of ^{238}U . For Assumption 3, the ^{238}U contribution is calculated separately as it is uncorrelated with other correlated contributions.

Assumption	σ_{iso}^{corr} (%)	σ_{iso}^{uncorr} (%)	^{238}U Contribution (%)	σ_{iso} (%)
1	1.96	0.39	0.33, included in σ_{iso}^{uncorr}	2.0
2	3.44	0.21	included in σ_{iso}^{corr}	3.45
3	1.96	0.21	1.48	2.47

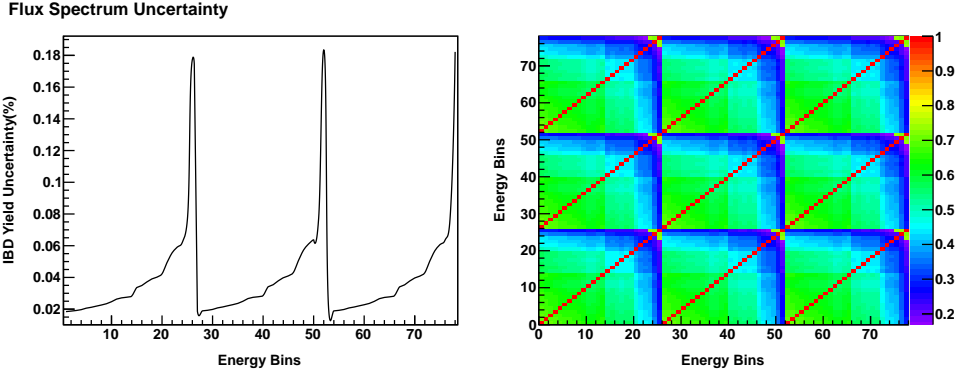


Figure 58. Left: the IBD uncertainties in each bin of the 3 sites caused by isotope spectrum uncertainties; Right: IBD uncertainty correlations between different bins of different sites: corresponding bins at different sites are almost fully correlated thus the isotope uncertainty caused flux uncertainties get cancelled out largely. These results are based on Assumption 1, *i.e.* ^{238}U uncertainties are uncorrelated.

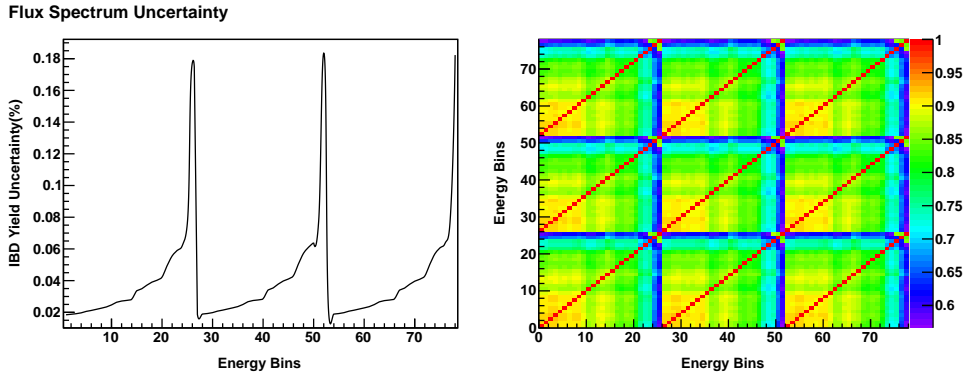


Figure 59. Results are based on Assumption 3, *i.e.* ^{238}U uncertainties are correlated between bins but uncorrelated with other isotopes.

Total uncertainties and correlations in fission isotopes Figure 58 and Fig. 59, show the uncertainties and the correlations between different bins of two different assumptions on the nature of the ^{238}U uncertainty correlation.

4.2.3 Nuclear reactor related uncertainties

Thermal power uncertainty It has been widely accepted that the thermal power measurement of modern PWRs can reach 0.5% [54] precision and accuracy. Thus they are absolute uncorrelated

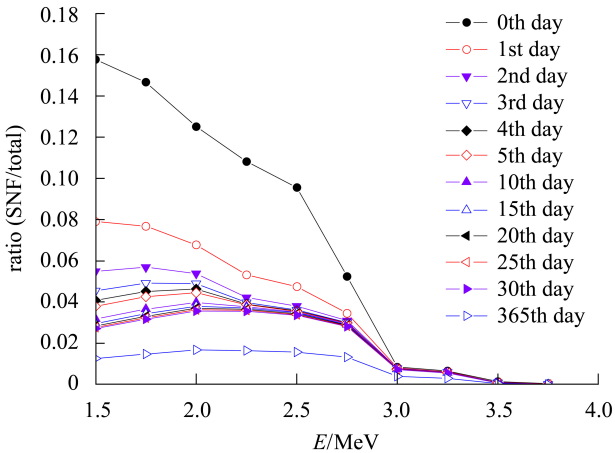


Figure 60. SNF spectrum evolution over time by Zhou *et al*: in the energy of interest, *i.e.* $> 1.806\text{MeV}$, the SNF spectrum is steeper when first removed from the core then becomes fairly flat. As SNF stays in the same pool for 5 years, we should add a time averaged spectrum to the antineutrino flux.

uncertainties between reactors.

Spent nuclear fuel flux Spent nuclear fuel (SNF) is generally stored in the same water pool which hosts reactor cores that produce those nuclear wastes. SNF could stay 10 to 20 years in the water pool before being moved to permanent storage places. While in pools, SNF continues to produce electron antineutrinos via beta decays and needs to be included in the reactor antineutrino flux. For our purpose, there are two time scales in SNF beta decays, see Fig. 60 taken from Ref. [55].:

1. Fast decay fission isotopes whose lifetime is on the order of days and less. Right after the reactor is shut off for refueling, the reactor, whose 1/3 fuel rods will become SNF, continues to give out antineutrinos.
2. Slow decay isotopes whose lifetimes are on the order of hundreds of days and beyond. After a few hundreds days, short-lived isotopes from SNF have decayed away. The long-lived isotopes like ^{90}Sr have lifetime on the orders of dozens of years thus the SNF spectrum becomes relatively stable.

The SNF calculation in the BCW analysis uses the 5-year average spectrum shape calculated in Ref. [56] and Ref. [57] shown in Fig. 61. The time evolution of the spectrum can be seen in Fig. 60. The SNF spectrum shape becomes fairly stable and flat after a year. We take time averaged spectrum from Ref. [57] as the SNF background and only allow the total normalization uncertainty, which means SNF uncertainty is correlated in energy. Between different reactors, SNF uncertainty is uncorrelated since each reactor has its own SNF accumulation and storage arrangement. The total SNF contribution is 0.3% in the energy range of 1.806MeV and 3.5MeV according to An *et al*'s calculation and its uncertainty is taken to be 50%. Figure 61 shows the SNF antineutrino yield fraction in the first 7 bins starting from the threshold energy 1.806MeV , $[1.806, 2.125]$, $[2.125, 2.375]$, $[2.375, 2.625]$, \dots , $[3.375, 3.625]$.

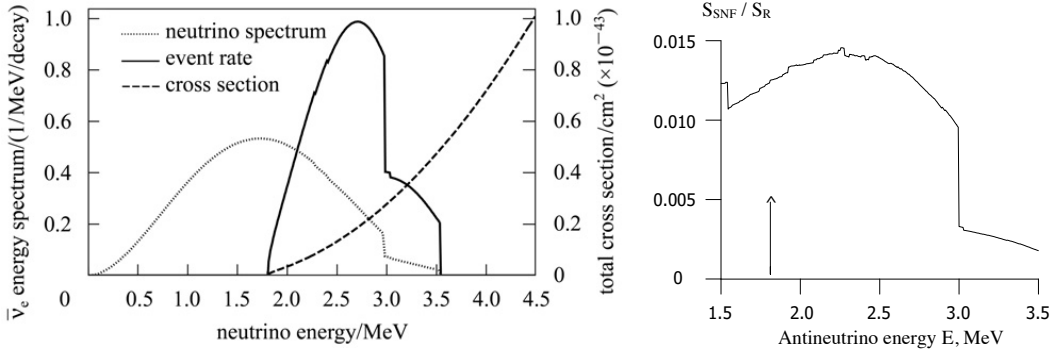


Figure 61. Left: the 5-year average SNF spectrum calculated by An *et al*; Right: time averaged SNF spectrum calculated by Kopeikin *et al*. In our uncertainty evaluation, the SNF IBD normalization is controlled to be 0.3% in the energy range of 1.806MeV and 3.54MeV where SNF spectrum ends according to An *et al*'s calculation.

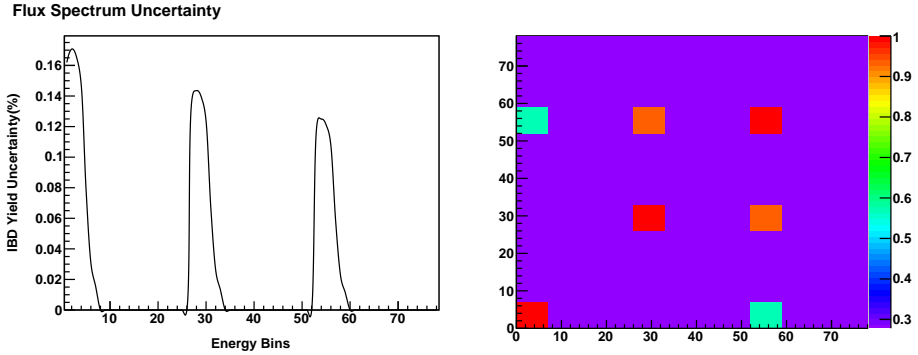


Figure 62. Left: SNF caused IBD spectrum uncertainty; Right: SNF uncertainty correlations between the bins of 3 sites. As we treat SNF flux uncorrelated between reactors, we see the is very little correlation between site 1 and site 2, which is expected.

Treating SNF as uncorrelated from reactor to reactor, we have evaluated the correlation matrix for its uncertainties in Fig. 62. Also, in Fig. 62, the SNF caused IBD uncertainties in each energy bin is evaluated.

Off-equilibrium correction Among the fission products of the 4 isotopes, about 10% have lifetime long enough to keep accumulating. In addition, some fission isotopes capture neutrons then go through beta decays. Their contributions to the antineutrino flux are of the order of a few percent, mainly below ~ 4.5 MeV. We currently use the corrections calculated by Mueller *et al*[51]. The off-equilibrium correction in principle should be time averaged. As the Daya Bay fuel cycle is ~ 1 year and every fuel rod stays in the core for 3 cycles, we use the 300-day correction numbers taken from Ref. 14 as the time averaged values and the uncertainty is energy bin correlated. Off-equilibrium correction caused IBD uncertainties in each bin and their correlations are shown in Fig. 63.

Fission fractions The nuclear fuel composition or fission fractions evolves with time as the reactor goes through fission processes to produce heat. Because the 4 dominant isotopes ^{235}U , ^{238}U , ^{239}Pu , and ^{241}Pu produce different antineutrino spectra, the resulting flux shape also evolves with

Table 14. Off-equilibrium corrections to the antineutrino spectrum and uncertainties

Isotope	2.0MeV	2.5MeV	3.0MeV	3.5MeV	4.0MeV
^{235}U	5.3%	4.0%	1.3%	0.7%	0.1%
^{239}Pu	1.8%	1.4%	0.4%	0.1%	0.1%
^{241}Pu	1.6%	1.1%	0.4%	0.1%	0.1%
Uncertainty	30% (on the total normalization)				

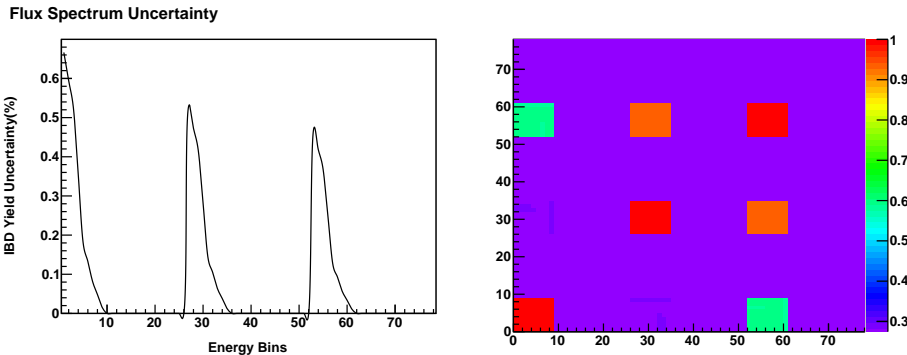


Figure 63. Left: Off-equilibrium correction caused IBD spectrum uncertainties; Right: Off-equilibrium caused uncertainty correlations between the bins of 3 sites. As we treat off-equilibrium effect uncorrelated between reactors, we see there is very little correlation between site 1 and site 2, which is expected.

time. Fission fractions are calculated using reactor core simulation code [58, 59] and the code has been validated using the so-called Takahama benchmark [58]. The uncertainties in fission fractions thus cause uncertainties in antineutrino flux. Fission fractions are correlated naturally due to conservation of the total heat production and the breeding processes in the reactor core [54, 59]. Based on the Daya Bay reactor configuration, Xubo Ma *et al* re-evaluated the correlation between the four isotopes and their uncertainties in DocDB-7413 [59] and DocDB-8163 [60]. The correlation matrix between the four fission fractions is shown in Eq. 4.4.

$$C_{fraction} = \begin{pmatrix} 1 & -0.22 & -0.53 & -0.18 \\ -0.22 & 1 & 0.18 & 0.26 \\ -0.53 & 0.18 & 1 & 0.49 \\ -0.18 & 0.26 & 0.49 & 1 \end{pmatrix} \quad (4.4)$$

Fission fraction uncertainties are 0.71%, 4.2%, 2.1% and 3.5% for ^{235}U , ^{238}U , ^{239}Pu and ^{241}Pu respectively according to Ma's calculation in DocDB-7413 [59] and they follow the correlation above.

There are two ways to incorporate the fission fraction correlation matrix in the analysis:

1. Directly apply nuisance parameters on the 4 fission fractions and the total penalty is calculated using the correlation matrix. This is the most straightforward way of treating the original correlated uncertainties in pull method.
2. Propagate the fission fraction uncertainties to the final reactor flux then nuisance parameters are applied to the final reactor flux. To propagate the correlated uncertainties, one can apply

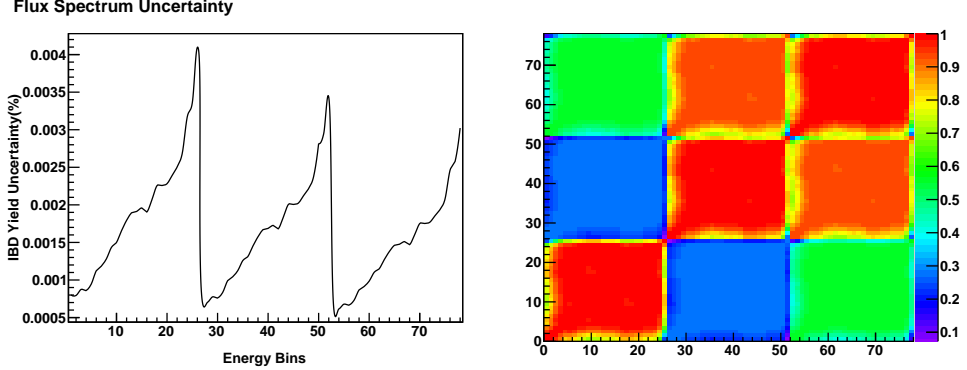


Figure 64. Total flux error caused by fission fraction uncertainties and their correlations.

Table 15. Fission energy from Kopeikin and Xubo Ma et al. We use Xubo Ma's numbers in our analysis.

Fission Isotopes	Kopeikin <i>et al</i> (MeV)	Ma <i>et al</i> (MeV)
^{235}U	201.92 ± 0.46	202.25 ± 0.39
^{238}U	205.52 ± 0.96	205.87 ± 0.55
^{239}Pu	210.99 ± 0.60^9	211.41 ± 0.32
^{241}Pu	213.60 ± 0.65	214.47 ± 0.36

Cholesky decomposition to the correlation matrix $C_{fraction}$ then generate correlated fission fraction fluctuations that obey the correlation matrix then evaluate the resulting uncertainty. We will talk more about this method later on. Find the lower diagonal matrix U so that $C_{fraction} = UU^T$, then we have found the Cholesky decomposition of $C_{fraction}$. For Eq. 4.4, we have

$$U = \begin{pmatrix} 1 & 0 & 0 & 0 \\ -0.22 & 0.9755 & 0 & 0 \\ -0.53 & 0.06499 & 0.8455 & 0 \\ -0.18 & 0.2259 & 0.4493 & 0.8454 \end{pmatrix} \quad (4.5)$$

Figure 64 shows the total uncertainties cause by fission fractions and their correlations for Daya Bay core 1. We see that the uncertainty exceeds 1% after ~ 6 MeV and it could be as large as 2.5% at high energies and the correlation is over all strong and positive.

Fission energy Fission energy is the energy source of nuclear reactors. Its connection with the reactor antineutrino is shown in Eq. 4.1. The part of the energy that is converted to heat, e_i , changes with the fuel composition as fission reactions develop in the reactor. Table 15 shows the results from Ref. [61] and Xubo Ma *et al* [62]. Ref. [62] re-evaluated the fission energy using Daya Bay core configuration thus we adapt these Daya Bay calculations in our analysis.

As fission energy is completely correlated among all reactors, they cause 100% correlation in all detectors also. Figure 65 shows this effect.

Total reactor caused uncertainties and their correlation As all the uncertainties are independent of one another, their contributions to the final IBD uncertainty can be added together in quadrupole approximation.

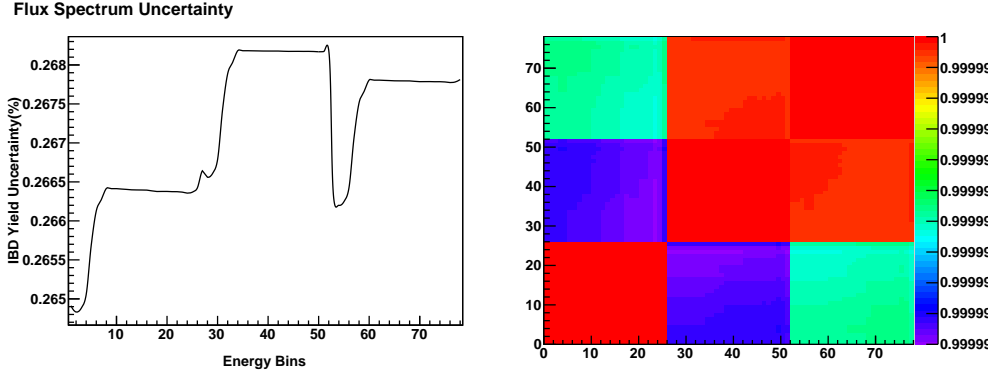


Figure 65. IBD spectrum errors caused by fission energy uncertainties and their correlations.

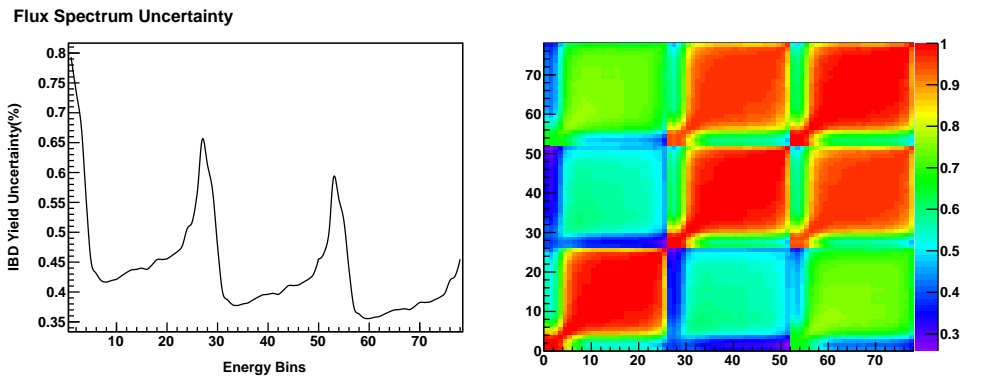


Figure 66. Total IBD spectrum errors caused by reactor uncertainties and their correlations.

ture. In other words, to evaluate reactor uncertainties effect to IBD spectrum, we simply add all the covariance matrices we have calculated in previous sections together. Figure 66 shows the total spectrum uncertainty caused by reactor uncertainties and their correlation.

4.3 Flux uncertainty treatment: covariance matrix + pull

4.3.1 Pull-covariance approach

If all reactor flux errors are treated based on their original definition (~144 terms depending on correlation assumptions¹⁰), the chi-square of a Neyman pull approach can be generalized to the following expression,

$$\chi^2 = \chi_{stat}^2(n_i^{obs}, n_i^{exp}, \eta_j, \dots) + \sum_{j=1}^{144} \left(\frac{\eta_j}{\sigma_j^r} \right)^2 + \text{sum}(\text{non-flux sys penalty}), \quad (4.6)$$

where $\chi_{stat}^2(n_i^{obs}, n_i^{exp}, \eta_j, \dots)$ is a general way to write the statistical part of the chi-square function. We will elaborate more in the format of χ_{stat}^2 in the next section when we come to oscillation

¹⁰In the original ILL or year 2011 re-evaluation of fission isotope spectra, 25 energy bins are chosen from 2MeV to 8MeV. Each bin has correlated and uncorrelated uncertainties. Counting all of them together with reactor uncertainties, we have in total 144 systematic uncertainties for reactor flux.

analysis. n_i^{obs} and n_i^{exp} are the observed and expected number of events in i , σ_j^r is the systematic uncertainties in reactor fluxes. The correlation caused by reactor flux uncertainties is reflected in the calculation of $n_i^{exp} = n_i^{exp}(\theta_{13}, \Delta m_{ee}^2 | \eta_j, \dots)$. There are two challenges in this “raw” way of implementing the flux uncertainties:

1. Number of parameters that the minimizer has to minimize over, which could cause numerical instability.
2. Complicated corrections reflected in the implementing of nuisance parameters η_j in n_i^{exp} as corrections in true neutrino energy need to go through all the reactor and detector effects.

Considering those two challenges, we propose to merge all the true energy related flux uncertainties into a covariance matrix so that: 1. number of parameters is reduced; and 2. certain detector effects can be included in the covariance matrix then new nuisance parameters can be applied at a later stage of the n_i^{exp} calculation thus reduce the numerical burden. Now the pull-covariance chi-square expression follows the following format,

$$\chi^2 = \chi_{stat}^2(n_i^{obs}, n_i^{exp}, \delta_j, \dots) + \sum_{j,j'=1}^{78} \delta_j (V^{-1})_{jj'} \delta_{j'} + \sum (\text{non-flux sys penalty}), \quad (4.7)$$

where V is the covariance matrix of the 78 nuisance parameters δ_j which is based on the original 144 reactor flux systematic uncertainties. Now the prediction is calculated based on less nuisance parameters δ_j , $n_i^{exp} = n_i^{exp}(\theta_{13}, \Delta m_{ee}^2 | \delta_j, \dots)$, and we can choose more convenient prediction stage to have them implemented.

The total number of nuisance parameters of 78 comes from the 26¹¹ reactor flux energy bins of 3 experimental sites. **Since there are inter-site correlations, we need to include all 78 bins to fully reflect the global correlation due to contributions from all reactors at each site. We will futher discuss the inter-site correlation in Sec. 4.3.2.**

4.3.2 Evaluation of the flux covariance matrix

Elements of the relative flux uncertainty covariance matrix between the energy bins of different sites¹² is defined in the following way,

$$V_{IJ} = \sigma\left(\frac{\delta\Phi_{ij}}{\Phi_{ij}}, \frac{\delta\Phi_{i'j'}}{\Phi_{i'j'}}\right) = \frac{\sigma(\delta\Phi_{ij}, \delta\Phi_{i'j'})}{\Phi_{ij}\Phi_{i'j'}}, \quad (4.8)$$

where $\Phi_{ij} \equiv \int_{\text{bin } j} dE \Phi_i(E) \sigma(E)$ and $\Phi_i(E)$ is the antineutrino flux at site i . Thus Φ_{ij} is the j -th energy bin’s total number of IBDs per unit time per unit target mass of site i . Global energy bin indices $I = (i-1)*26 + j$ and $J = (i'-1)*26 + j'$. Symble δ means absolute uncertainty and $\frac{\delta\Phi_{ij}}{\Phi_{ij}}$ is the relative uncertainty. Based on the formalism above, we simply need to calculate the absolute covariance $\sigma(\delta\Phi_{ij}, \delta\Phi_{i'j'})$. We will ignore the mentioning of “per unit time per target mass” as rate and total number of events have the same relative covariances. We might also ignore the index I and J in our following notations when it does not cause confusion for the sake of simplicity.

¹¹We extend the original reactor spectrum of 25 bins, (1.875, 8.125) MeV, by 2 bins using extrapolation technique to cover the spectrum up to 12MeV

¹²We use the hall center coordinates to represent the site location.

Since we have 6 reactor in Daya Bay, the total number of IBDs in bin j at site i is

$$\Phi_{ij} = \sum_{k=1}^6 \frac{1}{4\pi L_{ik}^2} \phi_{kj}, \quad (4.9)$$

where L_{ij} is the baseline between reactor j and site i . ϕ_{kj} is the total number of IBDs in bin j that reactor k can contribute without baseline effect. For simplicity, we will just call it reactor flux though it is not really the antineutrino flux but effective IBD “flux”. The absolute uncertainties between different energy bins now become

$$\delta\Phi_{ij} = \sum_{k=1}^6 \frac{1}{4\pi L_{ik}^2} \delta\phi_{kj} = \sum_{k=1}^6 w_{ik} \delta\phi_{kj}, \quad (4.10)$$

where we have defined the “weighting factor”, $w_{ij} \equiv 1/4\pi L_{ik}^2$, of reactor k for detector i due to geometric effect.

The absolute uncertainties in reactor flux $\delta\phi_{kj}$ are the quadrature sum of all systematic uncertainties since they are independent of one another,

$$\delta\phi_{kj} = \delta\phi_{kj}^{thermal} \oplus \delta\phi_{kj}^{fraction} \oplus \delta\phi_{kj}^{offeq} \oplus \delta\phi_{kj}^{snf} \oplus \delta\phi_{kj}^{fission} \oplus \delta\phi_{kj}^{iso}. \quad (4.11)$$

Thus 3-site flux spectrum absolute uncertainties covariance matrix can be expressed as,

$$\begin{aligned} \sigma(\delta\Phi_{ij}, \delta\Phi_{i'j'}) &= \sum_k \sum_{k'} w_{ik} w_{i'k'} \sigma(\delta\phi_{kj}, \delta\phi_{k'j'}) \\ &= \sum_{sys} \sum_k \sum_{k'} w_{ik} w_{i'k'} \sigma(\delta\phi_{kj}^{sys}, \delta\phi_{k'j'}^{sys}), \end{aligned} \quad (4.12)$$

where $k, k' = \overline{1\dots6}$, $\sigma(\delta\phi_{kj}, \delta\phi_{k'j'})$ is the total covariance between energy bin j of reactor k and bin j' of reactor k' and $\delta\phi_{kj}^{sys}$ represents the absolute uncertainty caused by a particular systematic uncertainty sys which runs through all the independent uncertainties in Eq. 4.11. Different systematic uncertainty caused relative covariance matrices $V^{sys} \equiv \sum_k \sum_{k'} w_{ik} w_{i'k'} \sigma(\delta\phi_{kj}^{sys}, \delta\phi_{k'j'}^{sys}) / \Phi_{ij} \Phi_{i'j'}$'s have been fully evaluated in previous sections, thus the total relative spectrum covariance matrix for 3 sites is,

$$V = V^{thermal} + V^{fraction} + V^{offeq} + V^{snf} + V^{fission} + V^{iso}. \quad (4.13)$$

The first line of Eqn. 4.12 also tells that the 3-site spectrum covariance matrix can be expressed as linear combinations of reactors' spectrum covariances. This is convenient for calculation purposes. We also note that: **if energy bin correlations are different between reactors, energy bin correlations must be different between different sites.**

4.3.3 Testing different isotope spectrum calculations

To test the effects of different flux calculations to our oscillation analysis, we evaluated the reactor fluxes and their uncertainty covariance/correlation matrices with the following 3 different combinations of fission isotope spectrum calculations.

1. Old ILL isotope spectra with ^{238}U spectrum calculated by Vogel. See Fig. 67 for the total error of each energy bin at the far site.

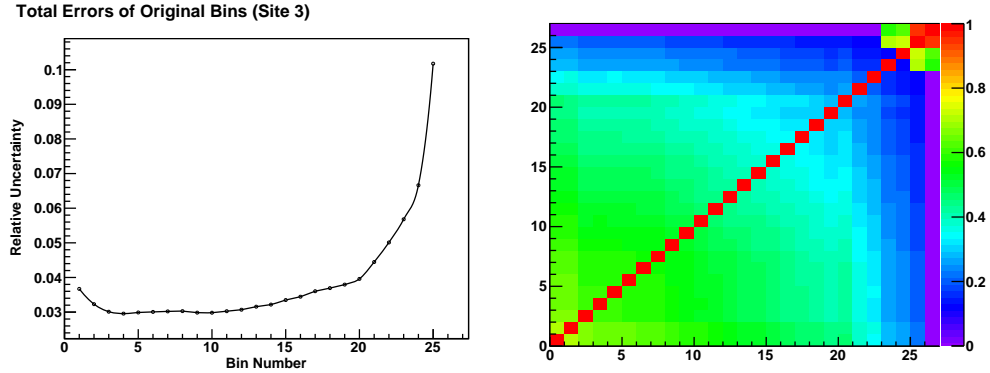


Figure 67. Far site reactor flux uncertainty and correlation using the old ILL fission isotope spectrum calculation and the ^{238}U spectrum by Vogel

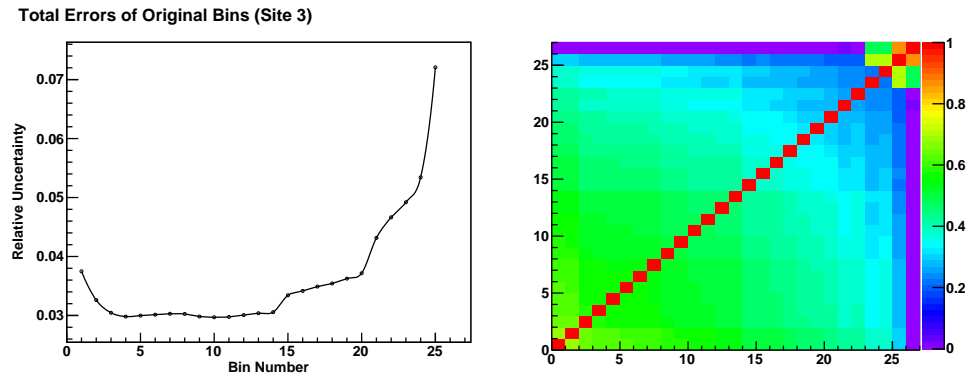


Figure 68. Far site reactor flux uncertainty and correlation using old ILL isotope spectrum calculation combined with the ^{238}U spectrum by Mueller *et al*

2. Old ILL isotope spectra with ^{238}U spectrum calculated by Mueller *et al*. See Fig. 68 for the total error of each energy bin at the far site.
3. New isotope spectra calculated by Huber with ^{238}U spectrum by Mueller *et al*. See Fig. 69 for the total error of each energy bin at the far site.

Besides obviously different systematic uncertainties, different isotope spectrum calculations have slightly different energy correlations also.

4.3.4 Uncertainties and correlations of all 3 sites

As we commented in Sec. 4.3.1, inter-site correlations need to be considered in our analysis due to different inter energy bin correlations at different sites and the site to site correlations due to the fact that all sites detect antineutrinos from all reactors. We here check how different they are to give us a sense of scale. We use the 2011 re-evaluated isotope fluxes as an example. As covariances can be conservative by taking the larger values among the 3 sites, correlations need to be proper for the shape analysis. Thus, we will show the comparison between the 3 sites' correlation matrices.

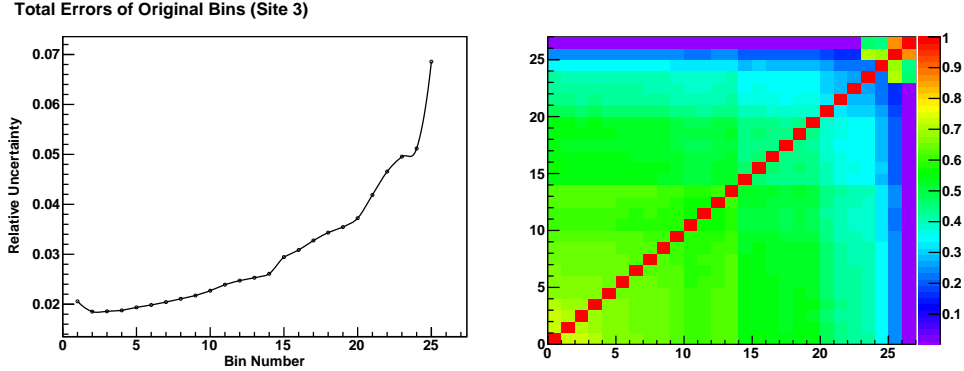


Figure 69. Far site reactor flux uncertainty and correlation using Huber's fission isotope spectrum calculation and ^{238}U by Mueller *et al*

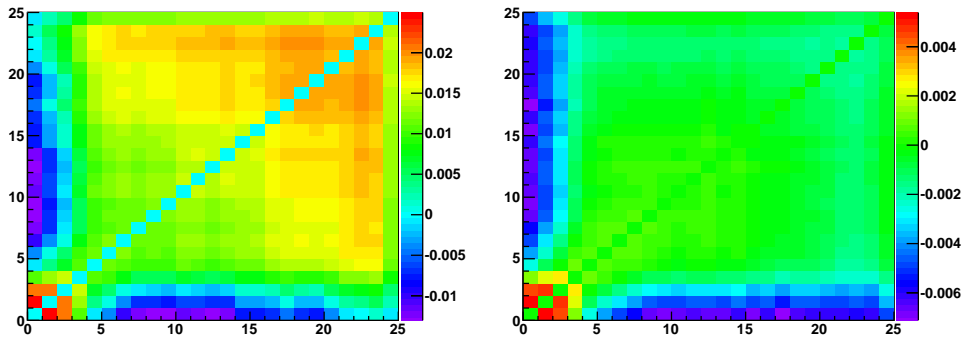


Figure 70. Left: the correlation matrix term by term differences between Site 1 and Site 3; Right: the correlation matrix term by term differences between Site 2 and Site 3.

First, let us check the absolute differences using the far site correlation matrix as the reference. Figure 70 shows the correlation matrix differences.

The differences are smaller between Site 2 and Site 3, which is understandable as they are both dominantly, $> 50\%$, affected by the Ling Ao site reactors. The differences are mainly in the correlations between energy bins $< 1.5\text{ MeV}$ and the ones about 1.5 MeV . Between Site 1 and Site 3, in addition, differences between energy bins in the range of $(6\text{ MeV}, 8\text{ MeV})$ are more significant — reaching 2% level. Figure 71 shows the relative differences between near sites and far sites.

As the correlations between different energy bins are noticeably different at different sites, it is important for the shape analysis to treat these site to site correlations properly. Thus, a correlations matrix of all energy bins of all sites correlation matrix is needed for the proper shape analysis. Our final bin uncertainties are shown in Fig. 72 and their correlation matrix, 78×78 , is shown in Fig. 73.

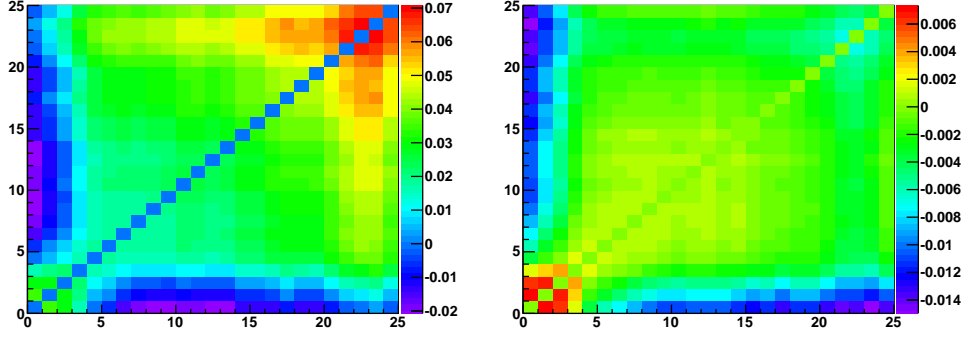


Figure 71. Left: the correlation matrix term by term relative differences between Site 1 and Site 3 using Site 3 one as the reference; Right: the correlation matrix term by term relative differences between Site 2 and Site 3. We see that for Site 1, its spectrum energy correlation differences with the far site are greater than 2% for most of the energy bins.

Flux Spectrum Uncertainty

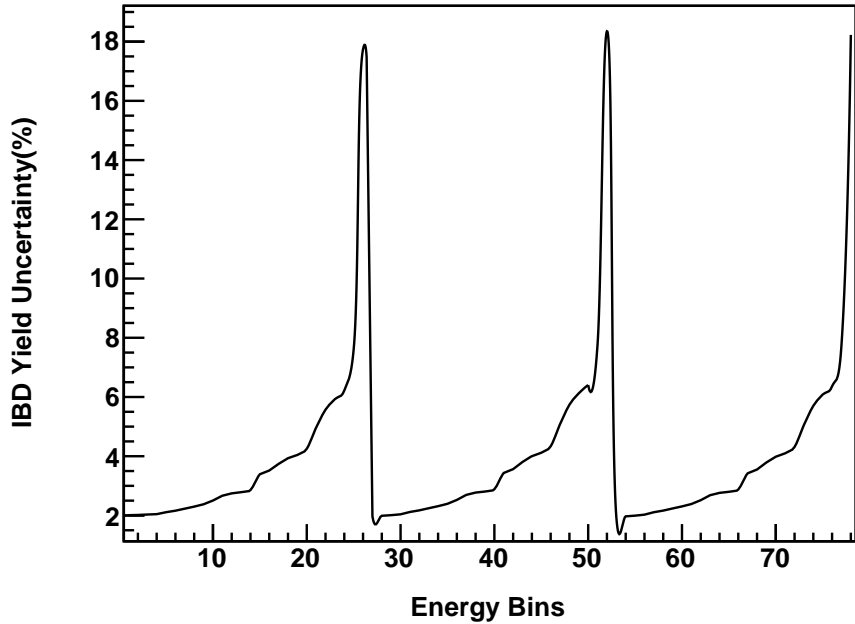


Figure 72. The IBD uncertainties of the energy bins of all experiment sites. Note that they include both the correlated and uncorrelated components. We also know the correlated components caused by isotope spectrum uncertainties dominate.

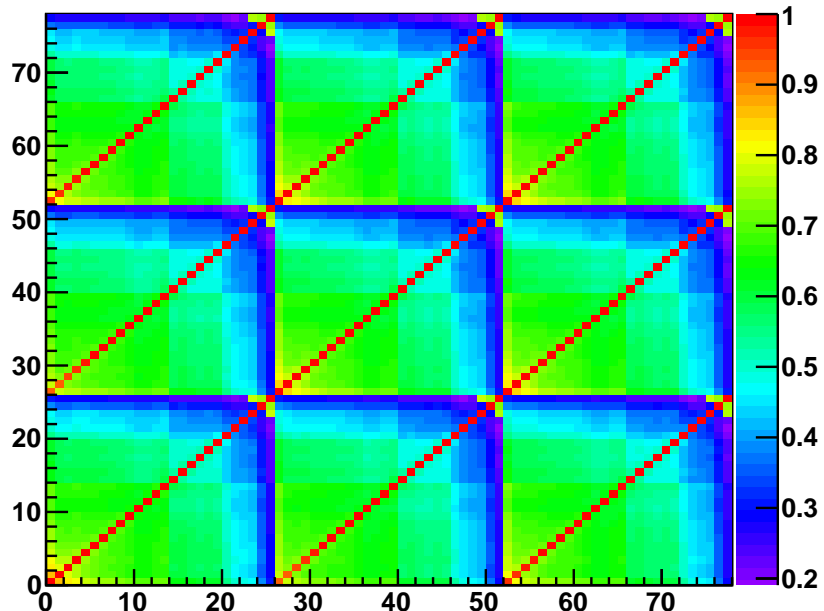


Figure 73. The correlation matrix of all energy bins of all experiment sites. We see the corresponding bins at different sites are strongly correlated as expected, which shows the power of the near-far flux uncertainty cancellation. However, the correlation is not exactly 1, meaning the flux uncertainty cancellation is not 100%. Detailed simulation in CDR shows a 1/20 suppression in the flux uncertainty, consistent quantitatively with our findings.

5. Oscillation Analysis

Since the reactor information is blinded after May 11, 2012, *all the oscillation analysis results presented in this section only use the data set from Dec 25, 2011 to May 11, 2012, the same data set as in the CPC paper.*

5.1 Rate-only analysis

The rate-only analysis uses the same method as described in the tech-note (doc:7621 [35]) of the February BCW θ_{13} analysis. Since the shape information is not used in the analysis, the uncertainty on θ_{13} will be worse than the rate+shape analysis. On the other hand, the rate-only analysis depends only on the integrated number of events over the whole reactor spectra in each detector. Being less sensitive on the detailed energy response model, the rate-only analysis is less prone to a systematic bias in the result.

Following Eq. [33.12] from PDG, the statistical component of the chi-square, χ^2_{stat} can be constructed from the Poisson likelihood comparing a measured number of entries N^{obs} with an expected value N^{exp} is,

$$\chi^2(\boldsymbol{\theta}, |\delta^{corr}, \delta^{osc}, \delta^r, \delta^{AD}, \delta^b) = -2\ln\lambda(\boldsymbol{\theta} | \delta^r, \delta^{AD}, \delta^b) = 2 \left(N^{exp} - N^{obs} + N^{obs}\ln\frac{N^{obs}}{N^{exp}} \right). \quad (5.1)$$

The expected value $N^{exp} \equiv N^{exp}(\boldsymbol{\theta} | \delta^{corr}, \delta^{osc}, \delta^r, \delta^{AD}, \delta^b)$ is predicted by a model with the unknown parameter(s) $\boldsymbol{\theta}$ and all systematic nuisance parameters $\delta^{corr}, \delta^{osc}, \delta^r, \delta^{AD}$ and δ^b whose definitions are shown in Tab. 17. $\boldsymbol{\theta}$ includes unknown parameters θ_{13} the mixing angle and, depending on our choice, the atmospheric mass-squared splitting Δm_{32}^2 . By default, we don't consider Δm_{32}^2 unknown in the rate analysis so we only fit for θ_{13} . The observed number N^{obs} is measured from the data.

A common approach to account for model uncertainty, *i.e.* to implement the nuisance parameters, is to include penalty terms δ_m , each constrained by the corresponding uncertainty, σ_m . For the specific case of the expected rate of antineutrino interactions in detector j due to reactor core k , we can replace the nominal rate R_{jk} with a modified rate \tilde{R}_{jk} by taking the systematic corrections to the first order,

$$\tilde{R}_{jk} = R_{jk}(1 + \delta_j^{corr})(1 + \delta_j^{AD})(1 + \delta_k^r). \quad (5.2)$$

The systematic uncertainty terms have been discussed in previous sections and summarized in Table 17. Any uncertainties that are correlated across all detectors or reactors are combined in σ_j^{corr} . All uncertainties which are specific to one detector or one reactor are combined into σ_j^{AD} or σ_k^r respectively.

In a similar fashion, the estimate of expected backgrounds b_{jn} can be replaced with \tilde{b}_{jn} ,

$$\tilde{b}_{jn} = b_{jn}(1 + \delta_{jn}^b). \quad (5.3)$$

where n enumerates over each background type that is discussed in section 3: accidentals, ${}^9\text{Li}/{}^8\text{He}$, fast neutrons, correlated ${}^{241}\text{Am}{}^{13}\text{C}$ and ${}^{13}\text{C}(\alpha, n){}^{16}\text{O}$. The background uncertainties σ_{jn}^b is actually not all independent, for example, ${}^9\text{Li}/{}^8\text{He}$ and fast neutrons are correlated at the same site, and ${}^{241}\text{Am}{}^{13}\text{C}$ uncertainties are correlated in all ADs. In practice, it is useful to remove degeneracy

between penalty parameters. In the rate-only analysis, all background terms are summed and is dominated by the accidentals. The other backgrounds are less than 0.6% compared with IBD signals so the precise treatment of uncertainty is not necessary. In the following presented analysis, all background terms in each AD are combined into one,

$$\tilde{b}_j = b_j(1 + \delta_j^b). \quad (5.4)$$

and δ_j^b is assumed to be un-correlated among ADs. The expected number of events in detector j then becomes

$$N_j^{exp} = \tilde{N}_j + \tilde{B}_j = \sum_{\Delta T}^{weeks} \left(\sum_k^{cores} \tilde{R}_{jk} + \tilde{b}_j \right). \quad (5.5)$$

The distortion from penalty terms are included in the expected number of reactor antineutrino and background events, \tilde{N}_j and \tilde{B}_j respectively.

The total χ^2 including all detectors and penalty terms is,

$$\chi^2(\boldsymbol{\theta} | \delta^{corr}, \delta^{osc}, \delta^r, \delta^{AD}, \delta^b) = 2 \sum_j^{ADs} \left(N_j^{exp} - N_j^{obs} + N_j^{obs} \ln \frac{N_j^{obs}}{N_j^{exp}} \right) + \chi^2_{penalty}, \quad (5.6)$$

where the penalty component is,

$$\chi^2_{penalty} = \left(\frac{\delta^{corr}}{\sigma^{corr}} \right)^2 + \sum_j^{ADs} \left(\frac{\delta_j^{AD}}{\sigma_j^{AD}} \right)^2 + \sum_k^{cores} \left(\frac{\delta_k^r}{\sigma_k^r} \right)^2 + \sum_j^{ADs} \left(\frac{\delta_j^b}{\sigma_j^b} \right)^2 + \sum_m^{osc} \left(\frac{\delta_m^{osc}}{\sigma_m^{osc}} \right)^2. \quad (5.7)$$

Each penalty parameter δ contributes to the χ^2 according to the independently measured uncertainty σ . Deviations of neutrino oscillation parameters from existing measurements, δ_m^{osc} , may be included as shown in the final term. This term assumes a Gaussian character for the uncertainties from existing oscillation parameter measurements. An external χ^2_{osc} constrained by data from existing experiments is more rigorous, but is not used in this primitive study.

If we remove δ^{corr} from the χ^2 penalty term, then we are not relying on the absolute flux prediction or correlated detector efficiency, and only doing a relative rate analysis between ADs. This is the default analysis mode. Table 16 provides a summary of the parameters $\boldsymbol{\theta}$ in this physical model. By default, all parameters except for θ_{13} and δ^{corr} are constrained by penalty terms. There are a total of 2 *free parameters* and 21 *nuisance parameters* in this model.

Fig 74 shows the ratio of measured $\bar{\nu}_e$ events over expected events at each detector, assuming no oscillation. The x-axis shows the baseline of each detector weighted by the flux from each core. The 3 far site detectors are artificially separated by ± 50 meter to make them distinguishable on the figure. The grey band indicates the correlated uncertainty on total rate prediction, which is made a free parameter in the model. The error bars are statistical only. Large deficit is obvious at the far detectors relative to the near detectors.

Assuming an effective three neutrino oscillation formula

$$P(\bar{\nu}_e \rightarrow \bar{\nu}_e) = 1 - \sin^2 2\theta_{13} \sin^2 \Delta_{ee} - \cos^4 \theta_{13} \sin^2 2\theta_{12} \sin^2 \Delta_{21} \quad (5.8)$$

where $\Delta_{ij} \equiv |\Delta_{ij}| = 1.27 |\Delta m_{ij}^2| \frac{L[m]}{E[MeV]}$. The best fit value for θ_{13} is $\sin^2 2\theta_{13} = 0.086 \pm 0.011$. The best fit value for the flux normalization is $\delta^{corr} = 0.0128 \pm 0.006$, which means that the measurement is larger than the ILL prediction by 1.3%.

Table 16. Summary of Model Parameters in Rate-only Analysis

Parameter	Description	Count
$\sin^2(2\theta_{13})$	Short-baseline neutrino oscillation amplitude parameter	1
δ^{corr}	Total correlated variation in the expected $\bar{\nu}_e$ event rate	1
Δm_{32}^2	Short-baseline neutrino oscillation frequency parameter	1
$\sin^2(2\theta_{12})$	Long-baseline neutrino oscillation amplitude parameter	1
Δm_{12}^2	Long-baseline neutrino oscillation frequency parameter	1
δ_j^{AD}	Uncorrelated rate variation between each detector j	6
δ_k^r	Uncorrelated flux variation between each reactor k	6
δ_j^b	Uncorrelated rate variation in backgrounds in detector j	6

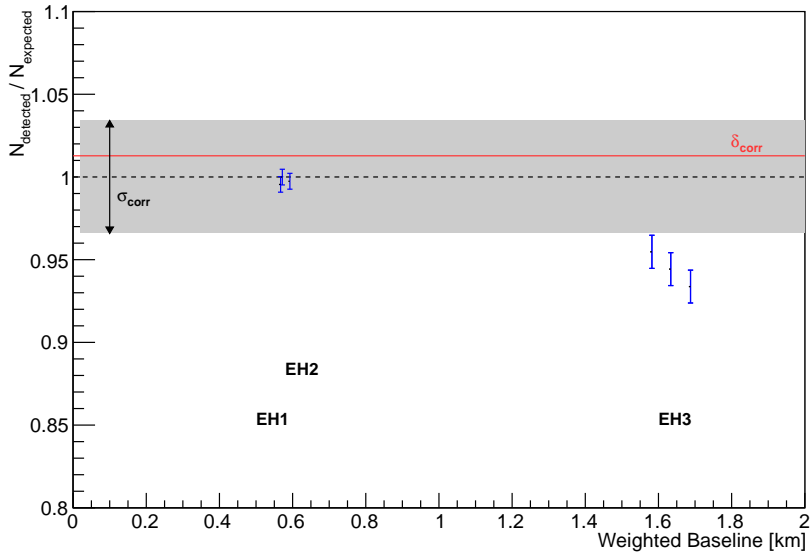


Figure 74. The ratio of measured $\bar{\nu}_e$ events over expected events at each detector, assuming no oscillation. The x-axis shows the baseline of each detector weighted by the flux from each core. The 3 far site detectors are artificially separated by ± 50 meter to make them distinguishable on the figure. The grey band indicates the correlated uncertainty on total rate prediction, which is made a free parameter in the model. The error bars are statistical only. Large deficit is obvious at the far detectors relative to the near detectors.

Fig. 75 shows the 1-D scan of the χ^2 distribution of $\sin^2 2\theta_{13}$, by marginalize all other parameters. The $\chi^2_{\min}/\text{ndf} = 2.48/4$, corresponding to p-value of 0.65. From the line corresponding to $\Delta\chi^2 = 1$ we find:

$$\sin^2 2\theta_{13} = 0.086^{+0.011}_{-0.011} \quad (5.9)$$

The significance of $\sin^2 2\theta_{13} > 0$ is 7.8σ , or at $(1 - 10^{-15})\%$ C.L.

Fig. 76 shows our projected precision of $\sin^2 2\theta_{13}$ measurement in 3 years, where we turned on 8 AD running after Aug, 2012. We further assumed an improvement on the uncertainty of background (due to more statistics) and the 6 MeV delayed energy cut($0.26\% \rightarrow 0.12\%$). An ‘ultimate’ precision of ~ 0.004 is projected.

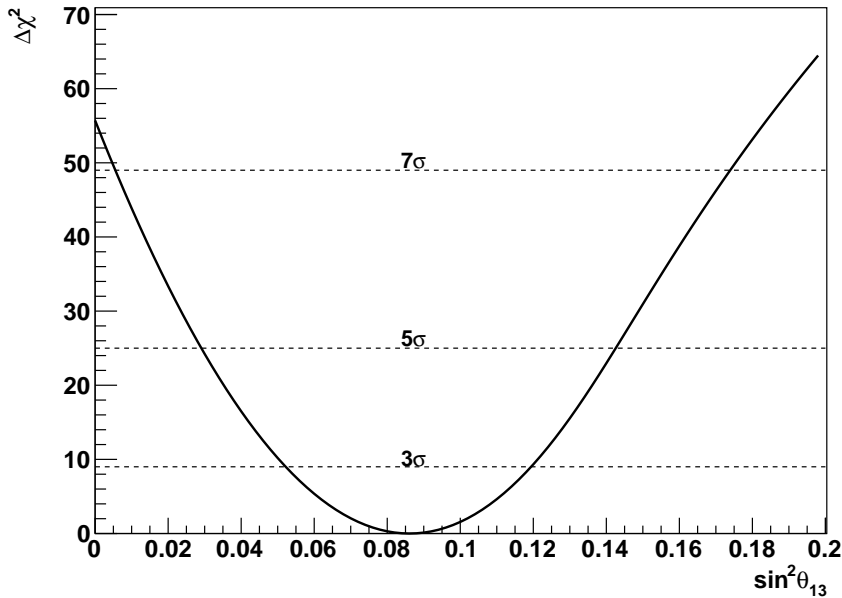


Figure 75. χ^2 distribution of $\sin^2 \theta_{13}$ in the rate-only analysis.

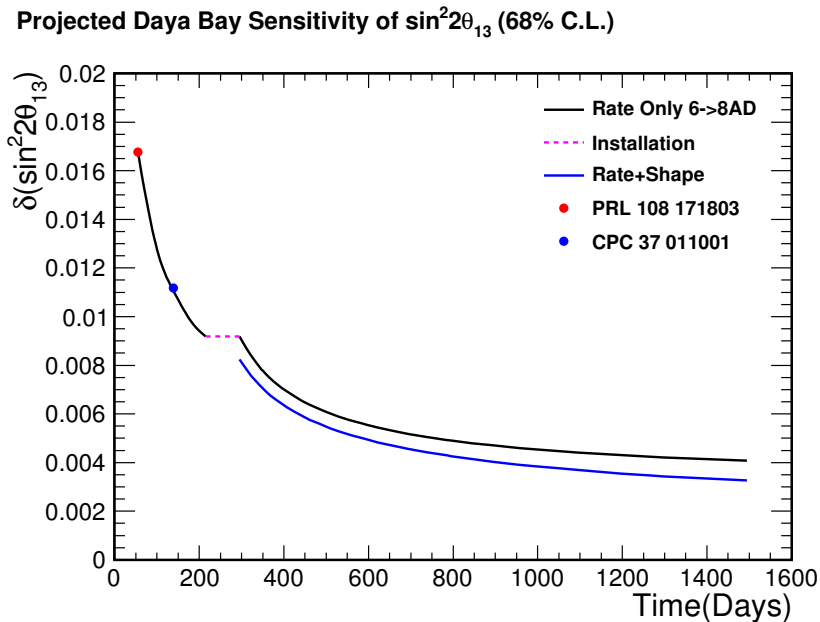


Figure 76. Evolution of the sensitivity to $\sin^2 \theta_{13}$ as Daya Bay accumulates more data over the next 3 years. The blue solid line shows the improvements if we do the shape analysis.

It has been shown in doc:7908 [63] that in the likelihood fitter, one can not cleanly separate the statistical uncertainty from systematic uncertainty, as well as the contribution of different systematic terms, because they are all correlated with each other. On the other hand, it is important to

know the approximate contribution of each systematic term, so that we can work hard on the more important issues. We use the following procedure to approximately breakdown the systematics:

- Do a regular fit. The total uncertainty is σ
- Fix all nuisance parameters at the best-fit value. The resulting uncertainty σ_{stat} is treated as from statistics only.
- Turn on one nuisance parameter at a time and redo the fit to obtain the uncertainty σ' . The uncertainty caused by this term is then approximated by $\sigma_i^2 = \sigma'^2 - \sigma_{stat}^2$. The uncertainty fraction of this term is calculated by $\sigma_i^2 / \sigma_{total}^2$
- Due to the correlation between systematic terms, the sum of σ_i^2 is not equal to σ_{total}^2 . The remainder is called σ_{others} ($\sigma_{total}^2 = \sigma_{others}^2 + \sum_i \sigma_i^2$) which indicates the size of the correlation effects.

The resulting breakdown of systematics in the rate-only analysis is shown in Fig. 77. Currently,

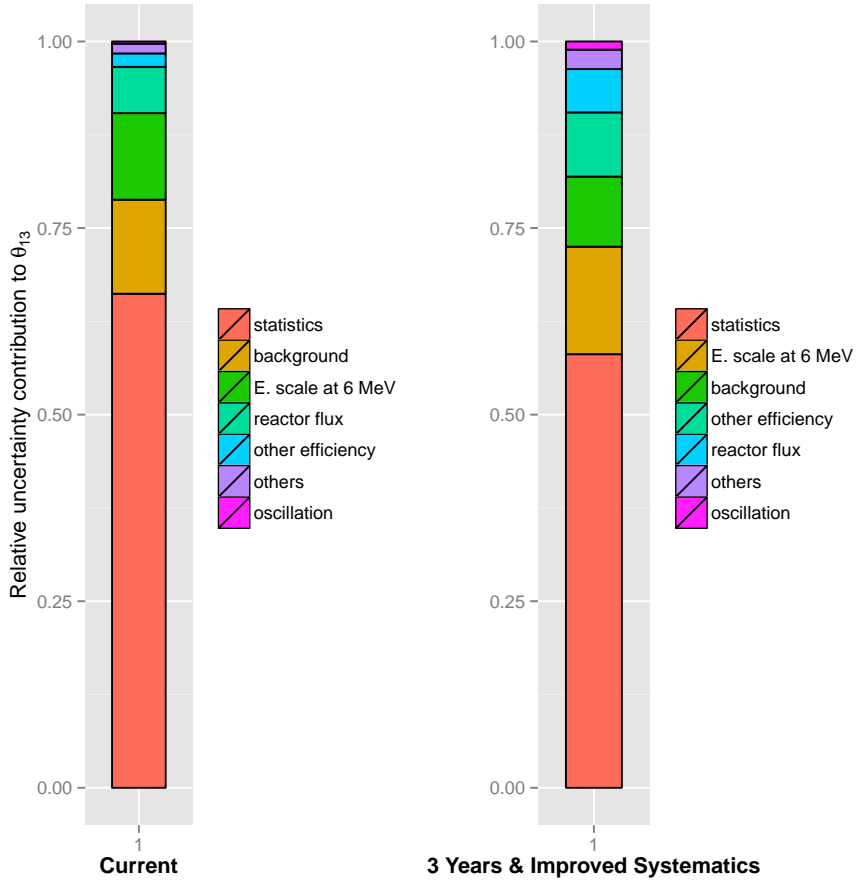


Figure 77. Breakdown of the $\sin^2 2\theta_{13}$ uncertainty contribution in the *rate-only* analysis.

the total uncertainty on $\sin^2 2\theta_{13}$ is dominated by the statistics, followed by background, delayed

energy cut and reactor flux. In 3 years, the statistical and the total systematic uncertainty will contribute about the same amount.

5.2 Rate + Shape analysis

5.2.1 Systematic considerations

Systematics relevant to the shape analysis have been discussed in their corresponding sections. Their summary is shown in Tab. 17. Due to the booming number of systematic uncertainties in antineutrino flux, we have merged all of them into a covariance matrix together with some detector effects as we have discussed in Sec 4.3.1.

5.2.2 χ^2 construction and event prediction

Shape chi-square construction Shape analysis chi-square is based on the rate analysis one shown in Eq. 5.6, with the addition of shape information reflected in the number of events in each energy bin. With the separation of rate and shape information in the event distribution in each energy bin of each AD, the systematic uncertainties that affect the event distributions need to be included,

$$\begin{aligned} \chi^2(\boldsymbol{\theta} | \delta^{corr}, \vec{\delta}^r, \delta^{AD}, \delta^b, \delta^{osc}) = & 2 \sum_j^{ADs} \left(N_j^{exp} - N_j^{obs} + N_j^{obs} \ln \frac{N_j^{obs}}{N_j^{exp}} \right) + 2 \sum_j^{ADs} \sum_{i=1}^{26} N_{ji}^{obs} \ln \frac{N_{ji}^{obs}}{N_{ji}^{exp}} (10) \\ & + \chi^2_{shape-penalty}, \end{aligned}$$

where $N_{ji}^{exp} \equiv N_{ji}^{exp}(\boldsymbol{\theta} | \delta^{corr}, \vec{\delta}^r, \delta^{AD}, \delta^b, \delta^{osc})$, the expect number of event in the i -th bin of AD j , is based on the expected event predictor we describe in the next paragraph, N_{ji}^{obs} is the i -th energy bin observed number of events of AD j and $N_j^{exp} = \sum_{i=1}^{26} N_{ji}^{exp}$ and $N_j^{obs} = \sum_{i=1}^{26} N_{ji}^{obs}$ are the total expected and observed numbers of events in AD j just like in the rate analysis. Now, $\boldsymbol{\theta}$ includes both θ_{13} and Δm_{32}^2 by default. $\vec{\delta}^r$, δ^{AD} , δ^b , and δ^{osc} represents the 4 groups of uncertainties' nuisance parameters: reactor related, AD related, background related and external oscillation parameter related systematic uncertainties listed in Tab. 17. **The nuisance parameters are not implemented to the first order any more like in the rate analysis due to more complicated bin to bin correlation in energy caused by different systematic effects. Instead, we consider the nuisance parameters in the event predictor based on their original definitions. This treatment increases the burdgen of the fitter but it considers energy bin to bin correlations thoroughly without any approximations, which we consider important in the shape analysis.** By default, we have no penalty for the overall normalization δ^{corr} , which shows our ignorance on the correlated detector efficiency and the chosen reactor flux model's normalization. $\chi^2_{shape-penalty}$ is the new penalty term considering all the systematic uncertainties in Tab. 17,

$$\chi^2_{shape-penalty} = \vec{\delta}^r^T (V^{-1}) \vec{\delta}^r + \sum_j^{ADs} \left(\frac{\delta_j^{AD}}{\sigma_j^{AD}} \right)^2 + \sum_j^{ADs} \left(\frac{\delta_j^b}{\sigma_j^b} \right)^2 + \sum_m^{osc} \left(\frac{\delta_m^{osc}}{\sigma_m^{osc}} \right)^2, \quad (5.11)$$

where the covariance matrix term $\vec{\delta}^r^T (V^{-1}) \vec{\delta}^r$ has included all the reactor related terms and $\vec{\delta}^r \equiv (\delta_1^r, \delta_2^r, \dots, \delta_k^r, \dots, \delta_{78}^r)^T$. Note that the additional shape term meets the following normalization

Table 17. Systematic summary of the shape analysis. Details are shown in corresponding sections.

Category	Name	Description	Correlation&Counts	Value(%)
Detector	σ_{eff}^{AD}	Relative detection efficiency uncertainties	Uncorrelated between ADs, 6	0.168
	σ_{scale}^{AD}	Relative energy scale uncertainties	Uncorrelated between ADs, 6	0.35
	$\sigma_{nonlinear}^{AD}$	Energy nonlinearity model parameter uncertainties	Correlated between all ADs, 4 parameters	100
Background	σ_{acc}^b	Accidental background uncertainties	Uncorrelated between ADs, 6	0.3-0.5
	$\sigma_{^8He/^9Li}^b$	${}^8He/{}^9Li$ background rate uncertainties	Uncorrelated rates between sites: 3	30
	$\sigma_{^8He/^9Li,ratio}^b$	${}^8He/{}^9Li$ ratio	correlated between ADs, 1	5
	$\sigma_{^8He/^9Li,kb}^b$	α and neutron energy quenching	correlated between ADs, 1	100
	$\sigma_{^8He/^9Li,nonlinear}^b$	β energy nonlinearity function	correlated between ADs, 4;	covariance matrix
	$\sigma_{FN,norm}^b$	Fast neutron background rate uncertainties	Uncorrelated between sites: 3	50
	$\sigma_{ACU,norm}^b$	ACU neutron source background uncertainties	Correlated between all ADs: 1	40
	$\sigma_{ACU,shp}^b$	ACU neutron source background uncertainties	Correlated between all ADs: 1 parameter from exponential shaped spectrum	15
Reactor	σ^r	$\alpha - n$ correlated background uncertainties	Uncorrelated between ADs: 6	50
		Reactor and fission isotope related uncertainties	Correlated between sites, 78	Matrix
Oscillation	σ^{osc}	Solar sector parameter uncertainties	Correlated between all ADs, 2	PDG

constraint for each of the individual AD j ,

$$\sum_{i=1}^{26} (N_{ji}^{exp} - N_{ji}^{obs}) = 0. \quad (5.12)$$

With the normalization constraint in Eq. 5.12, Equation 5.11 is equivalent to the following chi-

square using the log-likelihood approach of each energy bin,

$$\chi^2(\boldsymbol{\theta} | \delta^{corr}, \vec{\delta}^r, \delta^{AD}, \delta^b, \delta^{osc}) = 2 \sum_{i=1}^{26} \sum_{j}^{ADs} \left(N_{ji}^{exp} - N_{ji}^{obs} + N_{ji}^{obs} \ln \frac{N_{ji}^{obs}}{N_{ji}^{exp}} \right) + \chi^2_{shape-penalty}. \quad (5.13)$$

Expected event calculation With the addition of shape information, the prediction of the expected number of events needs to consider the energy response of the detector, not just the counting of total number of events in the pure rate analysis. We also need to note that this event predictor is called internally by the minimizer in each minimization step. Thus, the efficiency of this event predictor is essential for the performance of the minimizer. To increase its efficiency, we have proposed a “smearing matrix” approach as described in DocDB-8561 and DocDB-8612.

Our event predictor is coded in the following way:

1. Calculate the anti-neutrino spectra for each AD from each reactor and apply oscillation parameters with corresponding baselines
 - Spent nuclear fuel contribution applied here
 - Off-equilibrium contribution applied here
 - Apply the oscillation parameter nuisance parameters δ^{osc}
2. Convert the true energy spectra into deposit energy spectra
3. Apply the IAV effect, which is in the format of a 240×240 conversion matrix, to obtain the true visible energy spectra
 - Flux covariance matrix nuisance parameters δ^r are applied here
4. Evaluate the detector smearing matrices for both IBD and beta backgrounds
 - Smearing matrix for anti-neutrinos from reactors
 - Evaluate the ${}^8He/{}^9Li$ smearing matrix (${}^8He/{}^9Li$ spectrum is true energy based thus a smearing matrix that considers the electron nonlinearity effect and the detector resolution is needed)
 - Two components in the smearing matrix are the nonlinearity model and the resolution effect
 - Only nuisance parameters in δ^{AD} associated with the nonlinearity model and the energy resolution model are applied here
 - If none of the smearing matrix nuisance parameters are changed, no need to recalculate, which reduces the burden of the minimizer
5. Apply smearing matrices on the true visible energy spectra to obtain reconstructed energy spectra
6. Add in backgrounds which are evaluated in reconstructed energy¹³ to obtain the expected number of events in each energy bin

¹³the background spectra based on MC simulation like ACU and $\alpha - n$ can be expressed in any energy

P12E blinded 2D contour

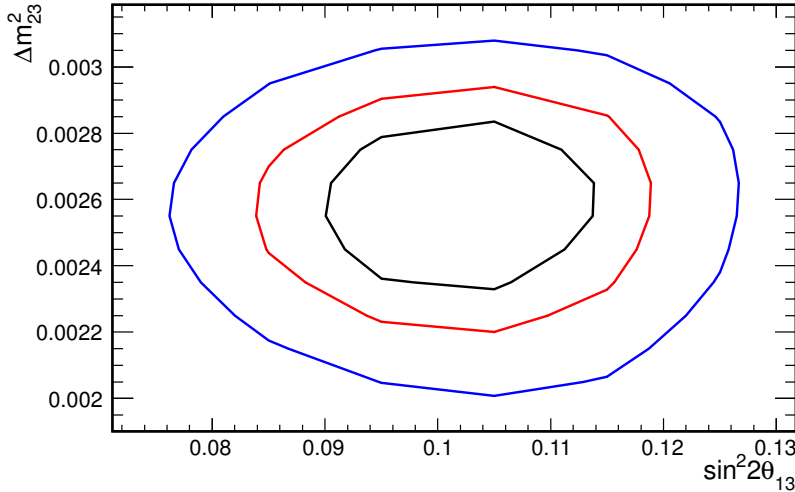


Figure 78. The chi-square contours with different reactor uncertainty treatments.

- Background nuisance parameters δ^b are applied here
- Detection efficiency nuisance parameters, a subset of δ^{AD} , are applied here

5.2.3 Results

Best-fit results (P12E) See DocDB-8923 for more description about the blinded dataset of P12E.

Fig. 78 shows the 1σ , 2σ and 3σ chi-square contours of $\sin^2 2\theta_{13}$ and Δm^2_{32} .

The best fit values are:

$$\sin^2 2\theta_{13} = 0.1017^{+0.008}_{-0.008} \quad (5.14)$$

$$\Delta m^2_{32} = (2.575^{+0.0169}_{-0.0169}) \times 10^{-3} (eV^2) \quad (5.15)$$

The best fit $\chi^2/NDF = 178.334/153$. The errors are quoted directly from the Minuit fitter. We also have shown that our result will not change if we switch to the other reactor flux model, such as ILL+Petr or ILL+Muller, more detailed information can be seen in DocDB-9133.

Systematic break down charts We checked the contributions of systematic uncertainties in the final fit assuming relative energy scale uncertainties, 0.12%. Results are shown in Fig. 79. We see the dominant systematic uncertainty after the total statistics for the Δm^2 precision is due to the relative energy scale.

Projection of the Δm^2_{ee} sensitivity With more statistics that Daya Bay will accumulate in forthcoming years, the Daya Bay sensitivity to Δm^2_{ee} could be competitive with results from the μ flavor sector by experiments like SuperK, T2K and MINOS. Figure. 80 shows the projection based on our current understanding of the relevant systematic uncertainties. For the difference between Δm^2_{ee} and $\Delta m^2_{\mu\mu}$, see more detailed discussions in DocDB-8727 and DocDB-8753 [64, 65]. After adding in

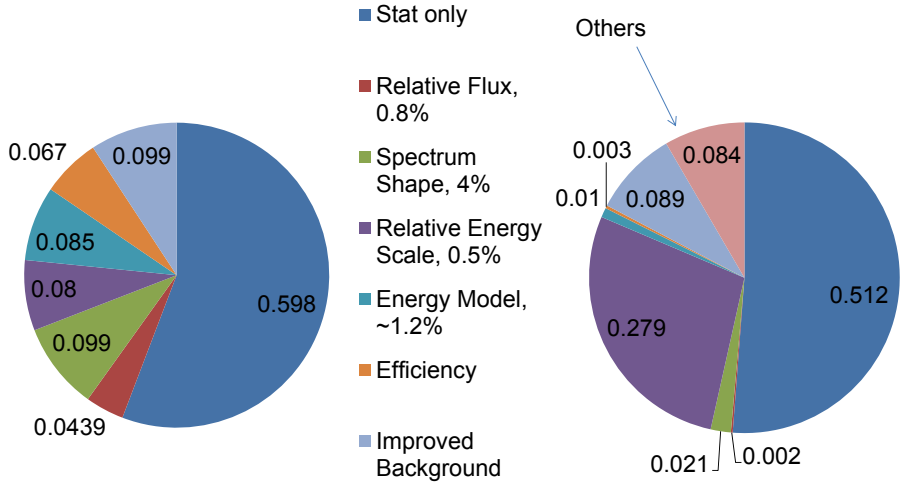


Figure 79. Breakdown the contributions of the systematic uncertainties of $\sin^2 2\theta_{13}$ and Δm^2_{32} ($\sigma_{scale}^{AD} = 0.12\%$)

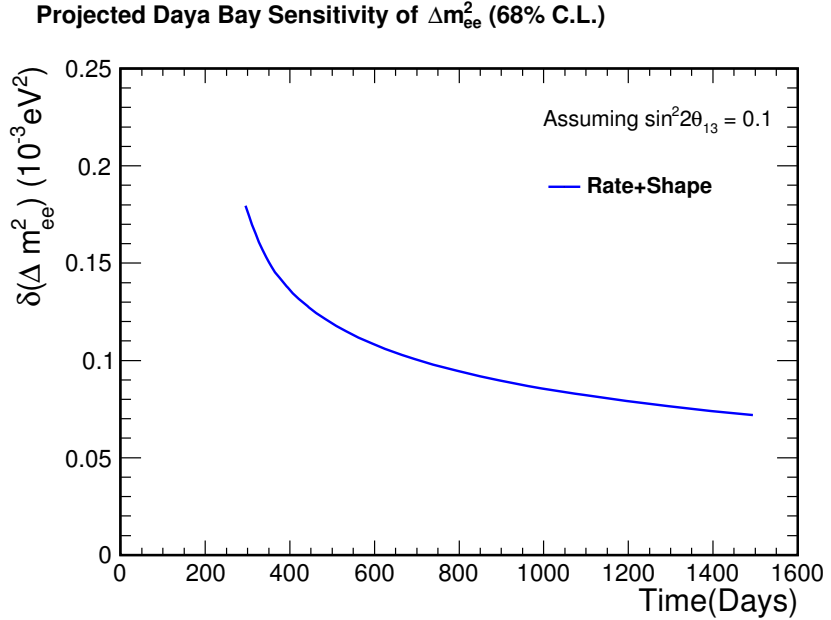


Figure 80. Evolution of Δm^2_{32} uncertainty of Daya Bay as statistics accumulates

the shape information, the Daya Bay sensitivity to $\sin^2 2\theta_{13}$ is also improved as shown by the blue curve in Fig. 76.

6. Summary

The BCW rate+shape analysis covers all corners of the essential components of the Daya Bay data analysis from reactor flux calculation and uncertainty treatments, the IBD&backgrounds identification and associated uncertainties, the detector energy scale non-linearity model and its validation, to the numerical technique considerations in the chi-square construction. In our analysis, for the reactor flux model, we checked the differences between the “old” and the “new” fluxes. Considering the challenge placed by the booming of systematic uncertainties in reactor flux, we propose a pull + covariance matrix approach to faithfully consider all the flux uncertainties while reducing the numerical challenge due to the large number of systematic uncertainties. Our correlation studies also show that the energy bin correlations at different experiment sites are noticeably different thus, to properly treat the correlations between all energy bins of all ADs, a 81×81 covariance matrix for anti-neutrino flux is necessary. In the detector energy non-linearity model, BCW adapted two different approaches to figure out AD’s energy responses: one is via the comparison between the near site observed and expected energy spectrum; the other is via the studies of the observed energies of various monoenergetic gammas’ presented either in ADs or in calibration sources. The latter is the bottom up approach one should take but the former should be satisfied since neutrinos have not oscillated much at near sites. Also in the latter study, by approaching the problem from fundamental levels, energy quenching in scintillator, we separate the electronic non-linearity from the physical processes in the liquid scintillator. Our studies prove the non-linearity in the electronic system needs to be considered and can be treated separately. Our two methods approaching the energy non-linearity have consistent results. Our non-linearity model is further validated by two independent data sets: the continuous spectra from ^{12}B and $^{212}Bi/^{214}Bi$. In the chi-square construction, we achieve a clean separation between rate and shape information by treating the systematic uncertainties’ rate and shape correlation properly. Our rate, shape and rate+shape analyses are consistent among one another. With our analysis framework, we find the dominant uncertainty in the rate+shape era, after the total statistics, is the relative energy scale uncertainty between ADs. This points out the direction we should put our effort in in our future work. Our projection of the Daya Bay sensitivity to Δm_{ee}^2 shows that, with improved understanding to the AD energy scale uncertainty, our sensitivity in the electron flavor is competitive with experiments from μ flavor sector like SuperK, T2K and MINOS. This shows a very attractive potential for future reactor neutrino oscillation experiments, currently the only electron flavor neutrino oscillation experiments available.

References

- [1] Y. Nakajima and *et al*, “Adsimple reconstruction (doc:7334).”.
- [2] J. J. Ling and X. Qian, *Position-dependence of Energy Resolution Study with Spallation and MCS Data (doc:8574)*.
- [3] J. B. Birks *Proc. Phys. Soc. A***64** (1951) 874.
- [4] J. J. Ling, X. Qian, and C. Zhang, “Gamma energy nonlinearity response (doc:8731).”.
- [5] Z. Yu, *Research on beta-alpha correlated decay in U/Th chain (doc:7220)*.

- [6] Y. Meng, ‘‘Boron12 study note and histogram (doc:8834).’’
- [7] P. K. V. Tsang, ‘‘B12/n12 - bcw & lbnl energy models (doc:8519).’’
- [8] F. H. Zhang *private communications*.
- [9] C. Zhang and X. Qian, ‘‘Validating energy model with low energy beta + gamma spectra (doc:8736).’’
- [10] B. Littlejohn *private communications*.
- [11] E. Worcester, ‘‘Effect of positron annihilation-in-flight on non-linearity (doc:8855)..’’
- [12] B. A. Faddegon, C. K. Ross, and D. W. O. Rogers *Med. Phys.* **17** 773.
- [13] L. Wen and *et al*, ‘‘Energy non-linearity correction (doc:8240).’’
- [14] S. Jetter, *Dealing with Energy Non-Linearity for a Shape Analysis (doc:8493)*.
- [15] S. Jetter, *Illustration of Charge Non-linearity From Toy MC (doc:8364)*.
- [16] X. Qian, ‘‘One thought about electronics non-linearity (doc:8907).’’
- [17] C. Zhang, ‘‘Ph.d. thesis on kamland.’’
- [18] H. W. C. Tseung, J. Kaspar, and N. Tolich *Nuclear Inst. and Methods in Physics Research A***654** (2011) 318.
- [19] B. von Krosigk *et. al.* arXiv:1301.6403 (2013).
- [20] X. C. Ruan and W. L. Zhong Measurement of Quenching Factor of Liquid Scintillator (doc:1999).
- [21] B. von Krosigk and L. Neumann SNO, *private communication*.
- [22] B. X. Yu and L. J. Wen, ‘‘Ls electron non-linearity measurement (doc:8521)..’’
- [23] X. Qian, C. Zhang, J. J. Ling, and W. Wang Summary of BCW Non-linearity Model (doc:8849).
- [24] C. Zhang, ‘‘Review of theory of beta decay (doc:8854).’’
- [25] C. Zhang and X. Qian, ‘‘Predicting beta decay spectrum (doc:8866).’’
- [26] Y. B. Liu and F. H. Zhang, ‘‘Updated expected energy spectrum of b12 (doc:8862).’’
- [27] X. Qian, ‘‘Update on electronics non-linearity (doc:8871)..’’
- [28] X. Qian, ‘‘Comparison of beta decay spectra (doc:8874)..’’
- [29] D. E. Alburger *Phys. Rev.* **131** (1963) 1624.
- [30] C. Zhang and X. Qian, ‘‘B12 spectra again (doc:8985)..’’
- [31] B. Littlejohn and *et al*, *Relative Energy Scale Uncertainties for P12C (doc:8570)*.
- [32] S. Jetter, ‘‘Review of ihep energy response model (doc:9121)..’’
- [33] Y. Nakajima, ‘‘Overview of lbnl non-linearity model (doc:9119)..’’
- [34] G. Li and *et al*, ‘‘Data quality check for p12c (doc:8487).’’
- [35] C. Zhang and *et al*, ‘‘Bcw θ_{13} oscillation analysis technote (doc:7464).’’
- [36] X. Qian, ‘‘Review of bcw background treatment for rate+shape analysis (doc:9140)..’’
- [37] L. Wen and *et al*, ‘‘Neutron-like singles study (doc:7043).’’
- [38] J. P. Ochoa, ‘‘Predicting the 9li background shape.’’

- [39] J. P. Ocoa, “Predicting the ${}^9\text{Li}/{}^8\text{He}$ background spectra (doc:8860)..”.
- [40] G. S. Li, “Non-linearity models correlation study (doc:9024)..”.
- [41] W. Gu and *et al.*, “Simulation on amc background (doc:6779)..”.
- [42] W. Q. Gu, G. S. Li, and J. L. Liu, “Amc background note (doc:8979)..”.
- [43] Z. Yu and *et al.*, “Estimation of (α, n) background (doc:7509)..”.
- [44] Z. Yu and *et al.*, “Alpha-n background spectrum update (doc:8716)..”.
- [45] X. Qian and W. Wang, “The uncertainty on total ibd events caused by the time averaging of reactor flux and target mass (doc:7208)..”.
- [46] C. Lewis, X. Qian, W. Wang, and C. Zhang, “How to do weekly thermal power average and fission fraction average? (doc:7993)..”.
- [47] F. Von Feilitzsch, A. Hahn, and K. Schreckenbach, *EXPERIMENTAL BETA SPECTRA FROM PU-239 AND U-235 THERMAL NEUTRON FISSION PRODUCTS AND THEIR CORRELATED ANTI-NEUTRINOS SPECTRA*, *Phys.Lett.* **B118** (1982) 162–166.
- [48] K. Schreckenbach, G. Colvin, W. Gelletly, and F. Von Feilitzsch, *DETERMINATION OF THE ANTI-NEUTRINO SPECTRUM FROM U-235 THERMAL NEUTRON FISSION PRODUCTS UP TO 9.5-MEV*, *Phys.Lett.* **B160** (1985) 325–330.
- [49] A. Hahn, K. Schreckenbach, G. Colvin, B. Krusche, W. Gelletly, *et. al.*, *ANTI-NEUTRINO SPECTRA FROM PU-241 AND PU-239 THERMAL NEUTRON FISSION PRODUCTS*, *Phys.Lett.* **B218** (1989) 365–368.
- [50] P. Vogel, G. Schenter, F. Mann, and R. Schenter, *REACTOR ANTI-NEUTRINO SPECTRA AND THEIR APPLICATION TO ANTI-NEUTRINO INDUCED REACTIONS. 2.*, *Phys.Rev.* **C24** (1981) 1543–1553.
- [51] T. Mueller, D. Lhuillier, M. Fallot, A. Letourneau, S. Cormon, *et. al.*, *Improved Predictions of Reactor Antineutrino Spectra*, *Phys.Rev.* **C83** (2011) 054615, [[arXiv:1101.2663](#)].
- [52] P. Huber, *On the determination of anti-neutrino spectra from nuclear reactors*, *Phys.Rev.* **C84** (2011) 024617, [[arXiv:1106.0687](#)].
- [53] G. Mention, M. Fechner, T. Lasserre, T. A. Mueller, D. Lhuillier, M. Cribier, and A. Letourneau, *Reactor antineutrino anomaly*, *Phys. Rev. D* **83** (Apr, 2011) 073006.
- [54] Z. Djurcic, J. Detwiler, A. Piepke, J. Foster, V.R., L. Miller, *et. al.*, *Uncertainties in the Anti-neutrino Production at Nuclear Reactors*, *J.Phys.* **G36** (2009) 045002, [[arXiv:0808.0747](#)].
- [55] B. Zhou, X.-C. Ruan, Y.-B. Nie, Z.-Y. Zhou, F.-P. An, *et. al.*, *A study of antineutrino spectra from spent nuclear fuel at Daya Bay*, *Chin.Phys.* **C36** (2012) 1–5.
- [56] F.-P. An, X.-C. Tian, L. Zhan, and J. Cao, *Systematic impact of spent nuclear fuel on θ_{13} sensitivity at reactor neutrino experiment*, *Chin. Phys.* **C33** (2009) 711–716.
- [57] V. Kopeikin, L. Mikaelyan, and V. Sinev, *Antineutrino background from spent fuel storage in sensitive searches for θ_{13} at reactors*, *Phys.Atom.Nucl.* **69** (2006) 185–188, [[hep-ph/0412044](#)].
- [58] C. Jones, A. Bernstein, J. Conrad, Z. Djurcic, M. Fallot, *et. al.*, *Reactor Simulation for Antineutrino Experiments using DRAGON and MURE*, *Phys.Rev.* **D86** (2012) 012001, [[arXiv:1109.5379](#)].
- [59] X. Ma, “Validating dragon for daya bay reactor neutrino experiment (docdb-7413)..”.

- [60] X. Ma, “Reactor flux calculation (docdb-8163).”.
- [61] V. Kopeikin, L. Mikaelyan, and V. Sinev, *Reactor as a source of antineutrinos: Thermal fission energy*, *Phys.Atom.Nucl.* **67** (2004) 1892–1899, [hep-ph/0410100].
- [62] X. Ma and W. Zhong, “Update of thermal fission energy calculation (docdb-8669).”.
- [63] X. Qian and *et al*, *Separation of Statistical and Systematic uncertainty for $\sin^2 2\theta_{13}$* (*doc:7548*).
- [64] Y. Nakajima, “How to define δm_{ee}^2 (*doc:8727*).”.
- [65] W. Wang, “What do SK/MINOS/K2K measure (*doc:8753*).”.